

## REPORT DOCUMENTATION PAGE

Form Approved  
OMB No. 0704-0188

The public reporting burden for this collection of information is estimated to average 1 hour per response, including the time for reviewing instructions, searching existing data sources, gathering and maintaining the data needed, and completing and reviewing the collection of information. Send comments regarding this burden estimate or any other aspect of this collection of information, including suggestions for reducing the burden, to Department of Defense, Washington Headquarters Services, Directorate for Information Operations and Reports (0704-0188), 1215 Jefferson Davis Highway, Suite 1204, Arlington, VA 22202-4302. Respondents should be aware that notwithstanding any other provision of law, no person shall be subject to any penalty for failing to comply with a collection of information if it does not display a currently valid OMB control number.  
PLEASE DO NOT RETURN YOUR FORM TO THE ABOVE ADDRESS.

1. REPORT DATE (DD-MM-YYYY)			2. REPORT TYPE FINAL REPORT		3. DATES COVERED (From - To) 15 Mar 07 – 30 Nov 08
4. TITLE AND SUBTITLE RESEARCH INSTITUTE FOR AUTONOMOUS PRECISION GUIDED SYSTEMS			5a. CONTRACT NUMBER  5b. GRANT NUMBER FA9550-07-1-0236  5c. PROGRAM ELEMENT NUMBER 61102F		
6. AUTHOR(S) DR JOHN R. ROGACKI			5d. PROJECT NUMBER 2304  5e. TASK NUMBER CX  5f. WORK UNIT NUMBER		
7. PERFORMING ORGANIZATION NAME(S) AND ADDRESS(ES) UNIVERSITY OF FLORIDA RESEARCH AND ENGINEERING EDUCATION FACILITY SHALIMAR, FL			8. PERFORMING ORGANIZATION REPORT NUMBER		
9. SPONSORING/MONITORING AGENCY NAME(S) AND ADDRESS(ES) AFOSR.RSL 875 NORTH RANDOLPH ST, ROOM 3112 ARLINGTON, VA 22203-1678			10. SPONSOR/MONITOR'S ACRONYM(S)  11. SPONSOR/MONITOR'S REPORT NUMBER(S) AFRL-QSR-VA TR-2012-0378		
12. DISTRIBUTION/AVAILABILITY STATEMENT DISTRIBUTION A					
13. SUPPLEMENTARY NOTES					
14. ABSTRACT There was significant progress made in delivering a hardship-in-the-loop rapid prototyping capability at the UF-REEF. Embedded systems are designed to control complex plants such as land vehicles, satellites, space crafts, unmanned aerial vehicles (UAVs), aircrafts, weapon systems, marine vehicles, and jet engines. They generally require a high level of complexity within the embedded system to manage the complexity of the plant under control. Hardware-in-the-loop (HIL) simulation is a technique that is used increasingly in the development and test of complex real-time embedded systems.					
15. SUBJECT TERMS					
16. SECURITY CLASSIFICATION OF: a. REPORT		17. LIMITATION OF ABSTRACT	18. NUMBER OF PAGES	19a. NAME OF RESPONSIBLE PERSON  19b. TELEPHONE NUMBER (Include area code)	
b. ABSTRACT	c. THIS PAGE				

*Final report*

RESEARCH INSTITUTE FOR PRECISION GUIDED SYSTEMS

FA 9550-07-1-0236

Submitted by:

Dr. J. Rogacki and Dr. L. Ukeiley  
Research and Engineering Education Facility (REEF)  
University of Florida, Shalimar, FL

Dr. W. Dixon, and Dr. R. Lind  
Department of Mechanical and Aerospace Engineering  
University of Florida, Gainesville FL

Submitted to:

Dr. Fariba Fahroo  
Program Manager, Computational Mathematics  
875 Randolph Street, Ste 325, Rm 3112  
Arlington VA 22203

Nov 30, 2008

20120918128

## TABLE OF CONTENTS

<u>ABSTRACT</u> .....	3
<u>REVIEW TECHNICAL ACCOMPLISHMENTS BY TASK</u> .....	4
Task 1: Full Vehicle Virtual Prototyping: Control Synthesis and Aero-structural Characteristics of Micro Air Delivered Munitions (MADM) and Micro Air Vehicles (MAV).....	4
Task 2: Integrated Visual-Servo Control and Path Planning for Unmanned Air Vehicles .....	12
Task 3: Aerodynamic and Structural Characterization of Flexible and Morphing MAVs.....	15
Task 4: Control of Biologically-Inspired Morphing for Variable-Geometry MAVs .....	44
Task 5: Computational Aerodynamics of Flexible and Flapping Wing for MAVs.....	65
<u>PERSONNEL SUPPORTED DURING DURATION OF THE GRANT</u> .....	68
<u>PUBLICATIONS</u> .....	69
<u>HONORS &amp; AWARDS RECEIVED</u> .....	72
<u>AFRL POINTS OF CONTACT</u> .....	72
<u>TRANSITIONS</u> .....	73
<u>NEW DISCOVERIES</u> .....	73

## **ABSTRACT**

The Research Institute for Precision Guided Systems (RIAPGS) was awarded a 21 Month grant on 1 March 07 to conduct groundbreaking research on Agile Autonomous Munitions (AAM). The research directly supports the mission needs of the Air Force Research Laboratory Munitions Directorate (AFRL/RW) in developing technology for semi-autonomous micro air vehicles. Research supported under the FY03 RIAPGS grant poised the UF-REEF and its partners to assume the role of a world leader in AAM research. The recently completed effort documented in this final report has built upon the results obtained from AFOSR funding of the 2003, three-year RIAPGS grant and its two extensions (8 month extension concluding 30 Nov 2006 and 3 month extension ending 28 Feb 07), and leverages the capabilities established, in large part, by AFOSR DURIP grants awarded to the University of Florida Research and Engineering Education Facility (UF-REEF). A team of experts from the UF-REEF, UF-Gainesville, University of Alabama, and University of Michigan conducted the research. The effort was conducted under the auspices of the Agile Autonomous Munitions Center of Excellence (AAM COE), a partnership between the University of Florida (REEF and Gainesville campuses) and AFRL/RW. The AAM COE, which supports the UF-REEF Research Institute for Autonomous Precision-Guided Systems, serves as the focal point for the research, development, design, analysis, testing and transition of technologies necessary to attain agile, smart munitions operating autonomously or cooperatively in complex, uncertain, adversarial environments (see Figure 1). The recently completed (30 Nov 08) 21 month grant had objectives and milestones in years 2007 and 2008 under the following 5 tasks:

- Task 1: Full Vehicle Virtual Prototyping: Control Synthesis and Aero-structural Characteristics of Micro Air Delivered Munitions (MADM) and Micro Air Vehicles (MAV)
- Task 2: Integrated Visual-Servo Control and Path Planning for Unmanned Air Vehicles
- Task 3: Aerodynamic and Structural Characterization of Flexible and Morphing MAVs
- Task 4: Control of Biologically-Inspired Morphing for Variable-Geometry MAVs
- Task 5: Computational Aerodynamics of Flexible and Flapping Wing for MAVs

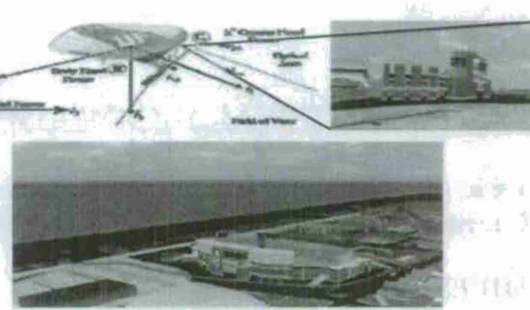
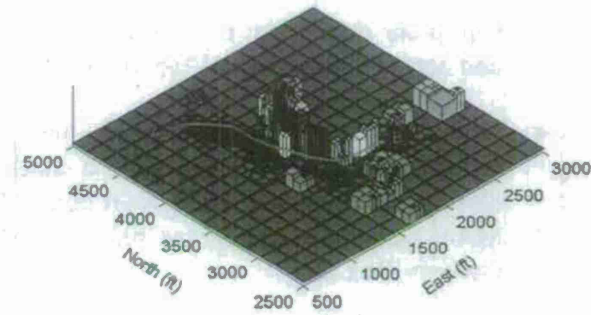


Figure 1, Semi-autonomous Path Planning and Obstacle Avoidance Research Results



Task 5 was a 9 month tasks that ended on 30 Nov 07. The remaining three tasks continued until 30 Nov 08.

### **REVIEW TECHNICAL ACCOMPLISHMENTS BY TASK**

#### **Task 1: Full Vehicle Virtual Prototyping: Control Synthesis and Aero-structural Characteristics of Micro Air Delivered Munitions (MADM) and Micro Air Vehicles (MAV)**

##### **MILESTONES/STATUS:**

###### **Months 1-9**

- Complete derivation of methods for characterizing MAV nonlinear dynamic response and aerodynamic models for MAV configurations. (Completed)
- Static mounted MAV models will be aerodynamically characterized and their aerodynamic coefficients will be modeled and provided to the Visualization Lab so closed loop testing of the visual controller technology can be simulated with innovative MAV aerodynamic designs such as morphing. (Completed at UF-REEF Labs and UF-Gainesville Labs)
- Inner loop stabilization of MAV using visual-servo control techniques derived in Task 2 via implementation and testing in the hardware in the loop environment. (Completed)
- Derivation, development and implementation of virtual prototyping methods associated with path planning in the image-space as derived in Task 2. (Completed)

###### **Months 10-21**

- Hardware-in-the-loop testing and evaluation of 3-dimensional visual-servo control derived in Task 2. (Completed)
- Hardware -in-the -loop testing and evaluation of geometry and obstacle estimation-based MAV vehicle control. (Partially Completed- Simulations run on desk top computer and not in real time on a field deployable laptop)

### **GENERAL**

Under the leadership of Dr. Rogacki and Dr. Albertani there was significant progress made in delivering a hardware-in-the-loop rapid prototyping capability at the UF-REEF. Embedded systems are designed to control complex plants such as land vehicles, satellites, spacecrafts, unmanned aerial vehicles (UAVs), aircrafts, weapon systems, marine vehicles, and jet engines. They generally require a high level of complexity within the embedded system to manage the

complexity of the plant under control. Hardware-in-the-Loop (HIL) simulation is a technique that is used increasingly in the development and test of complex real-time embedded systems.

The purpose of HIL simulation is to provide an effective platform for developing and testing real-time embedded systems. HIL simulation provides an effective platform by adding the complexity of the plant under control to the test platform. The complexity of the plant under control is included in test and development by adding a mathematical representation of all related dynamic systems. These mathematical representations are referred to as the "plant simulation." The UF-REEF has established a HIL simulation capability for MAV's that will lead to a rapid prototyping capability.

The Task 1 research plan included testing the visual based control system running on the cluster PCs in the REEF Visualization Lab by flying a relatively stable off the shelf slow flier (similar to MAV flight regime) in the small REEF wind tunnel and later in the large wind tunnel. The general layout of the test bed is illustrated in Fig. 2.

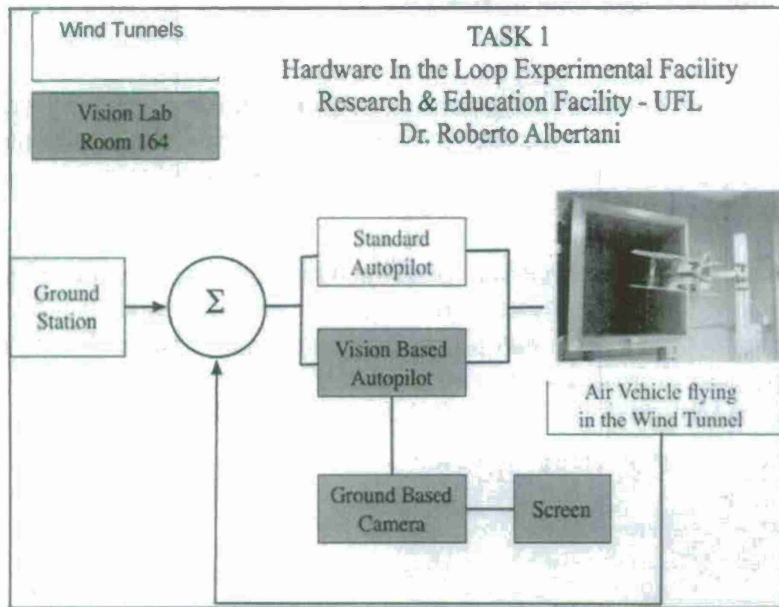


**Figure 2.** Lay-out of the HIL experimental test bed showing the vision-based autopilot (grey) and the aircraft systems (yellow) in the wind tunnel.

#### AIRPLANE DESCRIPTION

The airplane chosen for the experiment was a biplane that had a wingspan of 68.4cm and a total wing area including both wings of 2642 cm<sup>2</sup>. Both wings are flat plates and made from thin foam sheets. As can be seen in Figure 3, the structure was stiffened using carbon fiber stiffening rods. The airplane is considered a profile airplane because it does not have a traditional fuselage.

Instead it has two flat foam pieces shaped like a fuselage that are glued together perpendicular to one another. Figure 3 is a picture of the airplane.

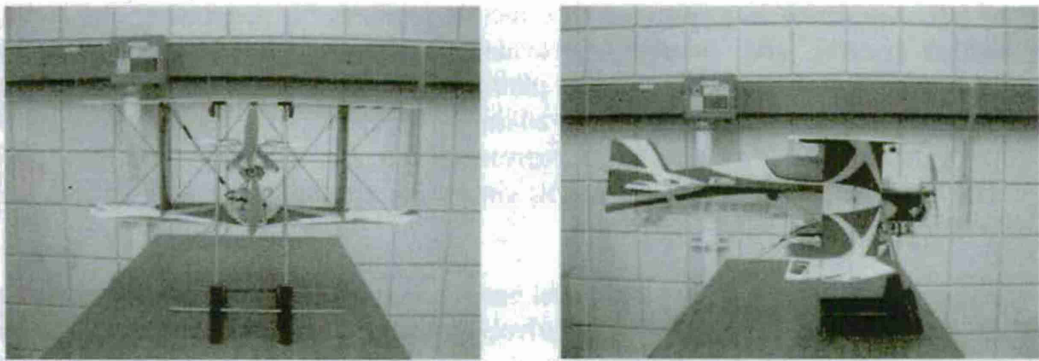


**Figure 3.** Front and side view of airplane.

The airplane was setup with conventional controls that consist of a rudder, elevator, and ailerons. A pitot tube was installed on the right wing to measure free stream velocity. Because of the fuselage design, a carrying tray was added to the front of the airplane and was used to mount the autopilot. A ball joint was used to join the airplane to the mount.

Communication with the airplane's onboard autopilot was conducted through the virtual cockpit software that came with the autopilot. The computer on which the software was installed used a communication box to send signals to the airplane autopilot. The transmitter was used to trim the airplane before maneuvers and also to input manual commands if needed. The 3-DOF rig design illustrated in Figure 4 was used to install the Tensor 4-D aircraft in the wind Tunnel.

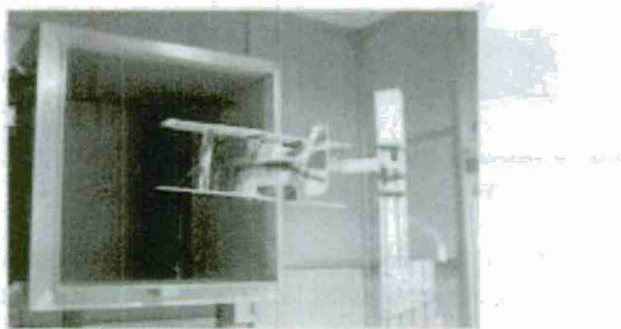


**Figure 4.** View of the airplane on the three D.O.F. joint in the wind tunnel.

Flight data were recorded on the ground station PC using the onboard telemetry system. The ground station, located outside the wind tunnel, was connected with the cluster PCs in the REEF Visualization Lab. The ground station received data from the aircraft on-board system and sent the information, through an internet connection, to the Visualization Lab.

## **EXPERIMENTAL SET-UP**

The hardware used in this project includes the remote controlled airplane, a ground station computer, a camera, and a server cluster used to create a virtual environment. The scope of this project was to create a communications system for these four components of hardware by writing software, which interpreted data between them since the camera and the UAV as well as the ground station, and server cluster were in separate labs. The end product software developed enabled communication between these systems. The quality of the data transfer can be verified by plotting control inputs and aircraft flight data.

## **COMMUNICATION SOFTWARE**

Two software packages were designed and used for two computers in the HILS system. The first program (Program 1) is loaded onto the ground station computer in the Wind Tunnel Laboratory (WT Lab) and the second (Program 2), which consists of a simple test socket of a server, is loaded onto the Visualization Laboratory (Vis Lab) computer. These programs implement the following procedures:

### **Program 1**

- ◆ Connect to Autopilot via a socket connection as client using Virtual Cockpit
- ◆ Connect to Vis Lab via socket connection as client
- ◆ Retrieve data at 6Hz from the autopilot
- ◆ Package data in vector form containing the heading, pitch, and roll. These are 2-byte integers with units of radians\*1000)
- ◆ Send data at 6Hz to Vis Lab
- ◆ Receive data at 6Hz from Vis Lab
- ◆ Output the sent and received data as well as elevator and aileron angles to the output file on hard drive for graphical analysis
- ◆ Display transfers in the GUI on the desktop (specifically sent data, received data, elevator angle, and aileron angle)

### **Program 2**

- ◆ Connect to WT Lab via a socket connection as a server
- ◆ Receive data from WT Lab
- ◆ Display data to command prompt

## RECORDED FLIGHT DATA

Pitch, roll, and yaw angle data, pitch, yaw, and roll rates, elevator, aileron, and rudder servo displacement values, and airspeeds were recorded during several maneuvers performed with the Tensor 4D aircraft with the Kestrel autopilot installed. The data was collected at a 20 Hz sample rate. A total of 200 samples were collected over a 10 second period for each maneuver.

Commanded pitch and roll doublets were performed. The data was collected at two wind tunnel airspeeds with the model mounted at the ball joint and the CG at the midpoint of the recommended aircraft CG range. Airspeeds were recorded during all of the tests.

The pitch and roll angle measurements and servo displacement values measured by the autopilot are provided as sample data. Plots of the pitch angle and elevator servo position and roll angle and aileron servo position are provided in Figs. 5a and 5b respectively for the low velocity case. The data trends recorded by the autopilot are consistent with the expected results. The high effectiveness of the dual sets of ailerons on the model can be observed from the small amplitudes of the roll aileron servo positions. The autopilot is trying to damp out the roll rate by counteracting the commanded input thus the servo position data appears slightly noisy. The pitch and roll angle plots are smooth which is consistent with the observed motion. The activity with the vision based autopilot is mainly dedicated to a reliable fast real-time connection between the aircraft ground station located in the wind tunnel lab and the vision camera-large screen set located in the Visualization lab. The ground station sends a set of variables as the three aircraft angle and rates and flight velocity to the vision autopilot that will detect the motion through a camera looking at a virtual scene on a large screen. The horizon on the screen moves with a motion defined from the real aircraft in the wind tunnel. The vision autopilot reaction is sent back to the ground station through the two laboratories communication systems and to the aircraft in the wind tunnel through the wireless link between the vehicle and the ground station.

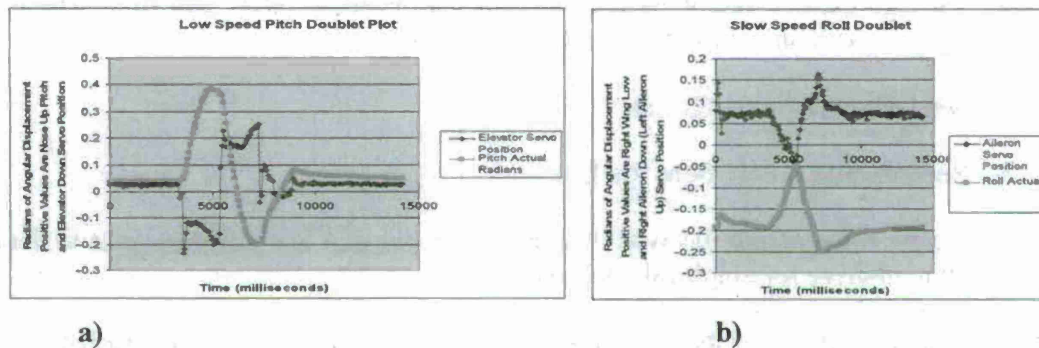


**Figure 5.** a) Low speed pitch doublet and b) low speed roll doublet. The values in radians are the servo position (blue) and the aircraft attitude (purple).

The originally desired frequency of data transfer was 25 Hz. This would have allowed the virtual environment to refresh quickly enough to produce very high quality imagery and to match better the expected dynamics of the aircraft. However, a frequency constraint exists due to the lack of the GPS system on the Procerus autopilot. The GPS system is required for the necessary packet to be requested (Packet 18) in DevDemo allowing the 25 Hz sampling rate transmission. Due to the lack of GPS, the transmission sampling rate was limited to 6 Hz.

An algorithm was implemented to create these lines as well as measure the pitch and roll from the deviations and lines to display the deviations from level trim conditions and return them to the Wind Tunnel Laboratory to use for analysis [1]. The camera sends the image it ‘sees’ to the workstation for the vision-based autopilot to analyze as shown in Figure 6. When a yellow line is visible, there is a pitch deviation from zero. When the red line is not horizontal, there is a roll deviation

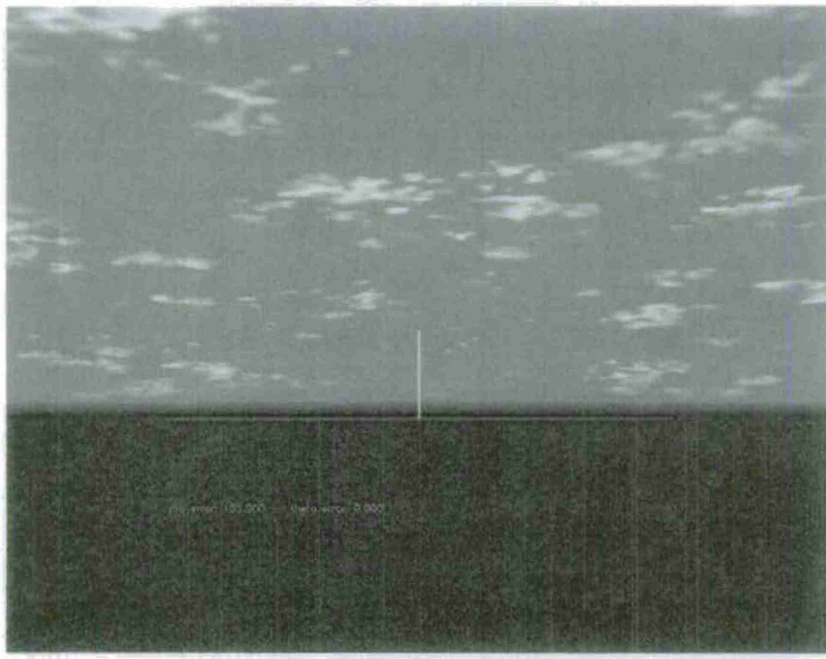


**Fig. 6.** Virtual Environment Display with Telemetry Measurements.

## SAMPLE OF RESULTS

Several tests were performed in wind-off and wind-on conditions. The output files from the final tests are processed by a MATLAB code which creates a matrix from the space delimited output data file as a time vector calculated dynamically based on the 6Hz sample rate. The system reads the aircraft attitudes from the on-board IMU and estimates the same quantities from the visual data on the screen in the visualization lab. The percent error for the data is calculated from the matrix of data from the file using the equation:

$$\text{Percent\_Error} = \frac{\text{Nominal} - \text{Experimental}}{\text{Nominal}} \cdot 100$$

Where the “Nominal” value is the telemetry data collected from the aircraft on-board system and the “Experimental” value is the data calculated by the vision-based system. A sample of results is illustrated in Fig. 7 and Fig. 8 during a wind-on test with a pilot induced roll-pitch doublet

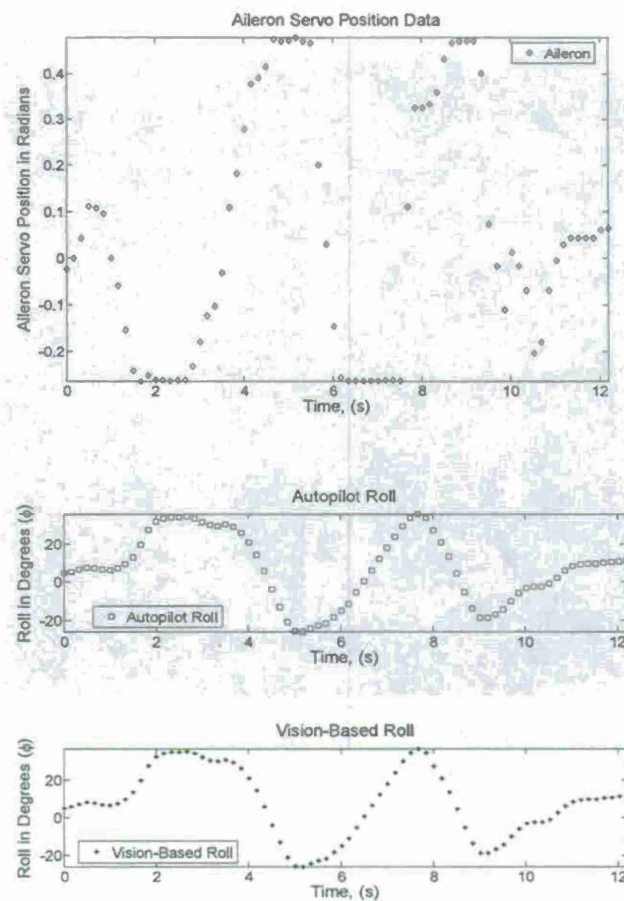


**Fig. 7.** Wind Tunnel Roll and Pitch Test – Aileron Angles and Roll Data.

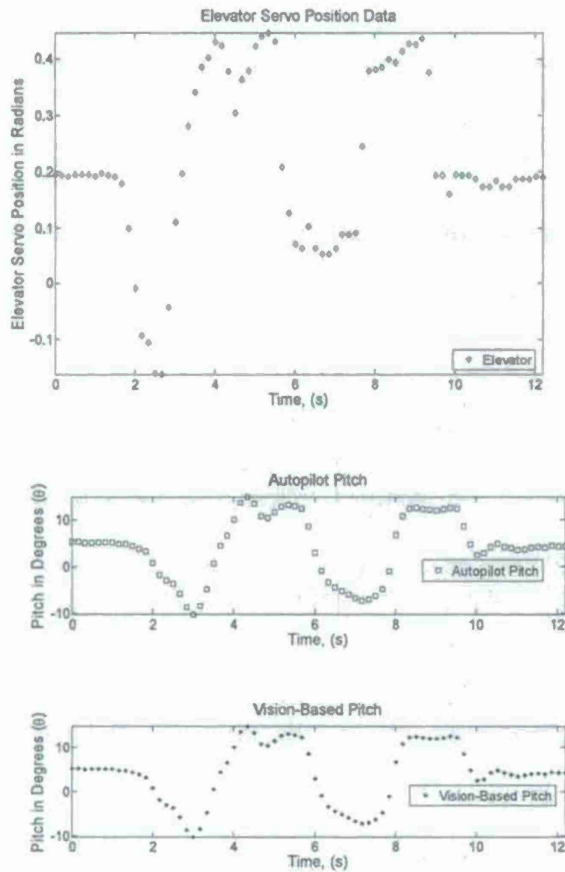


**Fig. 8.** Wind Tunnel Roll and Pitch Test – Elevator Angles and Pitch Data.

## CONCLUSIONS

The communications system created during this phase of Task 1 has resulted in a software package capable of testing a camera in loop with an UAV operating in a wind tunnel. A series of tests results show that the data processed in this communications system is reliable and capable of real time operations. The maximum error between the autopilot telemetry data and data calculated and sent from the visualization system was less than 0.3% with an average value of less than 0.1%. The software development package used was Microsoft Visual C++ and resulted in a GUI interface, which allows the user to interact dynamically with the system.

A follow-up phase could increase the degrees of freedom of the aircraft to eventually reach a free flight situation in the wind tunnel including an active propeller and adding flow perturbations. Finally a close the loop control would be implemented involving a feedback signal from the visual control camera and the UAV on-board control system.

## REFERENCES

- [1] Gans, N, A Kurdila, W E. Dixon, and R Lind. A, "Hardware in the Loop Simulation Platform," University of Florida, Virginia Polytechnic Institute, 2008.

## Task 2: Integrated Visual-Servo Control and Path Planning for Unmanned Air Vehicles

### MILESTONES/STATUS

#### First 9 Months:

- Develop and demonstrate optimization methods that refine the path planning methods in the presence of obstacles in the image-space flight path. These algorithms will be developed based on known and unknown topologies. (Completed)
- Complete development and demonstrate vision based state estimation strategies including structure from motion (SFM) and simultaneous localization and mapping (SLAM) methods. (Completed)
- Develop and demonstrate visual-servo controllers that use multi-vehicle (air to air, air to ground) images for collaborative mission objectives. (Completed)

#### Months 10-21

- Develop and demonstrate visual-servo controllers for MAV that are robust to camera uncertainty. (Completed)
- Develop and demonstrate quaternion-based visual-servo controllers to eliminate rotation singularities. (Completed)
- Develop and demonstrate visual-servo control techniques that account for the partial controllability of an MAV that may be maneuvering at nonlinear operating points away from trim. (Completed)
- Develop and demonstrate optimal path planners for obstacle avoidance that ensures targets remain in the field of view. (Completed)

Under the leadership of Dr. Dixon University of Florida and Dr. Gans (UF-REEF) there was significant research accomplishments achieved: Further development and verification of the "Daisy-Chaining" method for large-scale vision-based estimation and visual servoing of unmanned air and ground vehicles (UAV and UGV, respectively). Development of a novel visual servoing method to move a camera in order to keep multiple objects in the field of view without computationally expensive image processing or tracking algorithms was achieved.

## DAISY-CHAINING VISUAL SERVOING FOR LONG RANGE MICRO AIR VEHICLE (MAV) CONTROL

A principle concern in visual servoing, particularly when involving aerial vehicles, is the limited field of view of the camera. When an airborne camera (such as mounted on micro air vehicle, high altitude plane, etc.) is used as the sole sensor to generate control input for a MAV, there are several concerns. First, there must be a method to relate the position of the MAV to fixed reference objects (e.g. buildings) in order to generate estimates of the current MAV pose and velocity and relate it to desired MAV pose and velocity. Furthermore, as the camera and MAV move, fixed objects will leave the field of view, and new reference objects must be integrated into the estimation algorithm. This is a difficult problem. As seen in Figure 9, for one camera, one MAV and one reference object, eight pose estimates must be solved and chained. When a second reference object is involved (i.e. a new reference object has entered the field of view) this expands to sixteen pose estimates. Furthermore, not all targets may be in the camera field of view at the same time, requiring a robust estimation method for this data.

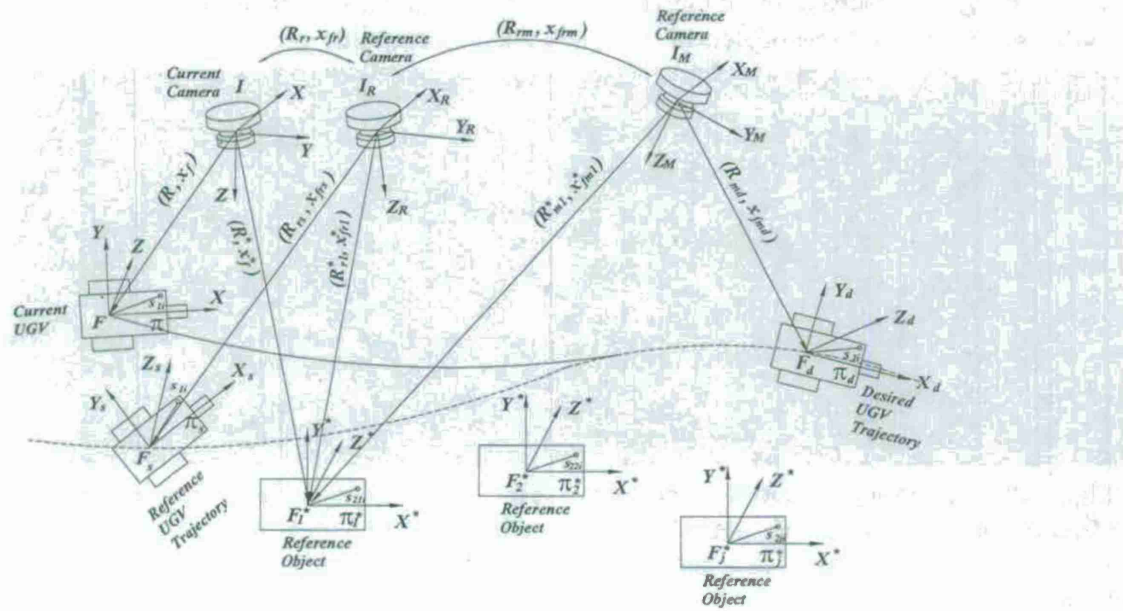


Figure 9-Illustration of Daisy Chaining for MAV control

The Daisy Chaining method can be used to solve this problem. By exploiting multi-view geometry and structure-from-motion methods of computer vision with nonlinear control theory, the UF has designed a vision-based control system that can regulate a MAV to a desired trajectory using vision data from an airborne camera that accepts new reference objects as they enter the field of view, and drops previous ones as they leave.

## UNDERDETERMINED VISUAL SERVOING FOR MULTIPLE TARGET TRACKING

The vast majority of visual servo controllers are designed to regulate the robot, vehicle, etc. to a specific fixed pose or along a specific fixed trajectory. However, there are many tasks do not require or do not have a fixed goal pose or trajectory for the robot. Thus a novel visual servo

control method was explored that does not regulate the robot to a goal, rather the control regulates some task functions and allows the robot to move to whatever pose is necessary to regulate the task functions. This freedom of motion leads to this controller being an underdetermined system. A further benefit of the underdetermined approach is the expensive feature extraction, tracking, and matching algorithms are not needed to identify and associate targets in each image.

The challenging task is tracking one or more targets (Fig. 10 and Fig. 11). Example scenarios are keeping a moving vehicle or a dispersing crowd in the field of view of an airborne camera. This can be done by regulating the distribution (e.g. mean and variance) of targets in an image. If mean target position is regulated to the image center and variance of target positions is regulated to less than  $\frac{1}{2}$  the image width, at least 75 % of all targets must be in the field of view. Depending on the distribution, this can increase up to 95%. Additional task functions can be added, such as keeping a desired distance or orientation to the targets. One task the UF has explored is maximizing *perceptibility*, which is a measure of how well the airborne camera can quickly change the distribution of targets in the image. Simulations have shown that this method is adept at keeping multiple objects in view, and that perceptibility help tracking.



Fig. 10- Keeping multiple moving objects in the field of view. For simplicity, pink targets are added to targets for recognition.

Fig. 11- Keeping a single moving object in the field of view. Target recognition is used to find the vehicle without using artificial pink targets.

#### VISUAL-SERVO CONTROL FOR UNMANNED AIR VEHICLES

- 1) Extension of a novel visual servoing method to move a camera in order to track multiple teams of targets, while maintaining network communications between multiple moving MAV's.
- 2) Extension of the Hardware In the Loop Simulation (HILS) to include a physical MAV in a wind tunnel, connected to a the visualization system.

#### Ensuring Network Connectivity of MAV's Performing Video Reconnaissance:

Motivated by mission scenarios and sensor restrictions, operations may require the collaboration of assets over an ad-hoc network. We have explored the problem of balancing trade-offs between asset/sensor cone positioning to satisfy target tracking requirements and network requirements

such as maintaining network connectivity. There is a direct need for methods that manage trade-offs between asset/sensor cone positioning to satisfy mission requirements and network requirements to ensure effective collaboration between the assets. Yet, literature that focuses on such issues appears sparse.

The problem considered involves multiple MAV's equipped with cameras. Each MAV is dedicated to monitoring/tracking a team of moving targets, but the communication network between the MAV's must be maintained for mission success. To address the trade-offs between asset positioning and network connectivity, a prioritized task-function based guidance law was developed for a simple scenario containing three assets. One developed task-function maintains a communication network by ensuring the distance between the MAV's does not exceed a critical threshold. Additional task-functions enable assets to keep targets of interest in the image cone by regulating image features derived from the camera view. Simulations demonstrated that such tradeoffs could be successfully achieved.

### **EXTENSION OF THE HARDWARE IN THE LOOP SIMULATION PLATFORM FOR VISION-BASED CONTROL OF MICRO AIR VEHICLES**

A desired outcome for Task 2 is to develop a sophisticated simulation test bed for the vision-based control of MAV's. This test bed will ultimately provide multiple stages of increasing hardware interaction. The first stage is a virtual reality data base capable of displaying large environments and controls processing. The second stage is a system of modular displays, digital cameras and computers for image and control processing. The third stage, recently implemented, incorporates a wind tunnel, MAV and force measurement system. The MAV is mounted on a sting balance in a low turbulence wind tunnel. Actuation of airfoils in the airflow of a wind tunnel will change the attitude of the MAV. The attitude change is relayed to the VE software, which alters the viewpoint accordingly. In turn, the vision-based control routines send velocity commands to the MAV autopilot (see details under Task 1).

#### **Task 3: Aerodynamic and Structural Characterization of Flexible and Morphing MAV**

##### **MILESTONES/STATUS**

###### **First 9 Months/Status:**

- Complete acquisition of and document experimental data sets (force/moment, flow field, deformation/shape) on fixed and passively flexible wings. (Completed)
- Collaborate with computational group (Task 5) to assess and evaluate results of fixed and passively flexible wing. (Completed)
- Define (with input from Task 4) and build actively morphing wing for investigating time-dependent phenomena. (Completed)
- Initiate acquisition of experimental data sets (force/moment, flow field, deformation) on actively morphed wings.

###### **Months 10-21**

- Complete acquisition of and document experimental data sets (force/moment, flow field, deformation) on actively morphed wings. (Completed at Gainesville)
- Collaborate with computational group (Task 5) to assess and evaluate results of morphed wings. (Collaborated with controls group on stability and control)
- Define (with input from Task 4) and build actively flapping wing for investigating time-dependent phenomena. (Completed)
- Initiate acquisition of experimental data sets (force/moment, flow field, deformation) on actively flapping wings. (Completed)

## GENERAL

Under the leadership of Dr. Ukeiley and Dr. Albertani from the UF-REEF and Dr. Hubner from the University of Alabama (UA) there has been significant progress in the experimental effort to characterize the aerodynamic and structural characteristics of MAV style airfoils and wings. This progress has been on several fronts by the team at the UF-REEF and the University of Alabama which include;

- The study of the effects of passive flexibility on separation characteristics of 2-D airfoils
- The characterization of steady and unsteady deformation of flexible wings including modeling of aeroelastic effects
- Steady and unsteady aerodynamic characterization of MAV configurations
- Detailed flow measurements of the of low aspect ratio wings

## CHARACTERIZATION OF LOW REYNOLDS NUMBER WIND TUNNEL

The Aerodynamic Characterization Facility was designed and installed at the UF-REEF under efforts partially supported by the RIAGPS. This has included a large effort to quantify the facility characteristics which is being reported in Albertani et al (2009). Photographs of the facility are shown in 12 and 13 below. The facility is housed in a large laboratory of approximately 50 x 60 feet to provide a large enough environment to isolate the effects of the surroundings from the flow through the wind tunnel. As can be seen in the figures this is an open return wind tunnel with an open jet test section. The air for the facility is moved by a 50 horse power 60 inch diameter fan. The fan is controlled by variable frequency drive electronics which allows for the varying of the wind tunnel velocity. The flow path starts by entering the conditioning section which has a cross sectional area of 10 foot by 10 foot through a bell mouth inlet. The flow conditioning section consists of a radiused inlet, metal honeycomb, and then several screen packs to break up any coherent large scale motions. This section is then followed by a 4.5 foot long straight settling region which allows for all any small scale organized motions generated by the flow conditioning section to relax. This settling chamber is then followed by a square contraction section with an area ratio of 8 to 1 whose contour was designed using the tools discussed in Mathew (2006). The exit of the contraction is a 42" square which is the start of the open jet test section and is displayed in 13 (b). This open jet test section is 10 feet long

and has a rigid enclosure that can be seen in 12. The enclosure consists of two parts, an outer shell which consist of foam core wall office structure and an inner structure made of up of 80/20 structural material. The overall dimensions of the enclosure are 11 ft high, 12 ft wide and 15 ft long. At the downstream end of the test section is a bell mouth fiberglass piece leading into 45.6 inch square opening to the diffuser section. The diffuser section transitions from a square cross-section to a 60 inch diameter circle, over a 99 inch axial distance, which is connected to the fan through a flexible coupling. The axial fan was manufactured by Howden Buffalo and is spun by a 50 HP Reliance Electric motor. The motor is controlled by a Toshiba VF-AS1 high performance inverter. This inverter (Variable Frequency Drive, VFD) controls the frequency of the electricity to the motor, which in turn controls the rotation rate of the fan and hence the flow velocity in the test section. At the end of the motor housing is inline flow silencer.

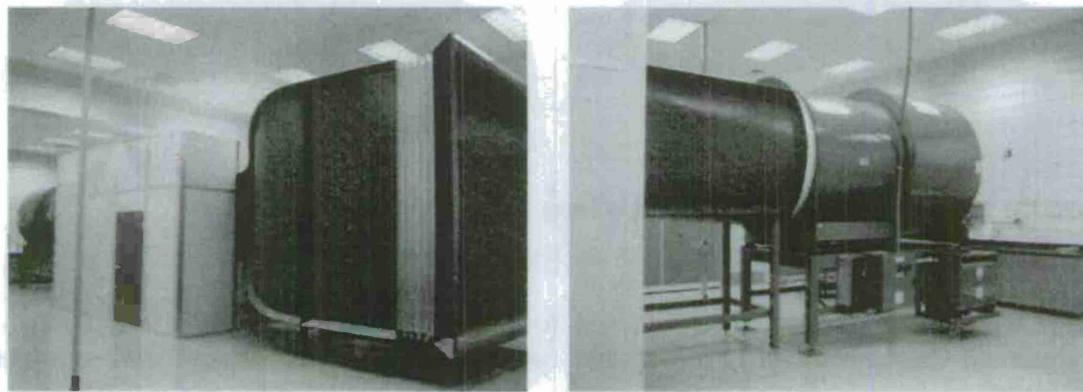


**Figure 12: Photographs of Aerodynamic Characterization Facility.**

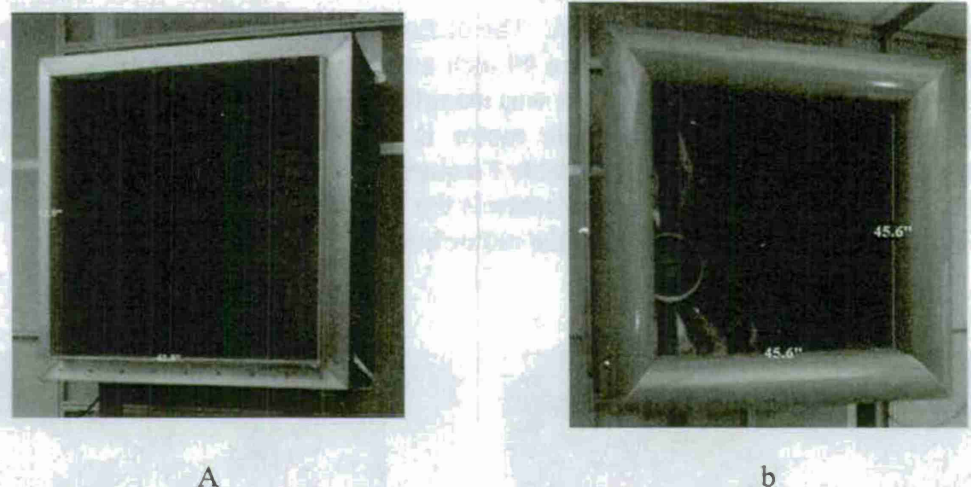


**Figure 13: Photographs of Test Section's Inlet (a) and Exit (b).**

#### **Assessment of Flow Quality**

A large experimental effort was conducted to determine the properties of the flow in the Aerodynamic Characterization Facility that has included both qualitative and quantitative assessments.

Since the input to set the rotation rate of the fan is the frequency on the Variable Frequency Drive (VFD), experiments to calibrate this value versus the air velocity at the inlet to the test section were performed. Several experiments have been performed with a Pitot-Static pressure probe situated in the center of the exit plane of the end of the contraction. All of these experiments involved setting the VFD to the prescribed frequency then letting the pressures in tubes equilibrate before taking the pressure data and averaging. This resulted in sampling the pressure at 2 Hz for 60 seconds to obtain the average velocity at the center of the entrance to the test section. It should be noted that all of data presented here was for VFD frequencies of up to 50 Hz however, one can easily extrapolate to the maximum value of 60 Hz.

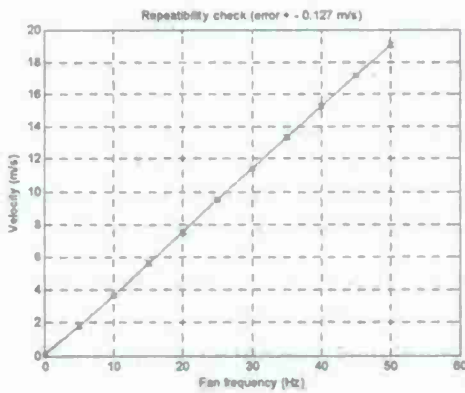


**Figure 14: Velocity vs. Frequency Calibration Curve**

Figure 14 displays a calibration curve to map from the VFD to flow velocity at the entrance to the test section. These experiments were performed several times with different transducers. However the most accurate one available at the UF- REEF is a Heise model ST-2H with both 0.5 and 2 inches of water transducers which have an accuracy of 0.005% of the full scale pressure reading. This results in a velocity accuracy of 0.2 m/s which are plotted as the error bars on this figure. Several experiments revealed that the measurements were repeatable and did not exhibit any hysteresis when the velocity was being approached from either ascending or descending values.

The Reynolds number per unit length and one based on the test section diameter are displayed in Table 1. This demonstrates that for an airfoil with a 6 inch chord length, the Reynolds numbers would range from approximately 16,000 through 175,000. As will be shown below the facility has been demonstrated to maintain a steady velocity in the 1.5 m/s free stream range validating the overall goal of a low Reynolds number facility.

VFD Setting (Hz)	Velocity (m/s)	Re (based in test section diameter)	Re per unit length ( $m^{-1}$ )
5	1.6	114,000	107,406
10	3.4	238,000	220,952
15	5.2	364,000	336,760
20	6.8	490,000	454,592
25	8.8	616,000	574,112
30	10.4	742,000	692,406
35	12.5	868,000	810,838

40	14.2	994,000	929,567
45	15.8	1,120,000	1,047,037
50	17.6	1,246,000	1,162,792

**Table 1: Flow Velocity and Reynolds Number versus VFD Setting**

Flow uniformity studies were conducted with a total pressure rake which had 32 ports each separated by 1 inch. The rake itself along with the way it was mounted is displayed in Figure 15. For the flow uniformity studies the rake was traversed (manually) through 21 vertical locations and 2 spanwise locations to develop a uniform grid spaced by 2 inches in both directions. The pressure readings were acquired with the Pressure Systems Inc. scanning pressure system with 16 ports with a 1 psi full scale range. This system quotes an accuracy of 0.05% of full scale which resulted in an accuracy 1.438 m/s. For all of the measurements the data was averaged over 120 samples which were acquired at a rate of 2 Hz. All of the velocities presented in this section are normalized by the velocity at the center location. It should be noted that the rake measurements will only be reported for one velocity setting (approximately 15 m/s) although flow uniformity measurements were additionally acquired at a free stream velocity of 2 m/s and are documented in Albertani et al (2009). Since the accuracy and range of the Pressure Systems scanning pressure system does not allow for reliable interpretation of the data at lower velocities a Scanni-Valve pressure switch was used with the Heisse transducer discussed above.

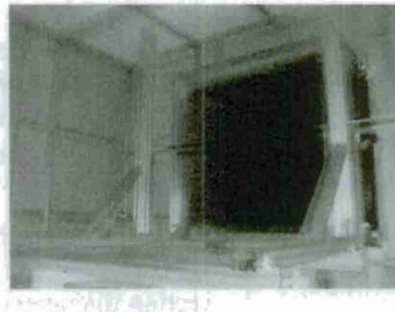


**Figure 15: Total Pressure Rake for Flow Uniformity Studies.**

Contour maps of the velocity field calculated from the total pressure measurements at 4 axial locations are displayed in Figure 16 for a 40 Hz setting on the VFD which corresponds to centerline velocity of approximately 15 m/s. From these plots the flow possesses a uniform core that covers at least 60% of the cross sectional area even at 62.5 % of the axial extent of the test section. Qualitatively there are some small asymmetries but in general the flow appears to evolve in a symmetric fashion.

In order to gain a better quantitative assessment of the flow quality, plots of the normalized velocities for both centerline horizontal and vertical slices at the 4 axial positions are presented in Figure 17. From these plots it is clear that there are no significant trends from top to bottom or left to right in the wind tunnel. Also apparent in these plots is how small the variations are on the order of less than 0.5%.

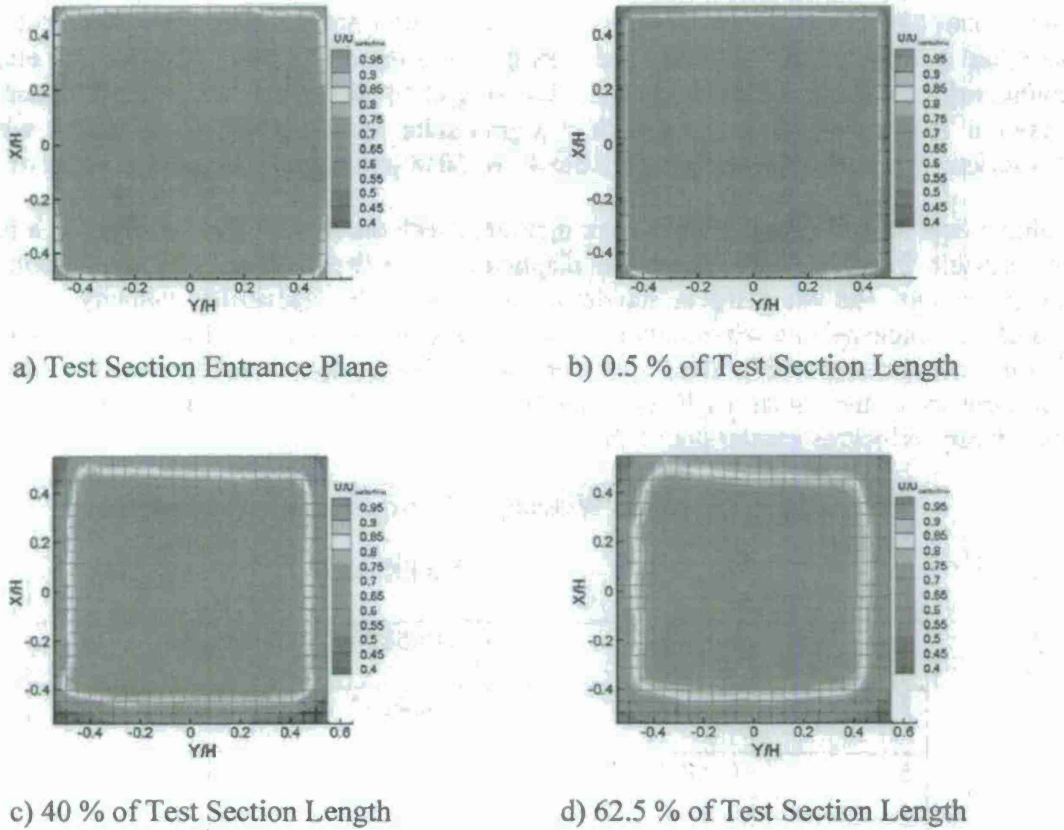


Figure 16: Flow Uniformity at 40 Hz VFD Setting (~15 m/s).

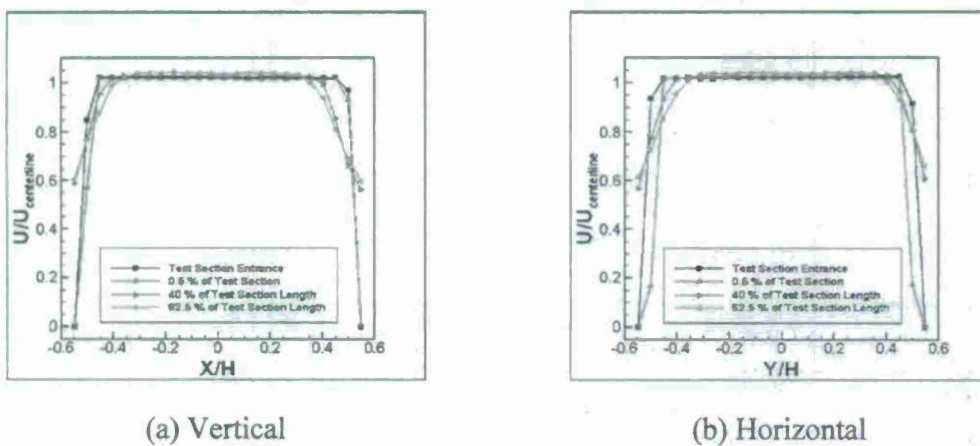


Figure 17: Centerline Vertical and Horizontal Velocity Profiles at 40 Hz on the VFD (~15 m/s).

Although the pressure measurements were quite encouraging in terms of flow uniformity, a device with a higher frequency response was needed in order to evaluate the unsteadiness. For

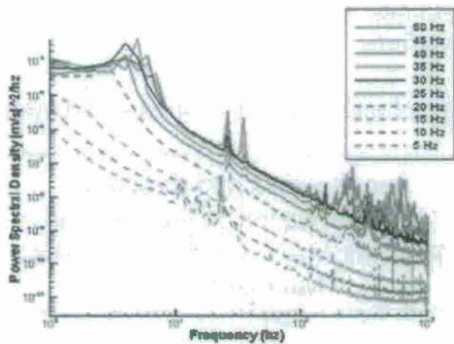
the rest of this section the measurements that will be discussed obtained using a single component constant temperature hot-wire anemometer system. The sensing element of the hot wire had a diameter of 5 microns and a length of nominally 1 mm. The sensing element was connected to a Dantec 55M10 bridge. The output of the bridge was then digitized with the National Instruments 4472 card with a sigma-delta analog-to-digital converter with 24 bit resolution. For these experiments, 256 blocks of 2048 points were acquired at a rate of 2048 Hz.

Table 2 lists several quantities that were measured with the hot-wire anemometer as a function of the variable frequency drive system as displayed in the first column. The second column is the mean velocity and the third is standard deviation of the fluctuating velocity. To calculate turbulence intensity in a wind tunnel it is common practice to high pass filter the fluctuations so that those associated with scales larger than the facility are not taken into account. After filtering out these scales the values are listed in the last column of Table 2 and are all less than 0.25% for free stream velocities greater than 1 m/s.

VFD Setting	U, Mean Velocity (m/s)	$\langle u \rangle$ (m/s) No Filtering	Turbulence Intensity $\langle u'_{\text{filtered}} \rangle / U$
1	0.1362	0.005679	4.0 %
3	0.2895	0.004152	1.4 %
5	0.9492	0.001213	0.12 %
7	2.3154	0.002255	0.09 %
10	3.3505	0.004158	0.06 %
15	5.1066	0.008787	0.13 %
20	6.8934	0.012275	0.11 %
25	8.7058	0.017555	0.16 %
30	10.4996	0.027106	0.21 %
35	12.2955	0.027439	0.17 %
40	14.0959	0.024822	0.14 %
45	15.8772	0.024201	0.07 %
50	17.6325	0.024383	0.06 %

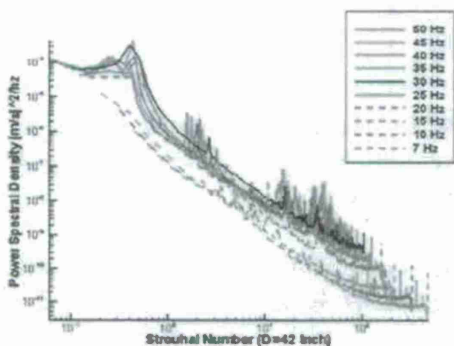
Table 2: Mean Velocity and Turbulence Intensities

Figure 18 displays the velocity power spectral density plotted at several settings of the VFD. The general trend of the data from 5 Hz on the VFD and up is expected, i.e., increasing energy levels in the fluctuating velocity as the speed of the tunnel is increased. From this plot one can also view the extension of the smaller scale (higher frequency) phenomena as one would expect with increasing Reynolds number.



**Figure 18: Power Spectral Density vs. Frequency Plots.**

Although the overall behavior for the higher frequency cases shows the correct trends there are several peaks that might be considered troublesome. The first are those that occur in the range of flow frequencies between 3 and 8 Hz which begin to become apparent between drive frequencies of 15 and 20 Hz and persist to the maximum velocities tested. To investigate these peaks the power spectral densities are plotted versus Strouhal number ( $fD/U$ ) in Figure 19 with the length scale, D, being the 42 in exit length of the contraction. Clearly, the peaks in this frequency range appear to have collapsed around a Strouhal number of 0.45. This number is in the range of what is generally expected for the Jet Column Mode.



**Figure 19: Power Spectra Plotted vs. Strouhal Number.**

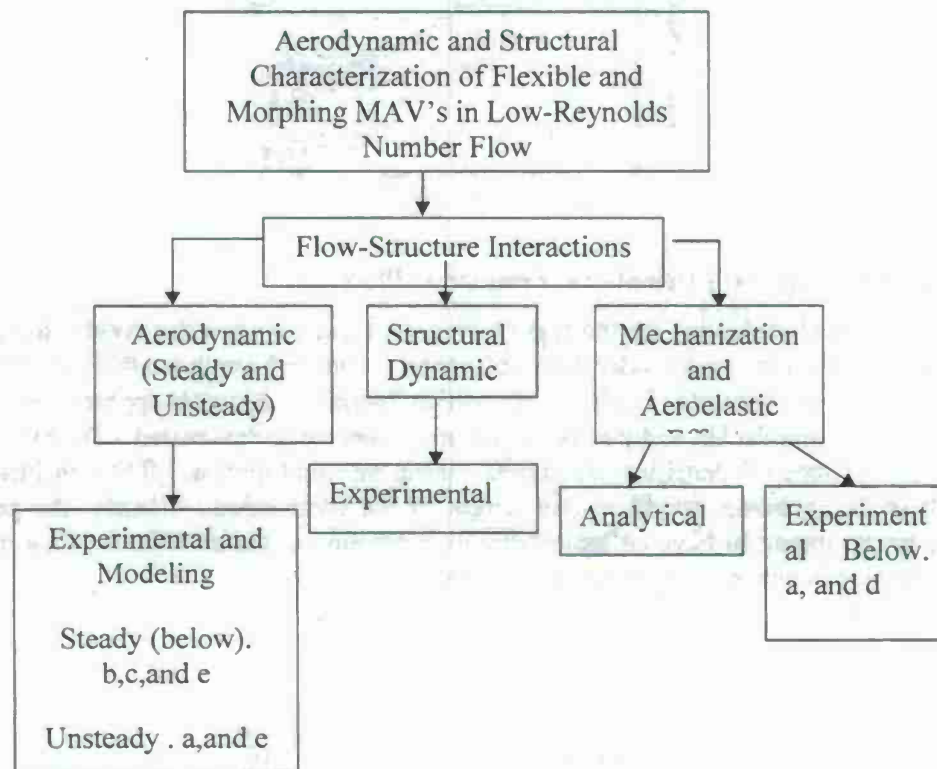
These measurements discussed above have demonstrated the quality of the flow in the Aerodynamic Characterization Facility and it will surely be a valuable facility for applied and fundamental studies of the MAV aerodynamics. Additional measurements reported in Albertani

et al (2008) along with ongoing further measurements demonstrate that in addition to steady flow the facility will be able to simulate gusting phenomena that one might find in the urban environment.

## AERODYNAMIC AND STRUCTURAL RESEARCH ACTIVITIES

Figure 20 outlines the aerodynamic and structural research areas considered for MAV with flexible and morphing wing structures

Figure 20. Aerodynamic and Structural Characterization of Flexible and Morphing MAV's



- [a] Albertani, R., Babcock, J., "Analysis of Wind Tunnel Unsteady Aerodynamic Data of Flexible Micro Air Vehicle Wings," 26th *AIAA Applied Aerodynamic Conference*, Honolulu, HI, August 18-21, 2008.
- [b] Albertani, R., "Experimental Characterization of Microflaps," 2<sup>nd</sup> *NWF MAV08 Workshop*, University of Florida REEF, Shalimar, May 27-29, 2008.
- [c] Albertani, R., "A Wind Tunnel Study of Gurney Flaps applied to a Micro Aerial Vehicle," *AIAA Journal*, Volume 46, Number 6, June 2008.
- [d] Hu, H., Abate, G., Albertani, R. "An Experimental Investigation on Flapping Flexible Membrane Wings," abstract submitted for the 47<sup>th</sup> *AIAA Aerospace Sciences Meeting*, Orlando, FL, January 5-8, 2009.

- [e] Albertani, R., Khambatta, P., Ukeily, L., Cattafesta, L., Oyarzun, M., Abate, G., "Validation of an Aerodynamic Characterization Facility," abstract submitted for the 47<sup>th</sup> AIAA Aerospace Sciences Meeting, Orlando, FL, January 5-8, 2009.

## EXPERIMENTS ON MICRO-FLAPS

The experiments were conducted at the low-speed low-turbulence wind tunnel at the University of Florida. Two flaps configuration with the same height but different spanwise lengths were tested on a wing with a MAC of 0.1073 m, a wingspan of 0.377 m, and an aspect ratio of 3.78. The airfoil has a mildly reflexed, very-thin section with a thickness of 0.90 mm and a camber of 6 % at 25 % MAC. The wind tunnel tests consisted of angle-of-attack (AOA) sweeps at 73,300 and 95,200 Reynolds numbers based on the MAC including the clean wing.

The experiments conducted provided evidence that by using a Gurney flap on a MAV wing there exists a beneficial effect on lift, a reduction in drag in certain conditions, and an increase in maximum lift-to-drag ratio compared to the clean airfoil. Figure 21 shows the increase of lift coefficient of the wing with small (50% b) and large (75% b) Gurney flaps in respect to the clean wing, at a free stream Reynolds number of 95,200. The same figure suggests a slight increase of the lift curve slope for the wing with flap and a decrease of the stall angle and the angle for zero lift for the wings with flaps.

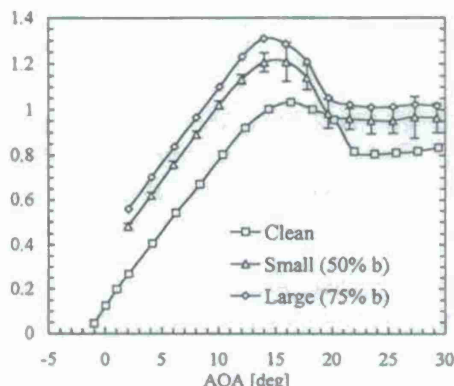
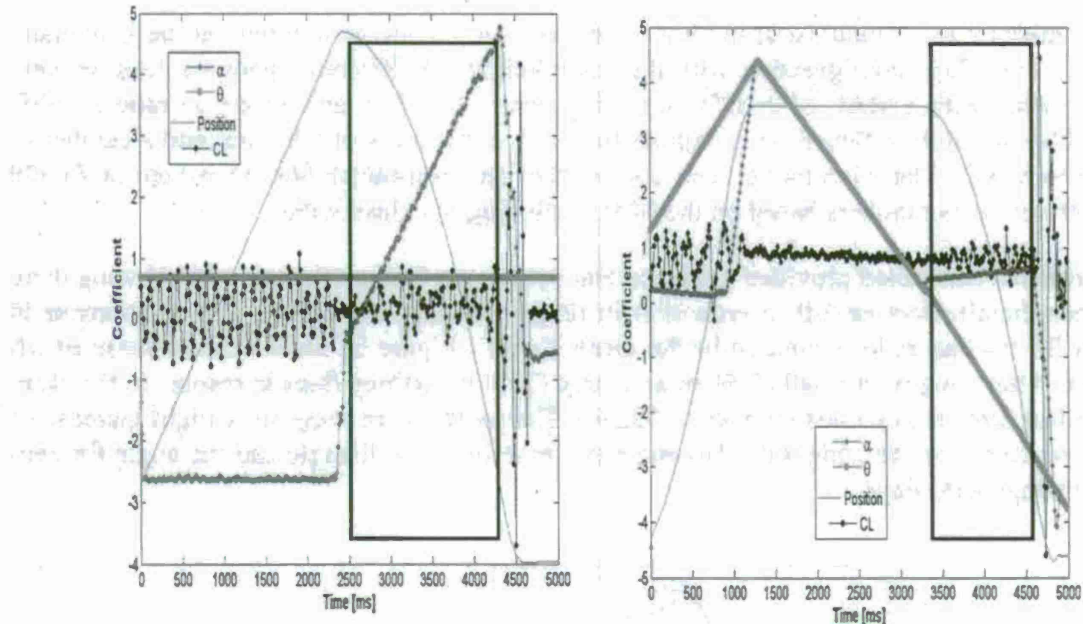


Fig. 21. Lift for clean wing and with 2.8% MAC Gurney flaps.

## PASSIVE AEROELASTIC WINGS IN UNSTEADY CONDITIONS

Micro air vehicles rigid and passive compliant wings were tested in unsteady conditions at the REEF low-speed low-turbulence wind tunnel equipped with a two degrees-of-freedom dynamic test rig. The motion, estimated by an inverse kinematics model that solves for the desired testing conditions, is provided by two ironless magnetic linear motors. This facility permits, for the first

time in applications to micro air vehicles, the measurement of the two individual components of the rotary damping moment. The coefficients due to rate of change of angle of attack were measured by oscillating the model in pure plunging motion. The coefficients due to pitch rate were measured during pitching motion, as illustrated in Fig. 22. To elucidate the correlation between the wings structural deformations and the aerodynamic damping characteristics, rigid and flexible identical wings at different levels of wing membrane tension were tested.



**Fig. 22. Combined plot with the model AOA, pitch angle and lift coefficient versus time. Left: pure plunging test. Right: pure pitching case. The position of the model is also displayed (light blue line). The rectangle shows the area used for data post-processing.**

The latex elastic membrane wing skin displacements are measured using the visual image correlation therefore the pre-tension strain state was characterized prior the aerodynamic tests, as illustrated in Fig. 23.

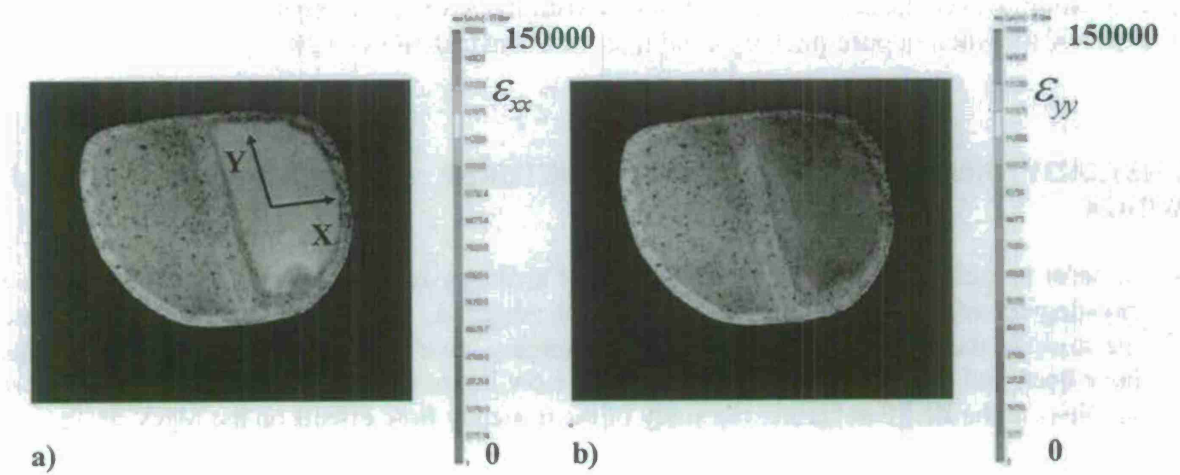


**Fig. 23.** Contour plots showing the experimental values of the wings elastic membrane strain state in wind-off conditions for the high pre-tension case. The strains are: a) in the x direction and b) in the y direction; c) and d) in the low

The data stored during the tests include the time histories signals from the six channels of the wind tunnel sting balance and the position of the two linear motors. Figure 24 shows the lift coefficient time histories for the case of pure pitching. The kinematics test conditions are characterized by the pitch angle varying linearly from  $23.0^{\circ}$  to  $13.0^{\circ}$ , a constant angle-of-attack (AOA) of  $18.62^{\circ}$  (nominally  $18^{\circ}$ ) and a wind tunnel free stream velocity of 10 m/s.

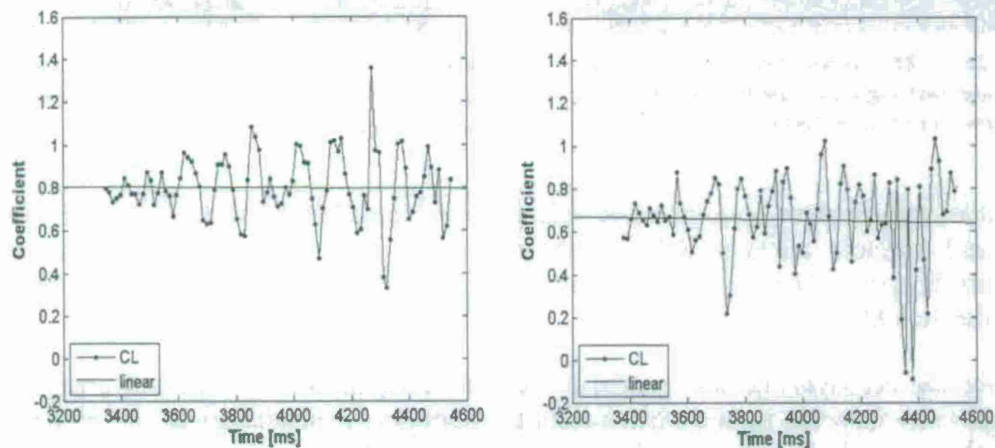


**Fig. 24.** Lift coefficient time histories. The plots represent the pure pitching case (constant AOA) for the rigid wing (left) and flexible wing (right). The flexible wing membrane is the high pre-tension condition.

The dynamic lift coefficients compare properly with the static counterparts with few anomalies as a lack of lift when in pure-pitching conditions at a constant AOA of  $18^{\circ}$ .

## UNSTEADY AERODYNAMICS AND STRUCTURAL DYNAMICS FOR FLEXIBLE WINGS

- In order to facilitate the testing of the effects of unsteady features of the MAV type airfoils a two-degrees-of freedom rig, Fig. 25 and 26, was designed. This rig was designed to facilitate the study of the effects of dynamic rotation, plunging, pure pitching and flapping. These rigs have been and will continue to be used in the Low Reynolds number wind tunnel and other facilities at the REEF to further the study of the unsteady flow effects on the MAV designs.

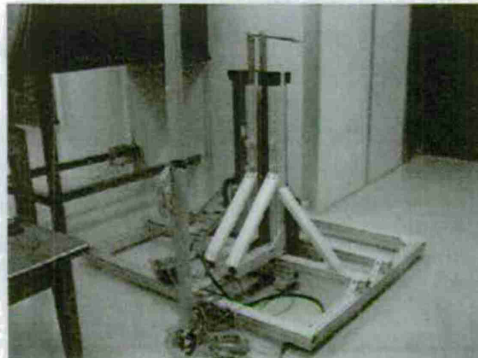


Fig. 25. The two-degrees-of freedom dynamic test rig assembled at the side of the new wind tunnel test enclosure.



Fig. 26. The one-degree-of freedom dynamic test rig in operation in the small wind tunnel.

Wind tunnel experiments on a powered micro air vehicle (MAV) with various flexible wing designs and variable elevator deflections proved effective for obtaining the aerodynamic coefficients in forms of linear regression models and investigating the mutual dependencies between the variables [2].

Models for the aerodynamic and propulsion coefficients, plotted in Figure 27, were obtained from multi-factorial wind tunnel experiments the nonlinear dependences of the propeller speed on the angle-of-attack, free stream velocity and elevator angle.

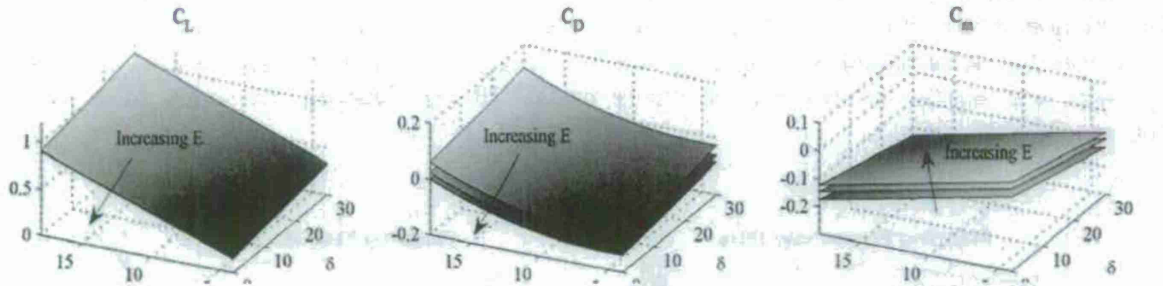


Fig. 27. Aerodynamic coefficient response surfaces for 6, 7, and 8 volts of input power to the DC micro motor.

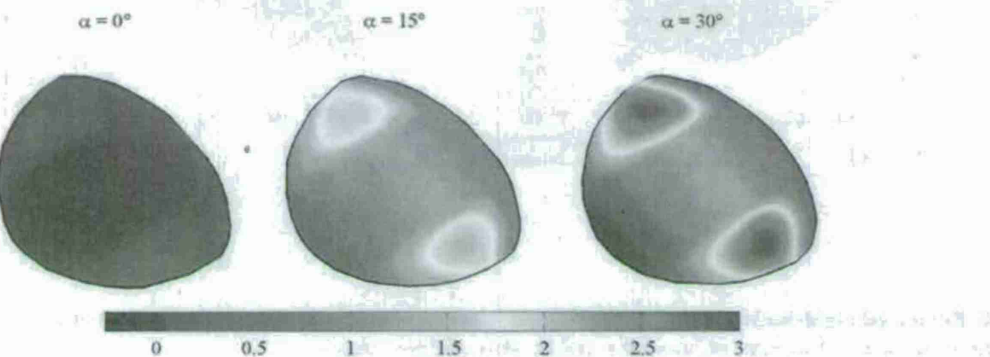


Figure 28. Time-averaged membrane displacements (mm) of the wing with a high pre-tension.

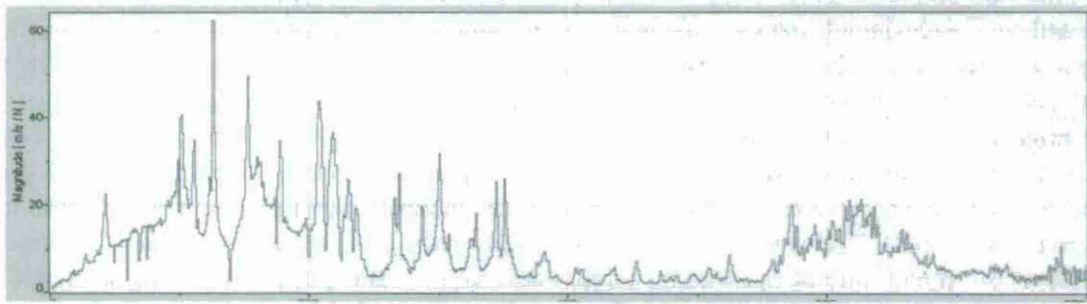
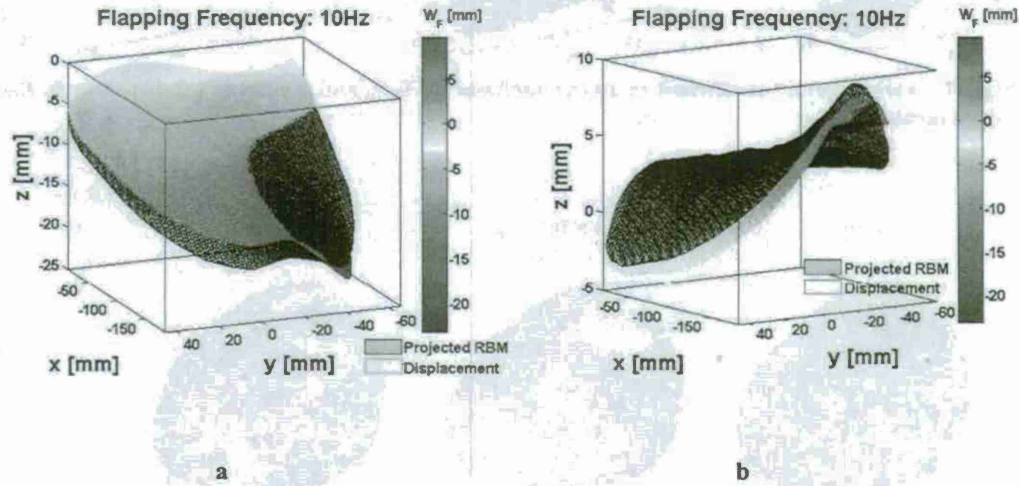


Fig. 29. Average spectrum (velocity/force) from LDV testing of membrane wing with high pre-tension.

Experiments were also carried out to evaluate the fundamental structural dynamics parameters (mode shapes, natural frequencies, and modal damping) of membrane MAV wings [3]. Bench vibrations tests (dry tests) and naturally induced vibrations measurements in a wind tunnel were performed on 15 cm wings with different levels of elastic membrane pre-tension. The average wing membrane out-of-plane deformations in wind tunnel tests are presented in Figure 28 for three angles of attack and at a free stream velocity of 9.5 m/s. The average spectrum in terms of velocity/force in natural induced vibrations is depicted in Figure 29 for the case with high membrane pre-tension. Results show an acceptable experimental accuracy for the modal parameters.

An experimental method based on dynamic visual image correlation and homogeneous transformation matrix post-processing was developed for decoupling the kinematics of wing motion from the deformation of a flapping flexible wing [4]. Figure 30 displays the combined wing twist and elastic deformation occurring at the 10 Hz flapping frequency of a latex membrane flexible wing.



**Fig. 30, Projected rigid-body-motion plotted against measured displacement for a membrane latex flapping wing at a) Start of up-stroke and b) Start of down-stroke.**

The primary objective of the UA effort was to study how a flexible (latex) membrane, similar to those used on UF-designed MAVs, affects the wake structure of flat and cambered plates at low  $Re$ . Past and recent research has shown that passive geometric changes and flexibility in the wing structure can improve MAV performance and alleviate sensitivity to flow disturbances. At higher angles-of-attack (AOA), the extension and/or passive vibration of the membrane could assist in the reattachment of the leading-edge shear layer and decrease wake width and drag. Figures 31 and 32 shows the two basic wing designs studied: perimeter reinforced (PR) and batten reinforced (BR). The latter does not have a rigid trailing-edge and, thus, does not prevent vibration of the membrane at the trailing-edge. High aspect ratio plates ( $AR = 8$ ), designed to minimize the tip effects, with multiple membrane cells and rounded leading-edges were tested at  $Re=45,000$ .

Surface and flow visualization confirmed leading-edge separation and reattachment on the solid flat plate for small AOA (see figure 32). The separation bubble increased with AOA, becoming fully separated at angles greater than  $8^\circ$ . For the cambered plates, the onset of leading-edge separation occurred at a positive AOA but slightly negative local leading-edge AOA relative to the free stream flow. Based on the jump in wake width, the flow appeared fully separated on the cambered plate at  $6^\circ$  AOA. The hot-wire wake surveys quantified velocity deficit and turbulence

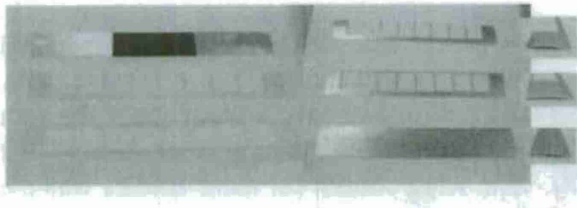


**Fig. 31.** Flat and cambered (6%) membrane plates

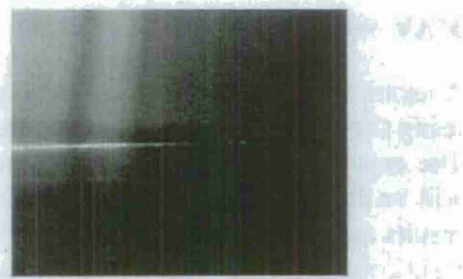


**Fig. 32.** Separation bubble on a flat plate at 2°.

intensity profiles as well as width and local drag coefficients. Fig. 33 is a comparison of the flat plate wake width at 50% velocity deficit (left) and local drag coefficient (right) for the flat plate. For the PR wing, there was a slight increase in wake width, local drag and turbulence intensity for  $\text{AOA} < 6^\circ$ . Slight improvement occurred at  $7^\circ$ , but the global characteristics were relatively the same at  $8^\circ$  (near full separation). The wake structure was vastly different for the BR wing due to trailing-edge flapping. While the wake deficit was lower than that of the PR and solid wings, the wake width, local drag and turbulence intensities were significantly increased, especially at small AOA. By  $8^\circ$ , the global characteristics were similar to that of the PR and solid plates. Scalloping the trailing 20% of the BR membrane showed considerable improvement in the local drag coefficient (based on the shortened local chord). This was due primarily to the substantial decrease in the wake deficit magnitude. The wake width, however was greater than that of the solid and PR wing, indicating trailing-edge fluctuation was still present but not as large as the unscalloped BR membrane. For the cambered plate, the presence of the PR and BR membrane decreased the wake width and local drag coefficient at  $6^\circ$  AOA (near full separation), but showed no improvement at lower or higher AOAs. Similar to the flat plate, scalloping the BR membrane on the camber plate significantly decreased the width and drag over the pre- and post-fully separated flow range ( $2^\circ$ - $14^\circ$ ).

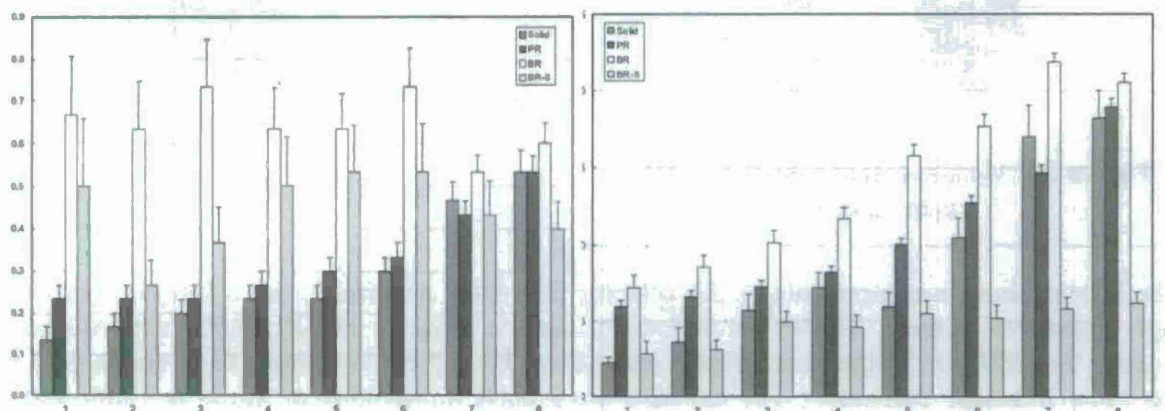


**Figure 33.** Effect of membrane geometry on wake width (left) and local drag coefficient (right) for  $\text{AOA} = 1^\circ$ - $8^\circ$ ; solid, PR, BR, BR-scalloped flat plate.

## MAV WING VELOCITY FIELD

A series of detailed flow measurements over a rigid low aspect ratio MAV wing were conducted using the REEF's time resolved particle Image Velocimetry system and low speed wind tunnels. The experimental effort has been reported in Khambatta (2008) and only a small set of the data will be discussed below. In addition we have used these results to compare to some steady CFD results and was reported in Khambatta et al (2008). The wing chosen for these studies was the rigid counterparts to those used for the wing deformation studies mentioned elsewhere and were developed by P. Ifju and his students. Below we will detail the comparison between the PIV and CFD results after a brief review of some details from the two techniques. Readers interested in a more elaborate discussion of the detailed PIV measurements should review Khambatta 2008.

The figure 34 below shows the planes in which the PIV measurements were acquired. Measurements for both configurations were taken at a free-stream velocity of 9.5 m/s corresponding to a Reynolds number of 75,000 based on the wing chord length of 0.124 m. Free-stream conditions were verified before the experiment by means of a pitot-static probe connected to a Heise (ST-2H) 0-0.5" of H<sub>2</sub>O, pressure transducer with an accuracy of 0.015% FS (~0.1 m/s). The time scale to ensure the capture of statistically independent data was calculated to be ~0.028 s, assuming that the largest conceivable scale is on the order of the wing-chord. This implies that the sampling frequency should be less than 35.5 Hz, to ensure statistically independent samples.

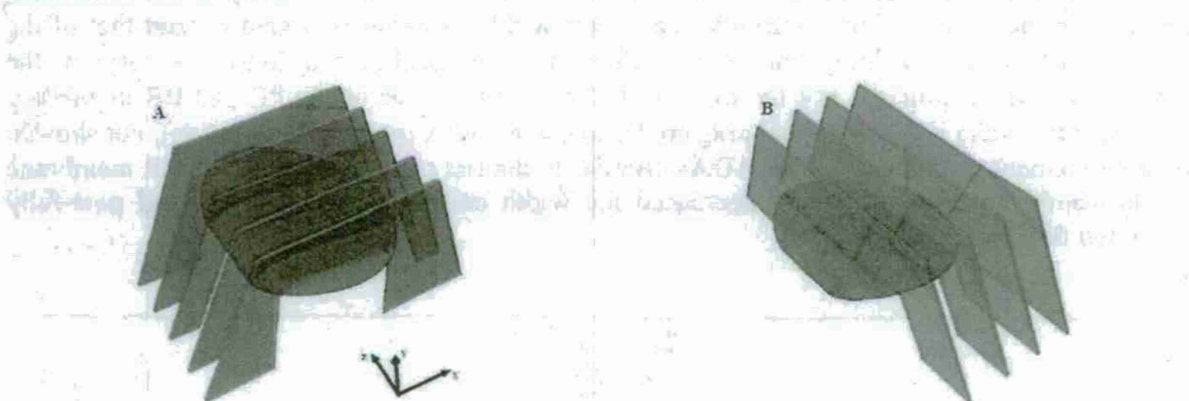


**Figure 34: Measurement planes for PIV experiments**

The instantaneous measurements of the velocity field were acquired using a Dantec Dynamics high speed PIV system. The PIV components include a Series 800-PIV/40G Nd:YAG laser system, two IDT XS-5 high speed digital cameras with f-2.8 Nikkor lenses and version 4.71 of the Flow Manager software. The cameras have pixel dimensions of 12 $\mu$ m x 12 $\mu$ m and a resolution of 1260x1024. For the 2-component PIV setup, the camera lens magnification was  $M = 0.11$  and for the 3-component PIV setup, the average lens magnification was  $M = 0.09$ . A Laskin nozzle seeding generator from Dantec Dynamics (model 10F03) was used to atomize olive oil and produce seeding particles expected to be in the size range of 1-5  $\mu$ m. The seeding

particles are introduced into the flow just upstream of the inlet-contraction to the wind tunnel in such a manner that they produced a region of uniformly seeded flow all around the wing within the test section. Given the magnification of the lenses, an  $f\# = 2.8$ , and the wavelength of the laser,  $\lambda_L = 532$  nm, one can calculate the diffraction limited spot size,  $d_{sp}$  for a single lens (Meinhart and Wereley, 2003) using the following relationship,

$$d_{sp} = 2.44(M+1)\lambda_L f^{\#}. \quad (1)$$

The particle image diameter,  $d_r$  on the pixel array is then calculated using equation (2), where  $d_p$  is the diameter of the seeding particles (Westerweel, 2000):

$$d_r \cong (M^2 d_p^2 + d_{sp}^2)^{\frac{1}{2}} \quad (2)$$

For these calculations,  $d_p$  was assumed to be 5.0 microns, based on specifications provided by Dantec. Based on equations (1) & (2),  $d_{sp}$  &  $d_r$  were calculated to be 4 microns. For cases where  $M \ll 1$ ,  $d_r \rightarrow d_{sp}$  (Westerweel, 2000), and therefore, our ratio of particle image diameter to pixel dimension was 0.33.

For 2-component PIV, the width of the image window was 0.14 m and to be able to apply an interrogation area of 16pix x 16pix (3.55 mm square) to an image pair, the time delay between successive images in a pair was set at 35  $\mu$ s. For 3-component PIV, the width of the image windows were 0.1 m and an interrogation area of 32pix x 32pix was used (2.54 mm square). To obtain statistically independent data, the frame rate was set at 35.0 Hz. A sample of the convergence is taken from the measurements at a point in the freestream at  $\alpha = 15^\circ$  and is shown in Figure 35, the data has been normalized by the mean velocity at that point (calculated from 810 samples). It can be seen that once the sample size exceeded 600, the variations in the mean velocity were less than 0.2% of the mean. After the raw images had been obtained, a low pass Gaussian filter with a width of 0.1 was applied to the data and the images were then processed with 50% overlap. A series of high speed measurements were acquired at 400 Hz in an effort to resolve the temporal behavior of the more energetic features of the flow. While the system is capable of sampling at up to 512 Hz in double-frame mode, measurements collected above 400 Hz appeared to suffer from inadequate optical conditions. These high speed measurements were collected under limited conditions: at  $\alpha = 25^\circ$  &  $30^\circ$  in the  $x$ - $y$  plane at  $2b/z = 0$  & 1 (2-component PIV); at  $\alpha = 30^\circ$  in the  $z$ - $y$  plane at  $c/x = 0.5, 0.87$  &  $1.1$  (3-component PIV).

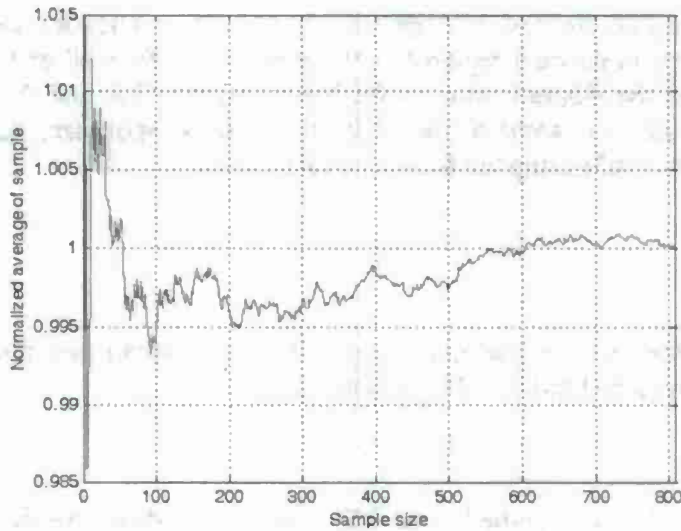


**Figure 35: Convergence plot of normalized mean vs. sample size.**

All measurements (2-component, 3-component configurations, statistically independent and high speed), comprised 810 samples. These measurement locations described should provide a sufficient description of the flow topology surrounding this MAV wing to be compared with numerical simulations, and provide some insight into the non-linear lifting characteristics of low Reynolds number airfoils, in particular, the vortices near the wing tips and the regions of separated flow on top of the wing. Table 3 and Table 4 present the locations where PIV measurements were taken around the wing.

Angles of attack	0°	10°	15°	18°	20°	21°	25°	30°		
Span-wise locations, $2z/b$ (2-component PIV, $x-y$ plane)	0	0.167	0.25	0.33	0.5	0.67	0.75	0.83	0.92	1.0

**Table 3: Angles of attack and span-wise locations for 2-component PIV measurements.**

Angles of attack	15°	18°	21°	25°	30°					
Chord-wise locations, $x/c$ (3-component PIV, $y-z$ plane)	0.3	0.4	0.5	0.6	0.7	0.8	0.9	1.0	1.1	1.2

**Table 4: Angles of attack and chord-wise locations for stereoscopic PIV measurements.**

## NUMERICAL METHODS

The three-dimensional, incompressible Navier-Stokes equations written in curvilinear coordinates are solved for the steady, laminar flow over the MAV wing. The fuselage, stabilizers, and propeller are not taken into account. The computational domain can be seen in Figure 36, with the MAV wing (red) enclosed within. Inlet and outlet boundaries are marked by the flow vectors: velocity is specified at the inlet, while a zero pressure condition is enforced at the outlet. The configuration shown in Figure 36 is for simulations at a model inclination of  $0^\circ$ . For non-zero angles, the lower and upper surfaces will also see a mass flux. The side walls are modeled as slip walls, and thus no boundary layer forms. The dimensions of the computational domain are given in terms of the root chord, and are placed far enough away from the MAV surface so as not to significantly affect the aerodynamics. As no flow is expected to cross the root chord of the wing (no propeller is modeled), symmetry is exploited by modeling only half of the computational domain (the plane of symmetry is also modeled as a slip wall). A detailed view of the resulting structured mesh is given in Figure 36. 210,000 nodes fill half of the computational domain, with 1300 nodes on the wing surface.

In order to handle the arbitrarily shaped geometries of a micro air vehicle wing, the Navier-Stokes equations must be transformed into generalized curvilinear coordinates:  $\xi(x,y,z)$ ,  $\eta(x,y,z)$ ,  $\zeta(x,y,z)$ . This transformation is achieved by (Tannehill et al, 1997):

$$\begin{bmatrix} \xi_x & \xi_y & \xi_z \\ \eta_x & \eta_y & \eta_z \\ \zeta_x & \zeta_y & \zeta_z \end{bmatrix} = \frac{1}{J} \cdot \begin{bmatrix} f_{11} & f_{12} & f_{13} \\ f_{21} & f_{22} & f_{23} \\ f_{31} & f_{32} & f_{33} \end{bmatrix} \quad (3)$$

where  $f_{ij}$  are metric terms, and  $J$  is the determinant of the transformation matrix:

$$J = \frac{\partial(x,y,z)}{\partial(\xi,\eta,\zeta)} \quad (4)$$

Using the above information, the steady Navier-Stokes equations can then be written in three-dimensional curvilinear coordinates (Shyy, 1994). The continuity equation and u-momentum equation are presented here in strong conservative form, with the implication that the v- and w-momentum equations can be derived in a similar manner.

$$U_\xi + V_\eta + W_\zeta = 0 \quad (5)$$

$$\begin{aligned} \frac{\partial(\rho \cdot U \cdot u)}{\partial \xi} + \frac{\partial(\rho \cdot V \cdot u)}{\partial \eta} + \frac{\partial(\rho \cdot W \cdot u)}{\partial \zeta} = & \frac{\partial}{\partial \xi} \left[ \frac{\mu}{J} \cdot (q_{11} \cdot u_\xi + q_{12} \cdot u_\eta + q_{13} \cdot u_\zeta) \right] \\ & + \frac{\partial}{\partial \eta} \left[ \frac{\mu}{J} \cdot (q_{21} \cdot u_\xi + q_{22} \cdot u_\eta + q_{23} \cdot u_\zeta) \right] + \frac{\partial}{\partial \zeta} \left[ \frac{\mu}{J} \cdot (q_{31} \cdot u_\xi + q_{32} \cdot u_\eta + q_{33} \cdot u_\zeta) \right] \\ & - \left[ \frac{\partial(f_{11} \cdot p)}{\partial \xi} + \frac{\partial(f_{21} \cdot p)}{\partial \eta} + \frac{\partial(f_{31} \cdot p)}{\partial \zeta} \right] \end{aligned} \quad (6)$$

where  $\rho$  is the density,  $p$  is the pressure,  $\mu$  is the viscosity,  $q_{ij}$  are parameters dictated by the transformation (expressions can be found in Shyy, 1994), and  $U$ ,  $V$ , and  $W$  are the contravariant velocities, given by the flux through a control surface normal to the corresponding curvilinear directions:

$$\begin{aligned} U &= f_{11} \cdot u + f_{12} \cdot v + f_{13} \cdot w \\ V &= f_{21} \cdot u + f_{22} \cdot v + f_{23} \cdot w \\ W &= f_{31} \cdot u + f_{32} \cdot v + f_{33} \cdot w \end{aligned} \quad (7)$$

In order to numerically solve the above equations, a finite volume formulation is employed, using both Cartesian and contravariant velocity components (Tannehill et al, 1997). The latter can evaluate the flux at the cell faces of the structured grid and enforce the conservation of mass. A second order central difference operator is used for computations involving pressure/diffusive terms; a second order upwind scheme handles all convective terms (Thakur et al, 2002).

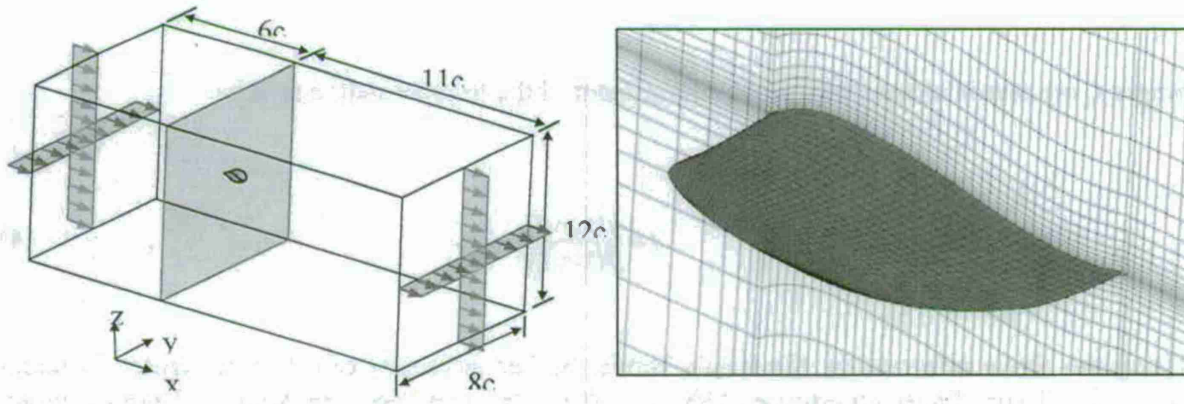


**Figure 36: CFD computational domain (left) and detail of mesh near wing surface (right).**

Figure 37 through Figure 41 allow for a qualitative comparison and discussion about the numerical and experimental results from 2-component PIV at  $\alpha = 10^\circ, 15^\circ, 21^\circ$  and  $30^\circ$  and at  $2z/b = 0$  & 1. Due to the dihedral in the wing and because the camera in the 2-component PIV setup was perpendicular to the  $x$ - $y$  plane, the flow adjacent to the wing surface could not be characterized in certain regions, (as is indicated by a white space between wing profile and the

data). These regions do not exceed  $0.04c$  in height above the wing surface. The PIV results were obtained with one digital camera capturing images at 35 Hz at a resolution of  $1260 \times 1024$  pixels and at a distance of 0.625 m from the plane of illumination.

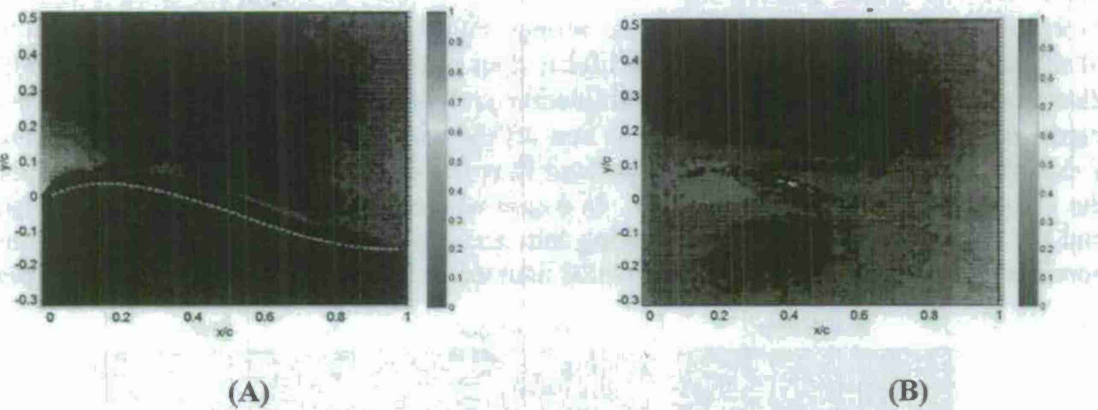


**Figure 37: A).** Percentage distribution of estimated vectors for  $\alpha = 10^\circ$  &  $2z/b = 0$ , and **B).**  $2z/b = 1$ .

For  $\alpha = 10^\circ$  and  $2z/b = 0$ , Figure 37 A, shows that the number of estimated vectors is less than 10% of the total number of samples for the majority of the area over the wing. The data near the leading edge has a region where the percentage of estimated vectors gets significantly larger, but this may be attributed to the fact that there is poor correlation between the image pairs due to those locations being close to the boundary of the image frame. Figure 37 B shows a similar distribution of the percentage of estimated vectors for  $\alpha = 10^\circ$  and  $2z/b = 1$ . It is observed that there are a large percentage of estimated vectors in a thin region that is adjacent to the perimeter of the wing-tip. This is attributed to the edge of the wing-tip that reflected a portion of the light from the laser sheet illuminating the  $x$ - $y$  plane immediately adjacent to it, causing a bloom effect on the sensor array. The estimated vectors for the other cases have a similar distribution over the vector map as the cases shown in Figure 37.

Looking at the time-averaged data in Figure 38 through Figure 41, there is indication of an acceleration of the flow over the wing at the point of greatest camber, as expected, after which there is some indication of separation as the flow over the wing comes in contact with an adverse pressure gradient. The numerical and experimental data appear to correlate well on this aspect. However, the numerical data indicates a stronger region of re-circulation sitting within the reflexed region of the airfoil ( $\sim x/c = 0.75$ ), which is not visible in the experimental data (for  $\alpha = 10^\circ$  &  $15^\circ$  at  $z/b = 0$ ). The flow over the reflexed region is clearly slowed down, and this might be indicative of a smaller separation bubble slightly more upstream than where the numerical model predicts it to be. Furthermore, for  $\alpha = 21^\circ$ , the numerical model predicts large scale separation over the wing and the experimental results indicate a much smaller region of re-circulation sitting just above the reflexed portion of the wing. At  $\alpha = 30^\circ$ , both, the numerical model and the experimental data indicate a large scale separation over the wing, but with varying results for the centers of the vortex cores at  $2z/b = 0$ .

For  $\alpha = 10^\circ, 15^\circ \& 21^\circ$  and  $2z/b = 1$ , the numerical model consistently predicts a slower velocity in the vortex tube as compared to the experimental data. The flow in this region is highly three dimensional, and it is possible that the experimental data was collected in a region where the strongest component of the velocity was in a stream-wise direction rather than normal to it. However, as can be observed in Figure 38 through Figure 41, the stream-wise component of the numerical data is also consistently slower in the vortex core as compared to the measured data. In the cases where  $2z/b = 1$  in Figure 38 through Figure 41, the stream-wise velocity in the core of the separation region appears to be higher than in the free-stream. This clearly indicates a discrepancy between the numerical simulation and the experimental results. However, the experimental results were collected  $\sim 2\text{-}3$  mm off the wing tip, (to avoid excessive blooming), in a region adjacent to the core of the separated flow region, where the stream-wise component of the velocity is greater than in the core. In a case where the vortex is  $\sim 12$  mm wide (Figure 42) and the core is only 3-4 mm wide, taking into account the laser sheet thickness ( $\sim 2$  mm), it is possible that the numerical and experimental data were collected from two different  $x\text{-}y$  planes.

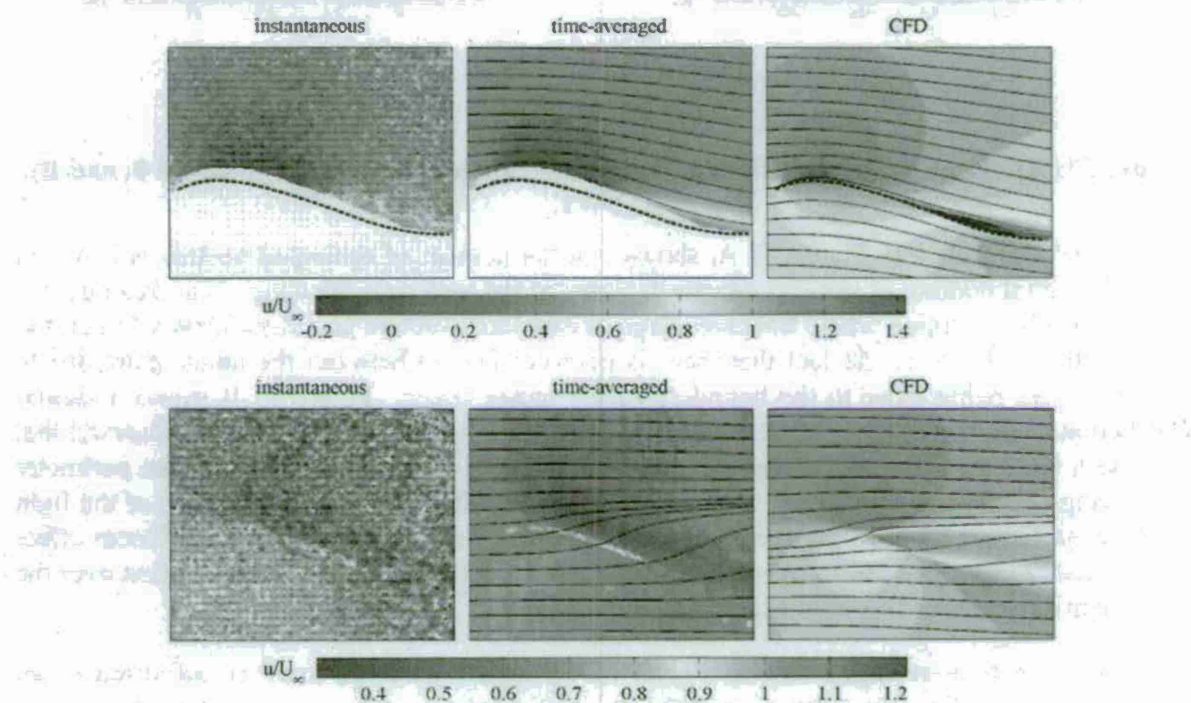


**Figure 38:** Normalized streamwise flow at  $\alpha = 10^\circ$ : instantaneous PIV (left), time-averaged PIV (center), and CFD (right). Span station  $2z/b = 0$  (top) and  $2z/b = 1$  (bottom).

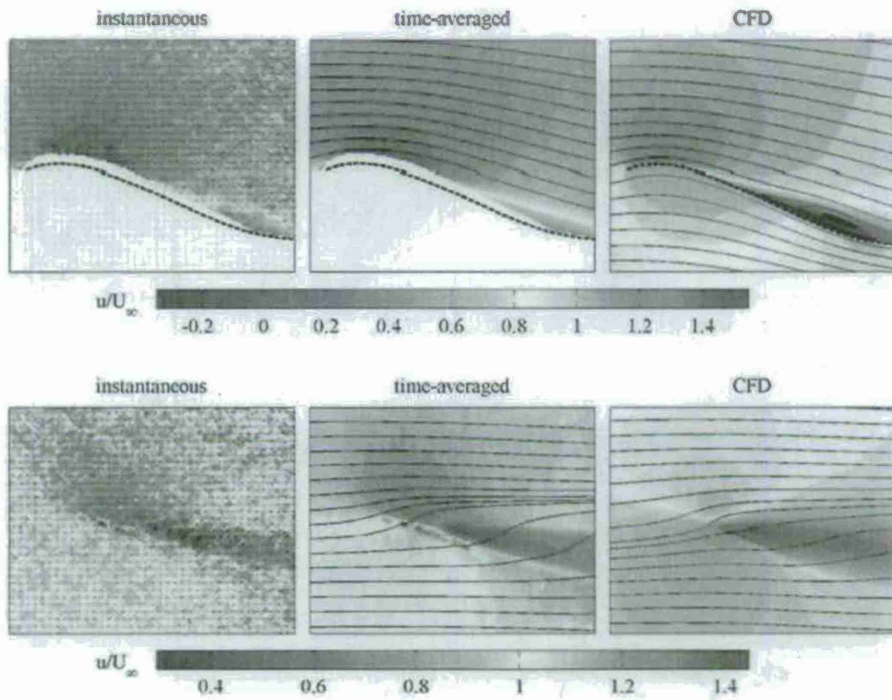


**Figure 39:** Normalized streamwise flow at  $\alpha = 15^\circ$ : instantaneous PIV (left), time-averaged PIV (center), and CFD (right). Span station  $2z/b = 0$  (top) and  $2z/b = 1$  (bottom).

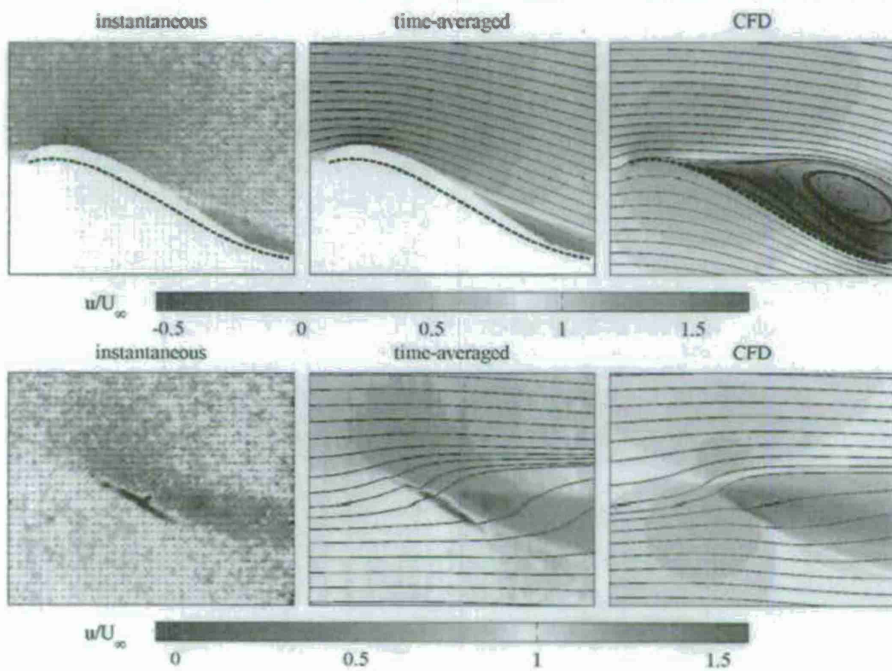


**Figure 40:** Normalized streamwise flow at  $\alpha = 21^\circ$ : instantaneous PIV (left), time-averaged PIV (center), and CFD (right). Span station  $2z/b = 0$  (top) and  $2z/b = 1$  (bottom).

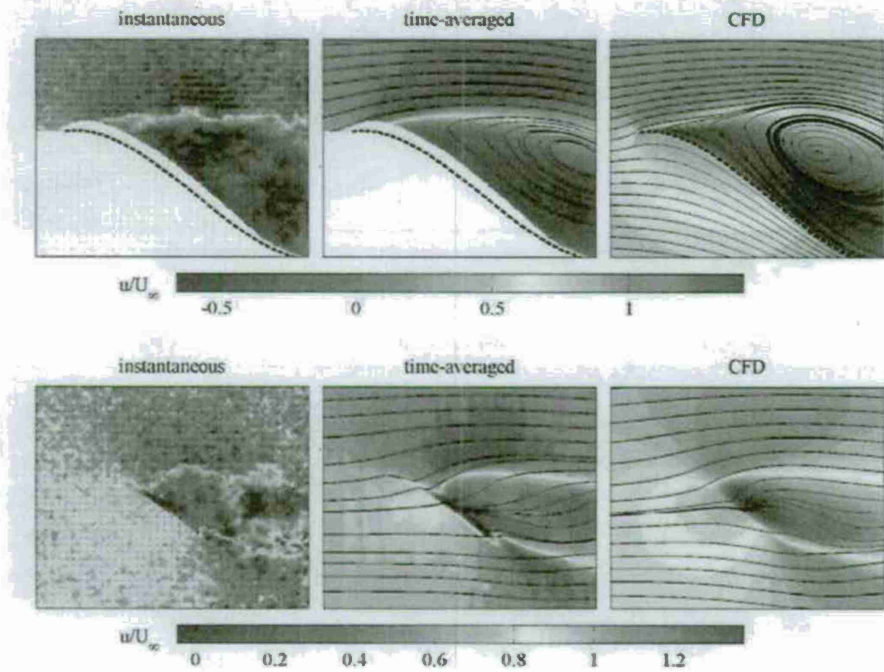


**Figure 41:** Normalized stream-wise flow at  $\alpha = 30^\circ$ : instantaneous PIV (left), time-averaged PIV (center), and CFD (right). Span station  $2z/b = 0$  (top) and  $2z/b = 1$  (bottom).

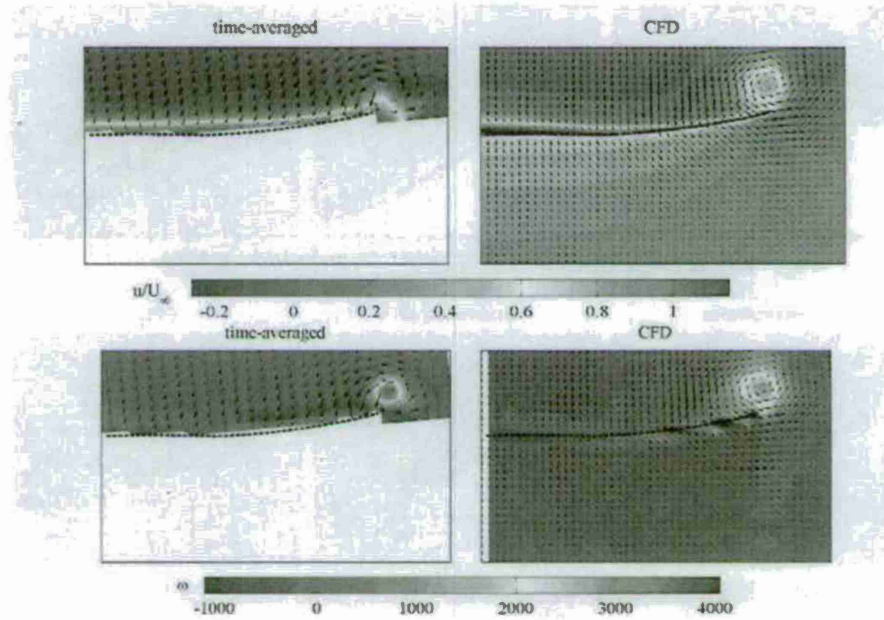


**Figure 42:** Normalized stream-wise flow (top) and vorticity (bottom) at  $x/c = 0.51$ ,  $\alpha = 15^\circ$ , with normal components indicated by the vector plot: time-averaged PIV (left), and CFD (right).

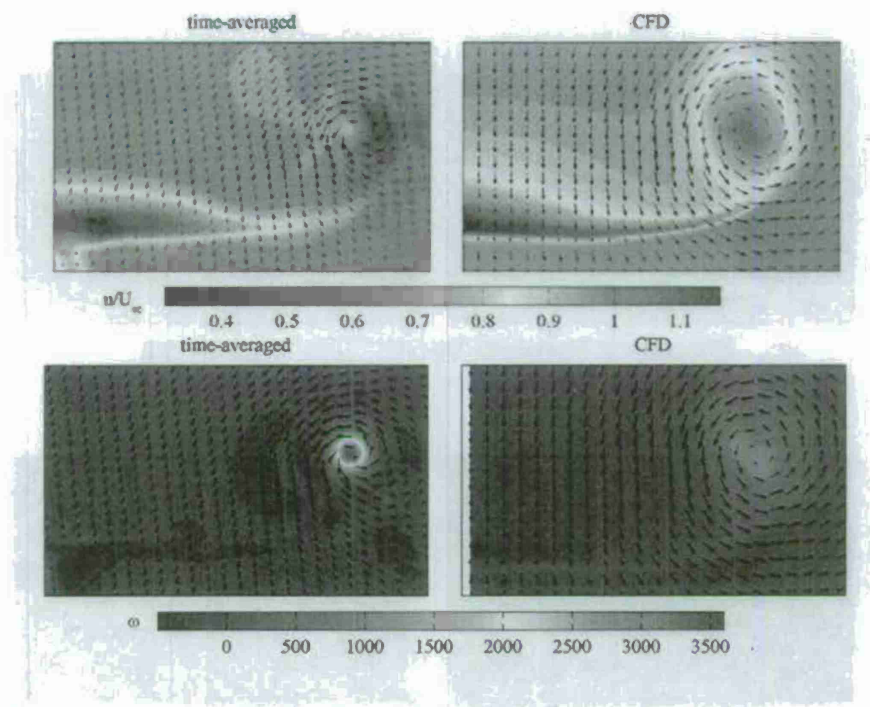


**Figure 43:** Normalized stream-wise flow (top) and vorticity (bottom) at  $x/c = 1.02$ ,  $\alpha = 15^\circ$ , with normal components indicated by the vector plot: time-averaged PIV (left), and CFD (right).

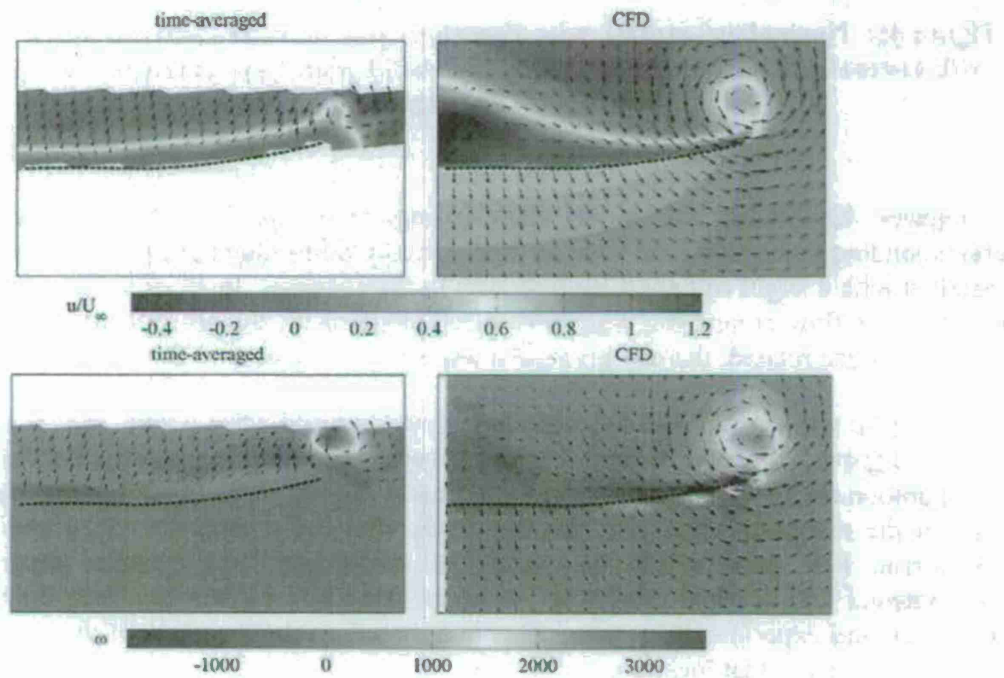


**Figure 44:** Normalized stream-wise flow (top) and vorticity (bottom) at  $x/c = 0.51$ ,  $\alpha = 21^\circ$ , with normal components indicated by the vector plot: time-averaged PIV (left), and CFD (right).

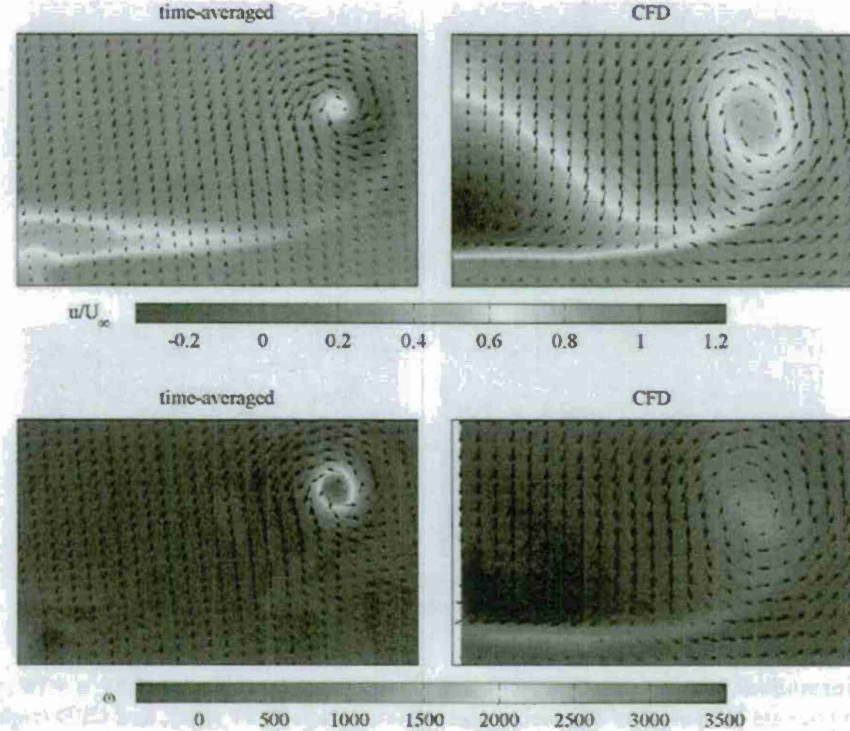


**Figure 45:** Normalized stream-wise flow (top) and vorticity (bottom) at  $x/c = 1.02$ ,  $\alpha = 21^\circ$ , with normal components indicated by the vector plot: time-averaged PIV (left), and CFD (right).

Figures 42 through Figure 45 show results from the 3-component PIV tests and the corresponding numerical data. During the collection of the experimental data, the wing had been installed with a slight roll angle with respect to the cameras. In an effort to correctly depict and compare the flow around the wing with a roll angle of  $0^\circ$ , the co-ordinate system and the flow field have been rotated, thereby giving the impression of a skewed flow field.

The wing tip vortices in these cases can be clearly seen and when observed over a period of time, appear to grow and shrink in size, alternating between wing-tips. In the  $\alpha = 21^\circ$  case, the region of separation on top and behind the wing is clearly smaller in magnitude in the experimental data than in the numerical data, and this correlates with the comparison done earlier with the 2-component PIV data, where the numerical model predicted massive separation and the experimental data showed otherwise. A quantitative comparison has been drawn between the numerical and experimental results in Table 5, based on the locations of the vortex core centers and the vorticity at that location.

The downward shift in the locations of the vortex cores with an increase in  $z/c$  is due to the downwash caused over the wing due to its angle of attack and geometry. Not only is there a downwash effect, there also appears to be a side-ways shift of the vortex core towards the center of the wing, this trend is observed in both, the numerical and the experimental data. The

vorticity at the wing-tips is also expected to increase with an increase in angle of attack, however, the experimental data indicates otherwise, showing a decay in the vorticity at the vortex center at  $\alpha = 21^\circ$  when compared at  $\alpha = 15^\circ$ .

Angle of attack, $\alpha$	Chord-wise location ( $z/c$ )	Location of vortex core		Vorticity ( $s^{-1}$ )
			$z$ (mm from origin)	
$15^\circ$	0.5	Experimental	78.8	2.1
		Numerical	75.5	4.0
$15^\circ$	1.0	Experimental	75.9	-8.8
		Numerical	71.4	-8.1
$21^\circ$	0.5	Experimental	79.0	-0.4
		Numerical	75.5	-1.4
$21^\circ$	1.0	Experimental	74.4	-13.8
		Numerical	71.4	-19.1

**Table 5: Comparison of vortex core locations and vorticity, between experimental and numerical results.**

## REFERENCES:

2. Albertani, R., DeLoach, R., Stanford, B., Hubner, J. P. Ifju, P., "Wind Tunnel Testing and Nonlinear Modeling Applied to Powered Micro Air Vehicles with Flexible Wings," accepted for publication on *AIAA Journal of Aircraft*, December 2007.
3. Albertani, R., Stanford, B., Sytsma, M. and Ifju, P., "Unsteady Mechanical Aspects of Flexible Wings: an Experimental Investigation Applied on Biologically Inspired MAVs," *MAV07 3rd US-European Competition and Workshop on MAV Systems*, SUPAERO, Toulouse, France, September 18-21, 2007.
4. Stewart, K., Albertani, R., "Experimental Elastic Deformation Characterization of a Flapping-Wing MAV using Visual Image Correlation," *MAV07 3rd US-European Competition and Workshop on MAV Systems*, SUPAERO, Toulouse, France, September 18-21, 2007.

## **Task 4: Control of Biologically-Inspired Morphing for Variable-Geometry MAV**

### **MILESTONES/STATUS:**

#### **First 9 Months/Status:**

- Complete analysis of aerodynamic shape-varying configurations (collaborate with REEF wind tunnel lab and REEF CFD researchers). (Completed)
- Analyze structural dynamics of vehicle with morphing implementations (Collaborate with AVCAAF researchers). (Completed)
- Develop framework to represent shape-dependent models (collaborate with GNV researchers). (completed)
- Conduct stability analysis for configurations within the framework (collaborate with GNV and AFRL researchers). (Completed)
- Implementation of configurations to alter CG and tail (collaborate with REEF rapid prototyping lab). (Completed)

### **GENERAL**

Under the leadership of Dr. Rick Lind from the University of Florida and Dr. Chakravarthy from the UF-REEF significant progress has been made in researching the effects of time-varying inertias on flight dynamics of an asymmetric variable-sweep morphing micro air vehicles. Mission capability can be enabled by morphing a micro air vehicles to optimize its aerodynamics and associated flight dynamics for each maneuver. Such optimization techniques often consider the steady-state behavior of the configuration; however, the transient behavior must also be analyzed. In particular, the time-varying inertias have an effect on the flight dynamics that can adversely affect mission performance if not properly compensated. These inertia terms cause coupling between the longitudinal and lateral-directional dynamics even for maneuvers around trim. A simulation of a variable-sweep aircraft undergoing a symmetric morphing for an altitude change shows a noticeable lateral translation in the flight path because of the induced asymmetry. Non linear dynamic equations including varying mass distributions were derived and applied to a variable wing sweep vehicle described below:

### **TIME-VARYING DYNAMICS OF MORPHING AIRCRAFT**

A study into the time-varying dynamics of the morphing wing, double section, variable-sweep MAV has been in progress. In this study, the time-varying counterparts of the conventional short period, phugoid, roll, spiral and dutch roll modes were researched. More specifically, if the MAV is hit by a disturbance at the same time while it is executing a morphing trajectory, this study characterizes the modes of the MAV at such times.

It is well known that the study of time-varying systems (even linear ones) is far more complex than those of LTI systems. For a LTV system, since the eigenvalues of the system matrix in general have no significance with regard to providing information of the system's stability or its

modal behavior, alternative techniques were explored. Several techniques have been proposed in the literature, but all of them suffer from some drawbacks or the other. Wu (1984) proposed a system of using (extended)  $x$ -eigenvalues and  $x$ -eigenvectors (using new definitions for these concepts); this method is good in that it can always diagonalize the system matrix (resulting in decoupled modes); however it has the drawback that the  $x$ -eigenvalues and  $x$ -eigenvectors are not unique. Indeed, each  $x$ -eigenvalue,  $x$ -eigenvector pair makes some sense only as a pair, but not individually. Also, if the time-variation is for a finite duration, these  $x$ -eigenpairs do not necessarily merge with the LTI eigenvalues and eigenvectors that occur at the start/end of the time-variation. Kamen (1988) proposed a factorization approach to determine the time-varying poles (and thus the modes) of an LTI system. This method involves the solution of a nonlinear time-varying Riccati equation. This method, when it works, is most elegant; in particular, its time-varying poles can be related with the LTI poles that occur at the start time of a finite duration morphing, but at other times, the Riccati equation can have unstable solutions, and this causes the time-varying poles to diverge to negative  $\infty$ . Zhu (1991) proposed notions of parallel D spectra and series D spectra, and used these notions to diagonalize the system matrix (in addition to transforming to other canonical forms) but they too have the problem that the time-varying poles can, under certain conditions diverge to negative  $\infty$ . O'Brien and Iglesias (2001) proposed notions of time-varying poles that rely on a QR factorization of the state transition matrix; the good feature of this notion is that the time-varying modes in this case are always bounded, however a drawback is that this notion does not necessarily result in being able to decouple the modes (i.e. it does not always diagonalize the system matrix, even though it may actually be possible to do so). Also, these poles are not necessarily related to the LTI poles that occur at the start/end times of a finite duration morphing.

Using Kamen's definition of time-varying poles, the short period modes of the morphing MAV, for two different morphing trajectories are as shown in Figures 46 and 47. For purposes of comparison, the frozen time LTI poles are also shown alongside. The feature of these graphs is that when the morphing occurs from +30 deg to -30 deg over a span of 2 seconds (Figure 46), the LTV poles remain bounded and finite. However, when the direction of the morphing is reversed (i.e. the same MAV morphs from -30 deg to +30 deg), the LTV poles become infinite (Figure 47). An investigation was conducted into this phenomenon using a phase plane analysis of the nonlinear, time-varying Riccati equation. Using this analysis, it is possible to identify precisely the sets of initial conditions under which these LTV poles (and those of an arbitrary second order time-varying system) diverge to  $\infty$ . Under such circumstances an optimization-based approach in order to determine the LTV poles using only output measurements was explored. The optimization based LTV poles are found to remain finite under all circumstances (even when Kamen's LTV poles become infinite); additionally they compare reasonably well with Kamen's LTV poles when the latter is also finite.

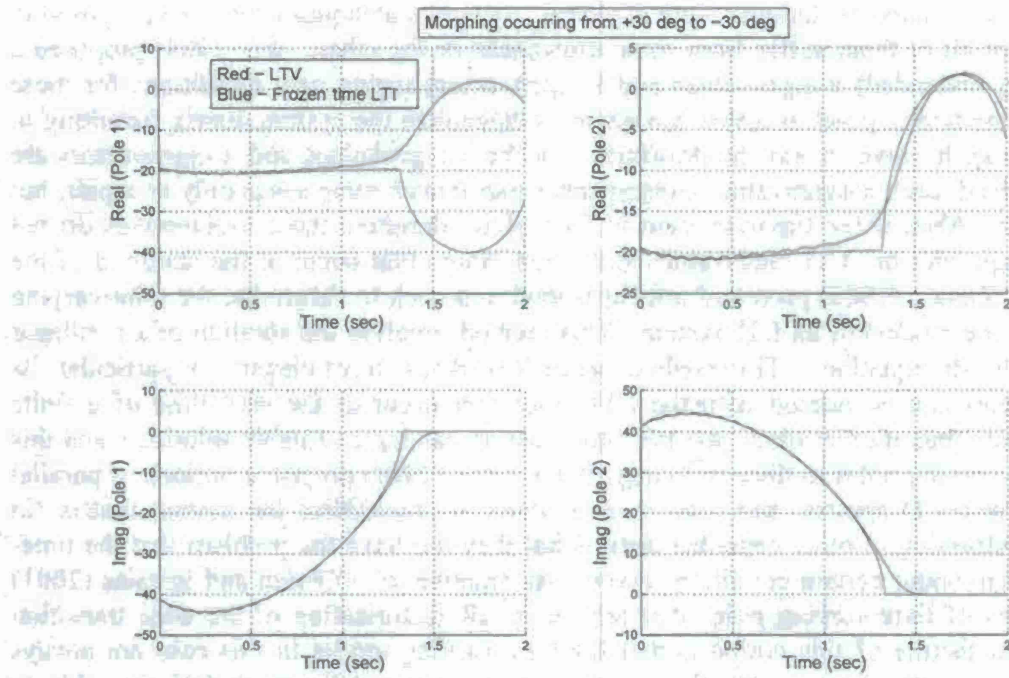


**Figure 46.** LTV short period right poles (red) and frozen time LTI poles (blue) shown while morphing occurs from +30 deg to -30 deg. The LTV poles remain bounded throughout the duration of the morphing.

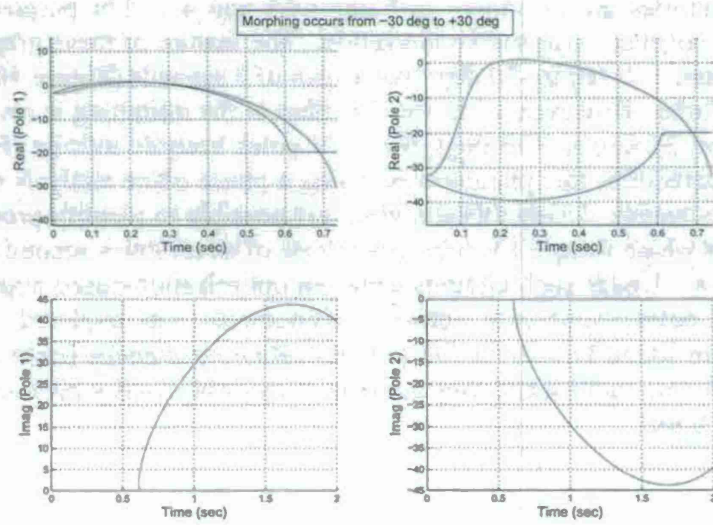


**Figure 47.** LTV short period right poles (red) and frozen time LTI poles (blue) shown while morphing occurs from -30 deg to +30 deg. The real part of the LTV poles starts to grow unboundedly after  $t = 0.7$  sec.

## COMPUTATION OF POLES FOR LTV SYSTEMS

The fact that the analysis of linear time varying (LTV) systems is substantially different from that of linear time invariant (LTI) systems has been well established [6]. For example, eigenvalues of the system matrix (that govern the stability of LTI systems) have no significance whatsoever when it comes to the stability of LTV systems [9]. Due to the possibility of nonexponential responses for LTV systems, the connections between asymptotic stability and bounded-input bounded-output stability for such systems are not as straightforward as they are for LTI systems [5]. The simple notions of controllability/observability in LTI systems assume the much subtler notions of total controllability, complete controllability, uniform controllability/observability for LTV systems [6]. In short, the analysis of LTV systems requires considerably enhanced machinery when compared to that used in the analysis of LTI systems.

In [4], the author defines a notion of poles and zeros of LTV systems. For an LTI system, use of the Laplace transform converts the system to an algebraic representation – whose numerator and denominator can then be factorized in a conventional manner, to obtain the poles and zeros of the system. For an LTV system, however, use of the Laplace transform does not (in general) convert the system to an algebraic representation; therefore special factorization techniques (as those discussed in [8]) that work directly on the ODEs are to be invoked. Other notions of poles and zeroes of LTV systems have also been discussed in [7], [11], [12]. In [7], the authors compute the LTV poles subsequent to performing a QR decomposition of the state transition matrix of the system. In [11], [12], the author discusses the notion of Parallel D spectra and Series D spectra.

This research performed a detailed phase-plane analysis on the differential Riccati equation [8] governing the evolution of the poles of a second order LTV system. The objective was to identify the sets of initial conditions on the coefficients of the LTV system, that lead to divergence of the LTV poles to negative  $\infty$ . While there has been some partial work in this regard in [10], that phase plane analysis only considered the case when the frozen time roots of the LTV system are real. Analysis was performed under this research project under the different conditions of when the frozen time roots of the LTV system are wholly real, or wholly complex, or transition from real to complex at some time, and vice versa. Under these conditions (that cause the LTV poles to diverge), we then explore the use of an optimization-based approach that uses output measurements to compute the LTV poles. The use of output measurements to compute LTV poles would be necessary in practical situations (for example, while performing flight tests to detect the poles of a time-varying aircraft with uncertain parameters). The ensuing optimization based LTV poles were compared with the LTV poles generated from the Riccati equation.

## ANALYSIS

Consider a second order LTV system of the form:

$$d^2x/dt^2 + a_1(t)dx/dt + a_0(t)x(t) = 0 \quad (1)$$

which can be written using operator notation  $D = d/dt$ , as

$$(D^2 + a_1(t)D + a_0(t))x(t) = 0 \quad (2)$$

If there exist functions  $p_1(t)$  and  $p_2(t)$  such that one can write

$$(D^2 + a_1(t)D + a_0(t))x(t) = (D - p_1(t))\{(D - p_2(t))x(t)\} \quad (3)$$

and a (non commutative) polynomial multiplication  $\circ$  is designed such that

$$\{(D - p_1(t))\circ(D - p_2(t))\}x(t) = (D - p_1(t))\{(D - p_2(t))x(t)\} \quad (4)$$

Then, comparing (3) and (4), one can define

$D \circ p_2(t) = p_2(t)D + dp_2/dt(t)$ , and finally arrive at an equation for  $p_2$  as

$$p_2^2(t) + dp_2/dt + a_1(t)p_2(t) + a_0(t) = 0 \quad (5)$$

from which one can then determine  $p_1$  using

$$p_1(t) + p_2(t) = -a_1(t) \quad (6)$$

$(p_1(t), p_2(t))$  then form a pole set, and  $p_2(t)$  is called a right pole. Note that this is an ordered pole set, and even when  $p_1(t)$  and  $p_2(t)$  are complex, they need not, in general, be complex conjugate [4].

The mode associated with a right pole  $p_2(t)$  is defined as

$$\varphi_{p2}(t, 0) = \exp(\int_0^t p_2(\tau) d\tau) \quad (7)$$

and one can write

$$x(t) = C_1 \varphi_{p21}(t, 0) + C_2 \varphi_{p22}(t, 0) \quad (8)$$

where  $p_{21}$  and  $p_{22}$  represent two right poles determined by solving Eqn (5) from two different initial conditions (which are typically the two time invariant poles at  $t = 0$ , also referred to as the "frozen-time" roots of (1) at  $t=0$ ); and  $C_1$  and  $C_2$  are constants.

## PHASE PLANE ANALYSIS OF POLES OF A SECOND ORDER LTV SYSTEM:

In this section a phase plane analysis of (5) is performed, when used to compute the LTV poles of (1), under different conditions of the frozen time roots of (1). Note that the frozen-time roots of Eqn (1) are given by  $\{-a_1(t) \pm \sqrt{(a_1(t)^2 - 4a_0(t))}\}/2$ , for each t. These are also the same as the frozen-time eigenvalues of the matrix

$$\begin{matrix} 0 & 1 \\ -a_0(t) & -a_1(t) \end{matrix}$$

now consider different cases of the values of the frozen-time roots :

Case I :  $a_1(t)^2 - 4a_0(t) > 0$  for all t, i.e. the frozen-time roots are real for all time t.

In this case, one can write Eqn (5) as

$$dp_2/dt = -(p_2 + a_1(t)/2)^2 + (a_1(t)^2/4 - a_0(t)) \quad (9)$$

Note that the fact that the frozen time roots are real for  $t=0$ , and that these same roots are being used as initial conditions in the solution of Eqn (9) implies that  $p_{21}(t)$  and  $\varphi^1(t)$  obtained from Eqn (9) will be real for all time. One can therefore perform a phase-plane study on the  $(p_2, dp_2/dt)$  plane. On this plane, at each time t, Eqn (9) represents a parabola with vertex at  $(-a_1(t)/2, a_1(t)^2/4 - a_0(t))$  and pointing downward, as shown in Figure 48. On this figure, the black dots represent the frozen time roots, while the arrows indicate the direction of the  $(p_2, dp_2/dt)$  trajectory (determined from the sign of  $dp_2/dt$  close to the frozen time roots). From this figure, one can see that once the left branch of the trajectory enters the region  $dp_2/dt < 0$ , it will remain in the region  $dp_2/dt < 0$  for all future time. In other words, once the LTV pole originating at the left (negative) fixed point begins to decrease in value with time, it will continue to decrease for all future time. Since the y co-ordinate of the vertex of this parabola is always positive, therefore any subsequent changes in  $a_1(t)$  and/or  $a_0(t)$  (as long as they continue to satisfy  $a_1(t)^2 - 4a_0(t) > 0$ ) will not alter this behavior.

Now look at the conditions where the LTV system Eqn (1) will have trajectories that originate at the negative initial frozen time root, and continue to have  $dp_2/dt < 0$ . For this, look at the second derivative of  $p_2$  and evaluate it at  $t=0$ . Differentiating Eqn (5) with respect to time,

$$d^2p_2/dt^2 = -(2p_2 + a_1(t)) dp_2/dt - da_1/dt p_2 - da_0/dt \quad (10)$$

The above equation is now used to evaluate  $d^2p_2/dt^2(0)$  (keeping in mind that  $dp_2/dt(0)=0$ ), to get

$$d^2p_2/dt^2(0) = -da_1/dt(0) p_2(0) - da_0/dt(0) \quad (11)$$

Now if  $d^2 p_2 / dt^2(0) < 0$ , that means  $dp_2 / dt(\Delta t) < dp_2 / dt(0)$  (for positive  $\Delta t$ ), or in other words,  $dp_2 / dt(\Delta t) < 0$  (since  $dp_2 / dt(0)=0$ ). To summarize therefore, if the parameters  $a_1(0), da_1/dt(0), a_0(0), da_0/dt(0)$  in Eqn (1) are such that they satisfy

$$-da_1/dt(0) p_2(0) - da_0/dt(0) < 0, \text{ i.e.}$$

$$-da_1/dt(0) \{(-a_{1\{1\}}(0)-\sqrt{a_{1\{1\}}(0)^2-4a_0(0)})\}/\{2\} - da_0/dt(0) < 0 \quad (12)$$

then the LTV pole obtained from Eqn (5) and originating from the negative initial frozen time root, will go to negative  $\infty$ . On the other hand, if the parameters satisfy

$$-da_1/dt(0) \{(-a_{1\{1\}}(0)-\sqrt{a_{1\{1\}}(0)^2-4a_0(0)})\}/\{2\} - da_0/dt(0) > 0 \quad (13)$$

then the LTV pole obtained from Eqn (5) and originating from the negative initial frozen time root, will remain bounded. In the case when the inequality sign in (12) is replaced by an equality sign, one can derive corresponding conditions to determine whether the LTV pole is bounded or not, by looking at  $d^3 p_2 / dt^3(0)$ , and so on.

Now each of the above two behaviors with examples will be illustrated. Consider a system with  $a_1(t) = 3-t; a_0(t) = -0.1$ . It can be verified that these system parameters satisfy the condition (12). The response  $x(t)$  of Eqn (1) is shown in Figure 49, while the LTV poles computed from Eqn (5) are shown in Figure 50. It is clearly seen that within the time frame of  $t=[0,5]$  sec, one of the LTV poles grows unboundedly, while the other one remains bounded. Figure 51 shows why this happens, using the phase plane analysis described above. This figure shows the phase portraits at several time instants (as  $a_1(t)$  varies), along with the corresponding  $(p_2, dp_2/dt)$  trajectory obtained from the solution of Eqn (5).

On the other hand, consider the system  $a_1(t) = 3+t; a_0(t) = -0.1$ . It can be verified that these system parameters satisfy the condition Eqn (13). The LTV poles for this system are shown in Figure 52. It is seen that both the LTV poles  $p_{21}$  and  $p_{22}$  remain bounded. An understanding of why this is so, can be inferred from the phase portrait of Figure (53).

Case II :  $a_1(t)^2 - 4a_0(t) < 0$  for all  $t$ , i.e. the frozen-time roots are complex for all time  $t$ .

In this case,  $p_{21}(0)$  and  $p_{22}(0)$  are complex. Separating  $p_2$  into its real and imaginary parts, we can write  $p_2 = p_{2R} + jp_{2I}$ . We can then write out two ODEs from Eqn (5), corresponding to the real and imaginary parts of  $p_2$  as :

$$dp_{2R}/dt = -p_{2R}^2 + p_{2I}^2 - a_1(t) p_{2R} - a_0(t) \quad (14)$$

$$dp_{2I}/dt = -2p_{2R}p_{2I} - a_1(t) p_{2I} \quad (15)$$

Eqn (14) represents a hyperbolic paraboloid in the three-dimensional  $(p_{2R}, p_{2I}, dp_{2R}/dt)$  space. This surface is as shown in Figure 54. In general, cross-sections taken parallel to two of the three co-ordinate planes of a hyperbolic paraboloid are parabolas, while that taken parallel to the third co-ordinate plane is a hyperbola. Similarly, Eqn (15) represents a surface that is qualitatively depicted in Figure 55. The solutions of Eqns (14) and (15) will represent curves that lie on each of these two surfaces. We can then perform an analysis by qualitatively plotting

the trajectories on a  $(p_{2R}, p_{2I})$ s plane. Considering for a moment  $dp_{2R}/dt = 0$  in Eqn (14), then write Eqn (14) as

$$p_{2I}^2 - (p_{2R} + a_1(t)/2)^2 = a_0(t) - a_1(t)^2/4 \quad (16)$$

Eqn (16) then represents a hyperbola on the  $(p_{2R}, p_{2I})$  plane; whose two vertices at each time  $t$  are at  $(-a_1(t)/2, \pm a_0(t) - a_1(t)^2/4)$ . These vertices correspond to the frozen time roots of Eqn (1). Points lying "inside" this hyperbola correspond to  $dp_{2R}/dt < 0$ , while points lying "outside" the hyperbola correspond to  $dp_{2R}/dt > 0$ . Therefore trajectories that lie inside the hyperbola have a horizontal component to the right, while those that lie outside the hyperbola have a horizontal component to the left. One can perform a similar analysis on Eqn (6) to determine that trajectories that satisfy either  $p_{2I} > 0; p_{2R} < -a_1(t)/2$  or  $p_{2I} < 0; p_{2R} > -a_1(t)/2$  have a vertical upward component (in the direction of increasing  $p_{2I}$ ), while trajectories that lie in either  $p_{2I} > 0; p_{2R} > -a_1(t)/2$  or  $p_{2I} < 0; p_{2R} < -a_1(t)/2$  have a vertical downward component. In this way, after appropriately partitioning the  $(p_{2R}, p_{2I})$  plane, one can determine the direction of the trajectories in each such partition. These trajectories are qualitatively depicted in Figure 56. The black dots on this figure represent the frozen time roots. From this figure, we can infer that as long as the complex part of the LTV poles is non-zero, the LTV poles remain bounded. However, the instant the complex part of the LTV poles drops to zero, it then remains zero for all future time (this can also be seen by substituting  $p_{2I}=0$  in Eqn (15) and noticing that it leads to making  $dp_{2I}/dt=0$ ), and the real part of the LTV poles subsequently goes to negative  $\infty$ .

Now the case when the frozen time roots change from real to complex, and vice-versa with an example wherein  $a_1(t) = 3-t$ ;  $a_0(t) = 0.2$  for  $t=[0,5]$  will be illustrated. In this case, the frozen time roots are initially real for  $t=[0,2.1]$  sec, then become complex conjugate for  $t = [2.1, 3.9]$  sec and finally become real again. The frozen time roots are depicted in Figure 57 and the simulation response is depicted in Figure 58.

The LTV poles for this system are shown in Figure 59. In this case, we see that both the LTV poles go to negative  $\infty$ . The reason for this can be inferred from the analyses discussed above.  $p_{2I}$  goes to negative  $\infty$  while the frozen time LTI poles are still real, for the reasons enumerated in Case I above. During this time,  $p_{22}$  remains bounded (as is seen in Figure 60). However, the instant the frozen time roots become complex,  $p_{22}$  finds itself on the real axis of the  $(p_{2R}, p_{2I})$  plane, and from the analysis of Case II (and Figure 57) one can see why it goes to negative  $\infty$ . Subsequently, even though both the frozen time roots become real again,  $p_{22}$  cannot be recovered again to have a finite value.

#### **DETERMINATION OF LTV POLES FROM OUTPUT MEASUREMENTS THROUGH AN OPTIMIZATION BASED APPROACH:**

In this section, the determination of the poles of a LTV system from output measurements will be investigated. In particular, those cases when the LTV poles are determined from the solution of Eqn (5) go to  $\infty$ , and are consequently unable to provide an accurate representation of the modes of the system. First consider the case when only a single measurement source (of  $x(t)$ ) is available, from which the LTV poles need to be determined. For a second order LTV system (of the form in Eqn (1)), one can write  $x(t)$  in terms of its right poles  $p_{21}(t)$  and  $p_{22}(t)$  as :

$$x(t) = C_1 \exp(\int_0^t p_{21}(t) dt) + C_2 \exp(\int_0^t p_{22}(t) dt) \quad (17)$$

where  $C_1$  and  $C_2$  are constants that depend on the initial conditions and the values of the LTV poles at  $t=0$  (which are the same as the frozen-time roots of Eqn (1) at  $t=0$ ).

Discretize time with equally spaced intervals  $\Delta t$  as  $[t_1, t_2, \dots, t_n]$  and then write out the above as an optimization problem involving nonlinear least squares minimization as follows :

Find  $p_{21}(t_1, t_2, \dots, t_n), p_{22}(t_1, t_2, \dots, t_n)$  such that

$$\begin{aligned} p_{21}(t_1, t_2, \dots, t_n), p_{22}(t_1, t_2, \dots, t_n) &= \arg \min \sum_{i=2}^{i=n} [x(t_i) \\ &- C_1 e^{\{(p_{21}(0) + (p_{21}(t_1) + \dots + p_{21}(t_{i-1})) / 2 + p_{21}(t_i)) \Delta t\}} \\ &- C_2 e^{\{(p_{22}(0) + (p_{22}(t_1) + \dots + p_{22}(t_{i-1})) / 2 + p_{22}(t_i)) \Delta t\}}]^2 \end{aligned} \quad (18)$$

where the trapezoidal approximation for the integral in Eqn (17) is used.

Figure 61 then shows the LTV poles computed by solving Eqn (17) for the case when  $a_1(t)=3-t; a_0(t)=0.2$ . It is seen that both the LTV poles remain bounded. Figure 62 shows the ensuing LTV modes, along with a comparison of the modes obtained from the solution of Eqn (5). It can be clearly seen that these modes are able to pick up the unstable segment of the response shown in Figure 58, while the same could not be detected by the solution of Eqn (5). Furthermore, even though the frozen time roots in this case change from real to complex and back to real, Eqn (18) generates only real LTV poles throughout owing to the fact that  $C_1$  and  $C_2$  are real (which in turn is because the initial values of the frozen time roots are real). Figure 62 shows a comparison of the ensuing modes from the different approaches. While it is seen that the modes corresponding to the solution of Eqn (2) cannot demonstrate the unstable segment of the response (which occurs after  $p_{21}$  has gone to negative  $\infty$ ), the modes determined from the optimization approach are able to demonstrate the same.

Figure 63 then shows the LTV poles computed by solving Eqn (18) for the case when  $a_1(t)=3-t; a_0(t)=-0.1$ . It is seen that LTV pole  $p_{21}$  remain bounded. However, a comparison of  $p_{22}$  obtained from the solution of Eqn (18) with that obtained from the solution of Eqn (5) shows some mismatch of the two poles, particularly in the region surrounding  $t=3$  sec as well as close to  $t=5$  sec. A modified optimization function, that now involves the use of two measurement sources (i.e.  $x(t)$  as well as  $dx/dt(t)$ , is used) is therefore explored. Since,

$$dx/dt(t) = C_1 p_{21}(t) \exp(\int_0^t p_{21}(t) dt) + C_2 p_{22}(t) \exp(\int_0^t p_{22}(t) dt) \quad (19)$$

therefore, the optimization problem takes the form :

Find  $p_{21}(t_1, t_2, \dots, t_n), p_{22}(t_1, t_2, \dots, t_n)$  such that

$$p_{21}(t_1, t_2, \dots, t_n), p_{22}(t_1, t_2, \dots, t_n) =$$

$$\arg \{ \min \} \sum_{i=2}^{i=n} [x(t_i) - C_1 \exp\{(p_{21}(0) + (p_{21}(t_1) + \dots + p_{21}(t_{i-1})) / 2 + p_{21}(t_i)) \Delta t\}]^2$$

- $- C_2 \exp\{(p_{22}(0) + (p_{22}(t_1) + \dots + p_{22}(t_{i-1}))/2 + p_{22}(t_i)) \Delta t\}^2 + [dx/dt(t_i) - C_1 p_{21}(t_i) \exp\{(p_{21}(0) + (p_{21}(t_1) + \dots + p_{21}(t_{i-1}))/2 + p_{21}(t_i)) \Delta t\}]^2$
- $- C_2 p_{22}(t_i) \exp\{(p_{22}(0) + p_{22}(t_1) + \dots + p_{22}(t_{i-1}))/2 + p_{22}(t_i)) \Delta t\}^2 \quad (20)$

With this objective function, it is now seen that the LTV pole  $p_{22}$  obtained is much closer to that obtained from the solution of Eqn (5). This is evident from Figure 63. It turns out that this new objective function does not change  $p_{21}$  at all, from the previous optimization function. This  $p_{21}$  however is bounded, in contrast to the unbounded  $p_{21}$  obtained from the solution of Eqn (5).

### CONCLUSIONS:

A detailed phase-plane analysis on the differential Riccati equation governing the evolution of the poles of a second order LTV system was performed. The objective was to identify the sets of initial conditions on the coefficients of the LTV system, that lead to the LTV poles diverging to negative  $\infty$ . This was done under the different conditions of when the frozen time roots of the LTV system are wholly real, or wholly complex, or change from real to complex at some time, and vice versa. Thus, for example, when the frozen time roots change from real to complex and then back to real, both the LTV poles diverge to negative  $\infty$ . Under these conditions, the use of an optimization based approach that uses output measurements to compute the LTV poles was explored. The ensuing optimization based LTV poles with the LTV poles generated from the Riccati equation were compared. It is observed that both the optimization based LTV poles remain bounded; with one of these poles comparing reasonably well with the stable solution of the Riccati equation.

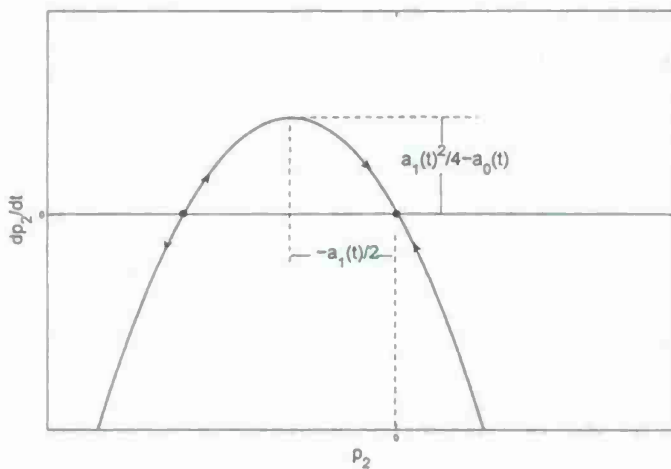


Fig 48. Phase plane trajectory of  $(p_2, dp_2/dt)$  when frozen time roots are real

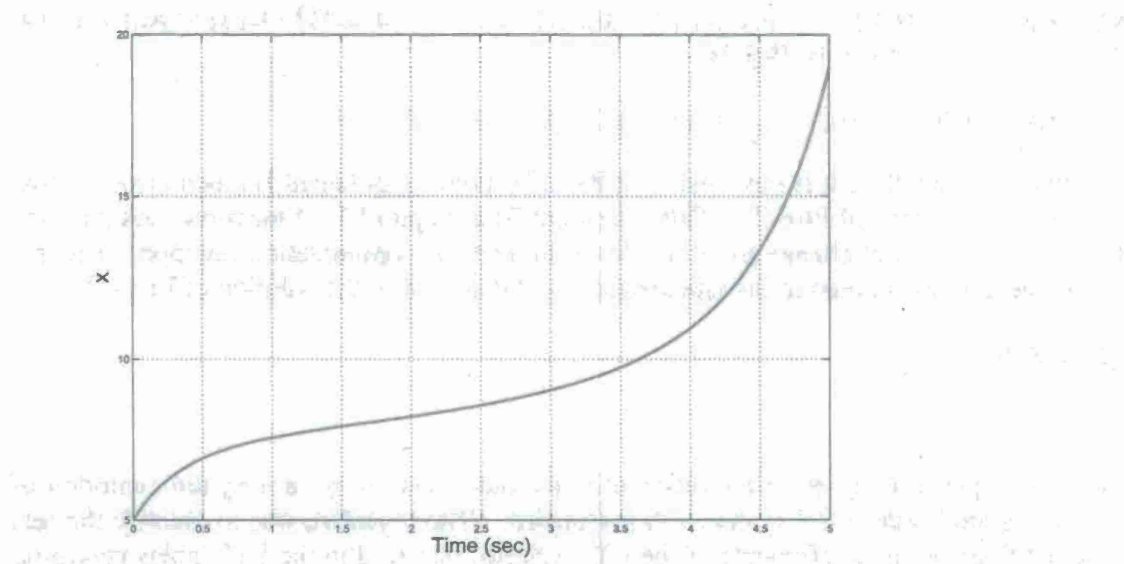


Figure 49. Simulation response for  $a_1(t)=3-t; a_0(t)=-0.1$

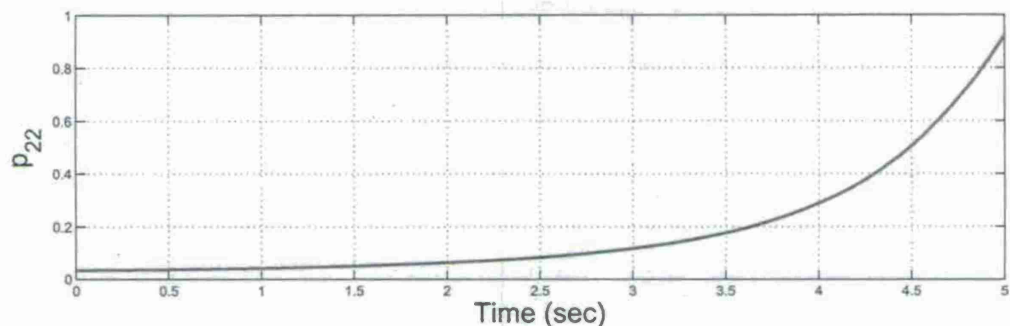
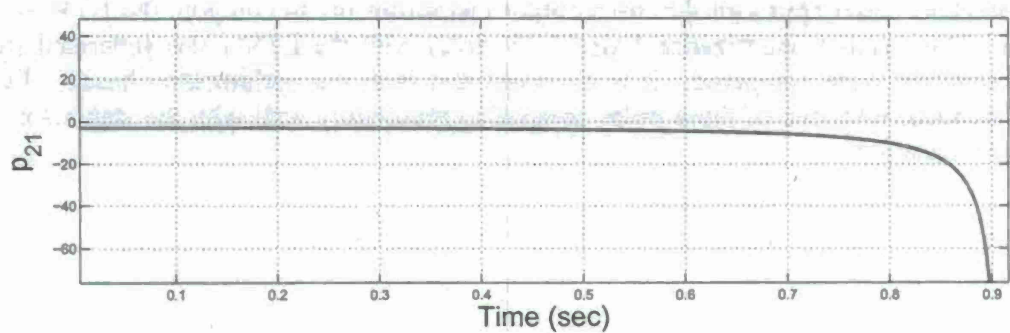


Figure 50. LTV poles computed for  $a_1(t)=3-t; a_0(t)=-0.1$  using Eqn (5)

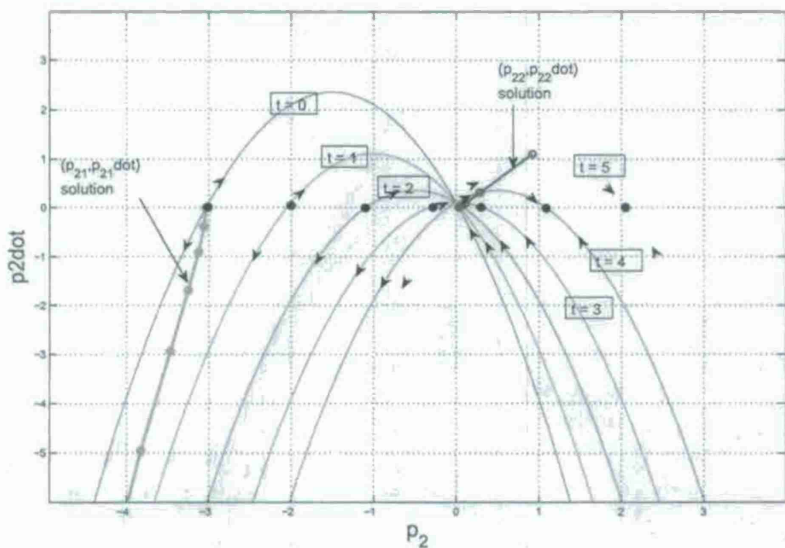


Figure 51. Phase plane trajectory of  $(p_2, dp_2/dt)$  at several time instants  $t=0,1,2,3,4,5$  sec for  
 $a_1(t)=3-t; a_0(t)=-0.1$

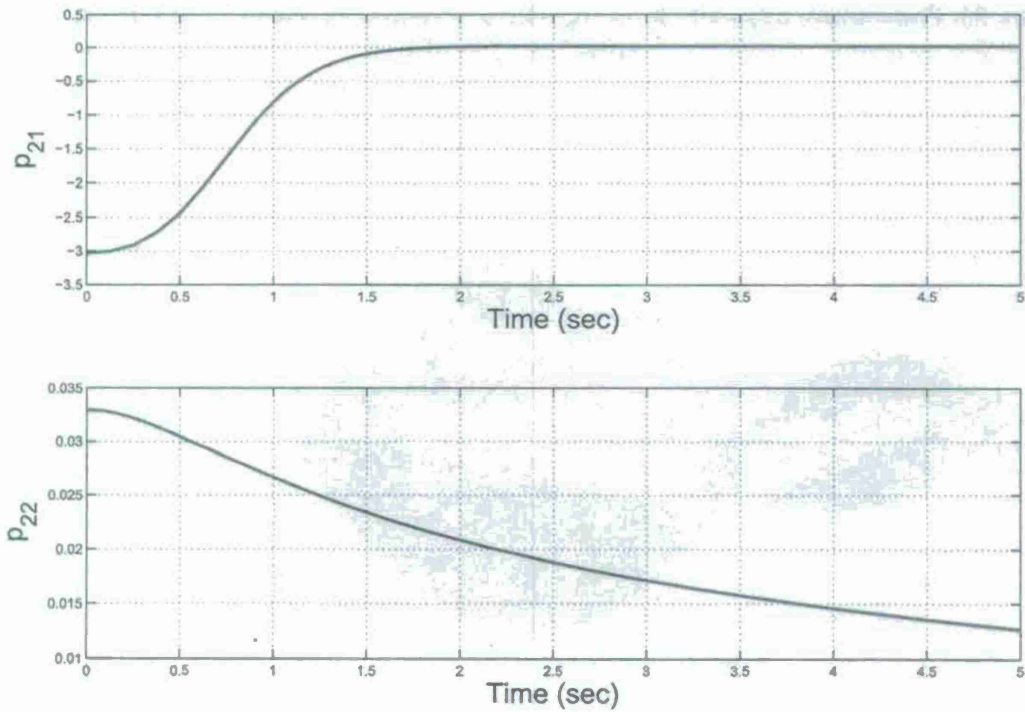


Figure 52. LTV poles computed for  $a_1(t)=3+t; a_0(t)=-0.1$  using Eqn (5)

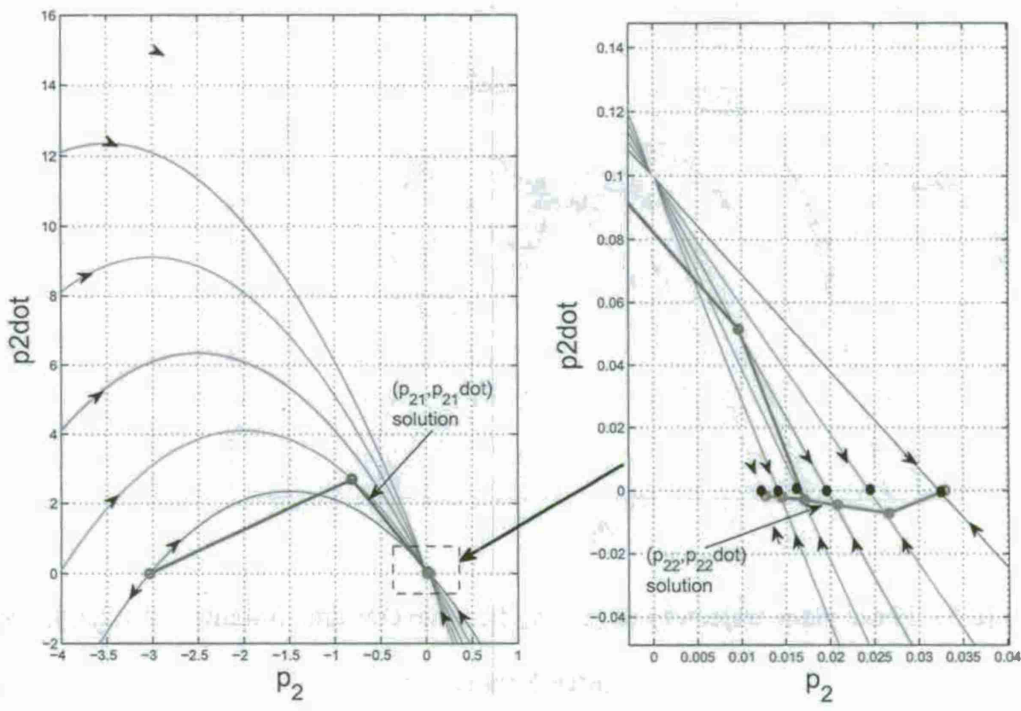


Figure 53. Phase plane trajectory of  $(p_2, dp_2/dt)$  at several time instants  $t=0, 1, 2, 3, 4, 5$  sec for  
 $a_1(t)=3+t; a_0(t)=-0.1$

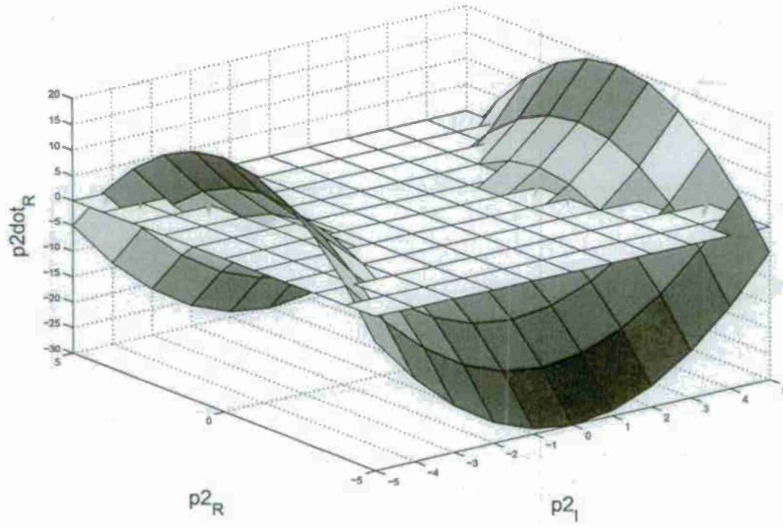


Fig 54.  $(p_{2R}, p_{2I}, dp_{2R}/dt)$  phase space

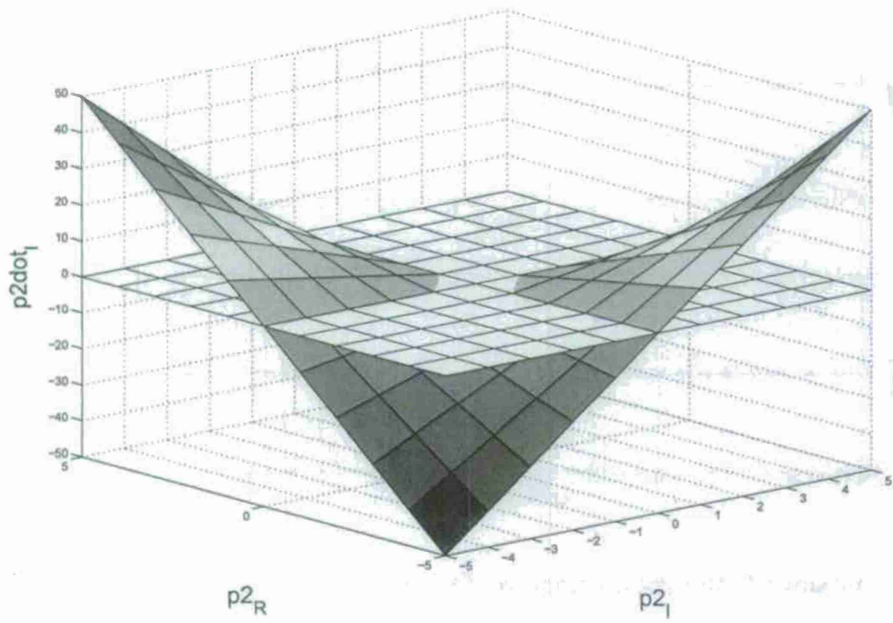


Figure 55.  $(p_{2R}, p_{2I}, dp_{2I}/dt)$  phase space

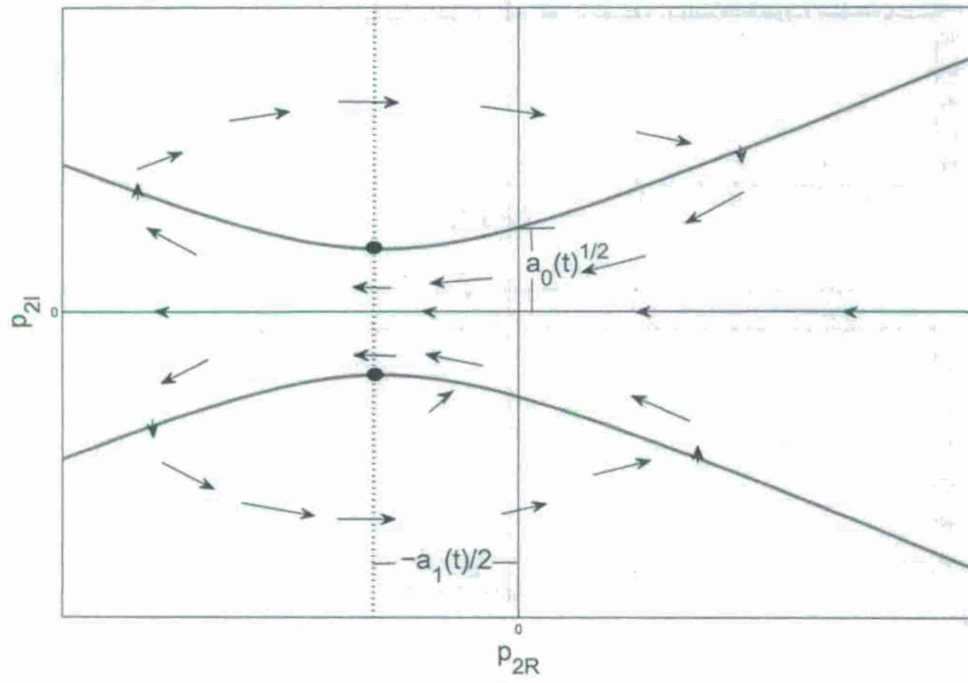


Figure 56. Phase plane trajectory of  $(p_{2R}, p_{2I})$  when frozen time roots are complex

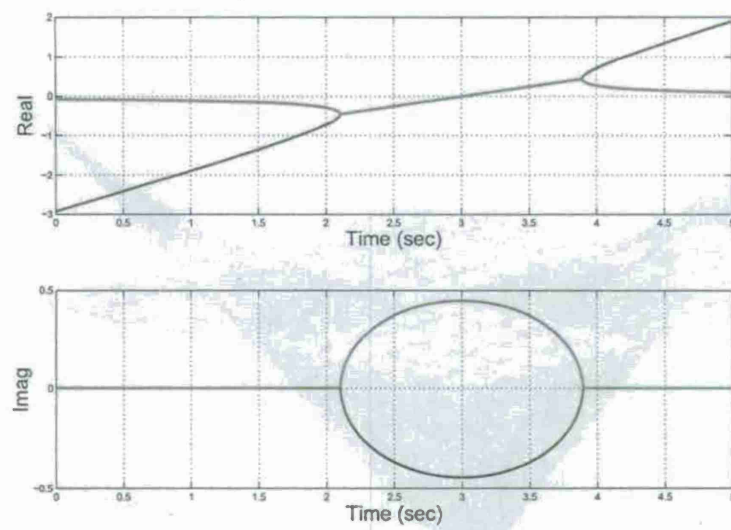


Figure 57. Simulation response for  $a_1(t)=3-t; a_0(t)=0.2$

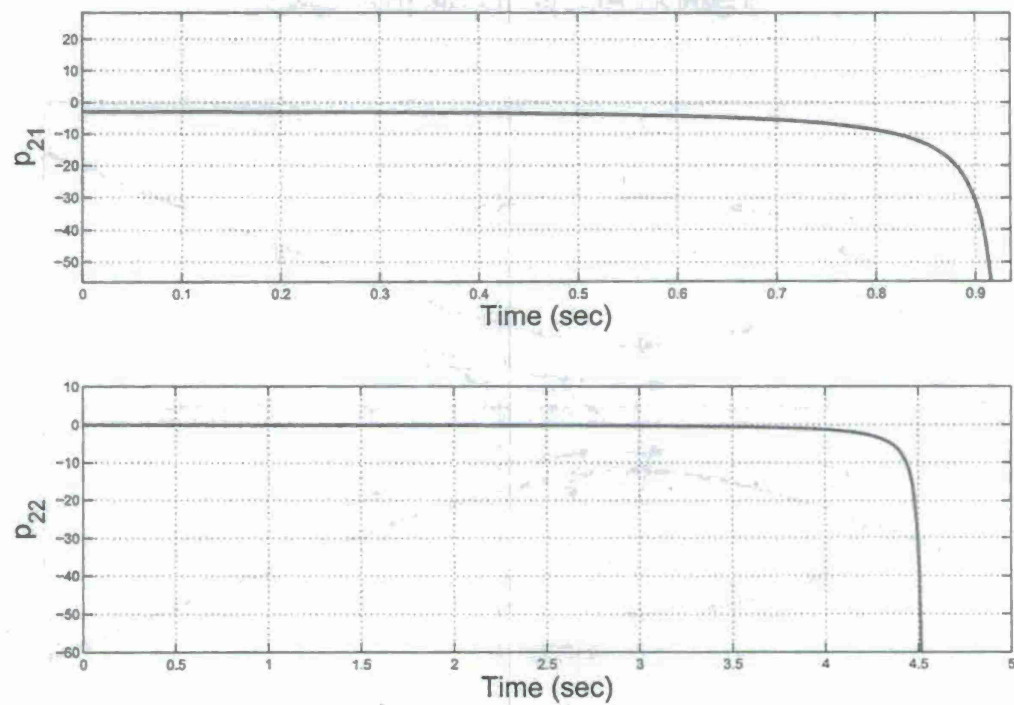


Figure 58. LTV poles computed for  $a_1(t)=3-t; a_0(t)=0.2$  using Eqn (5)

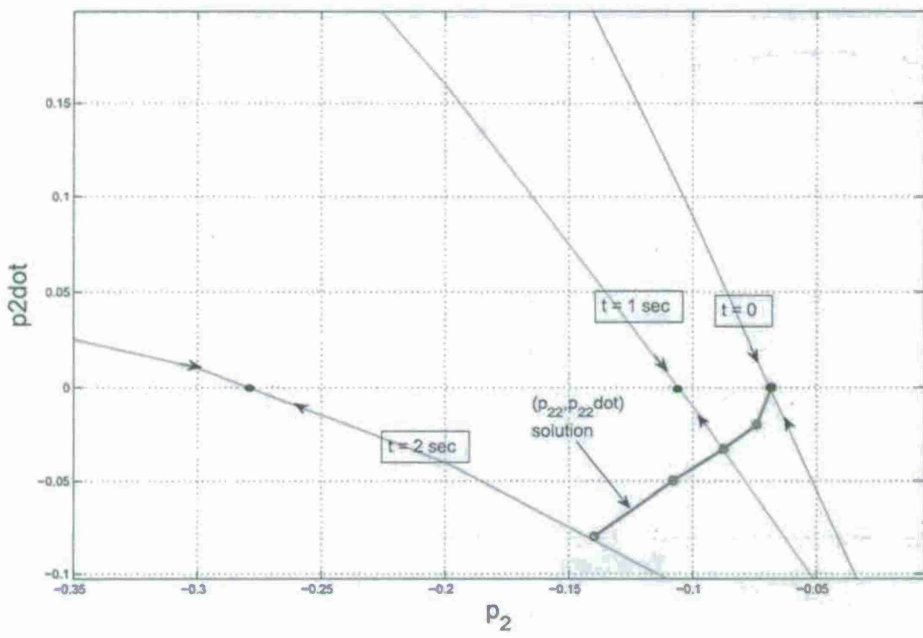


Figure 59. Phase plane trajectory of  $(p_2, dp_2/dt)$  at  $t=0, 1, 2$  sec for  $a_1(t)=3-t; a_0(t)=0.2$

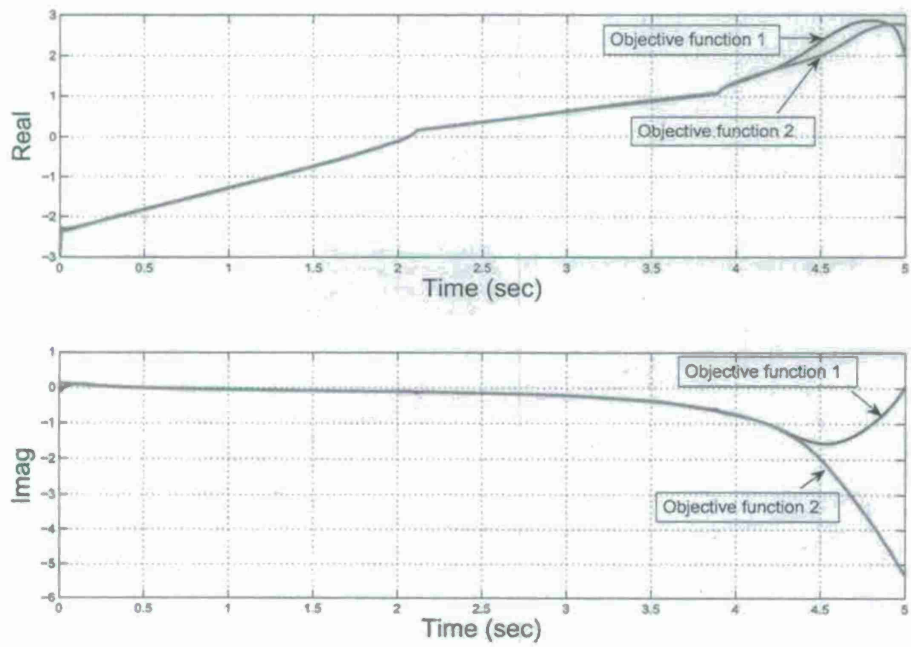


Figure 60. LTV poles computed for  $a_1(t)=3-t; a_0(t)=0.2$  using Eqns (18), (20)

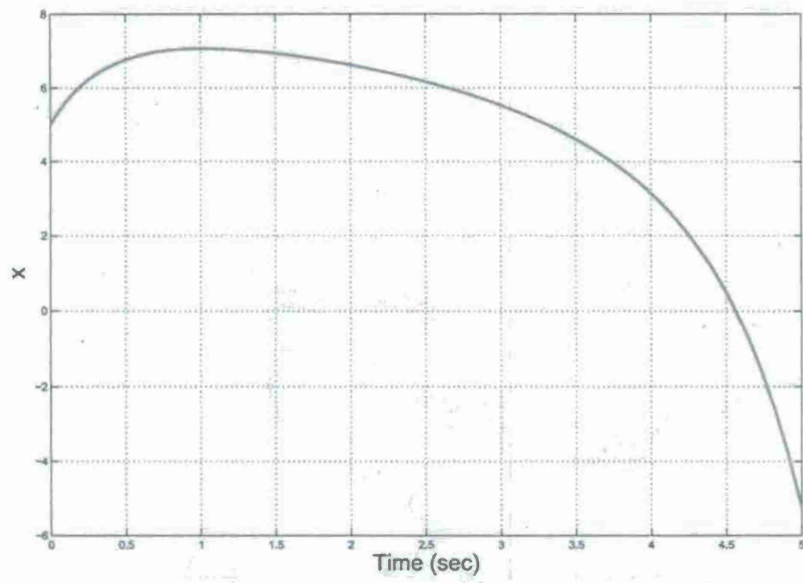


Figure 61. Simulation response for  $a_1(t)=3-t; a_0(t)=0.2$

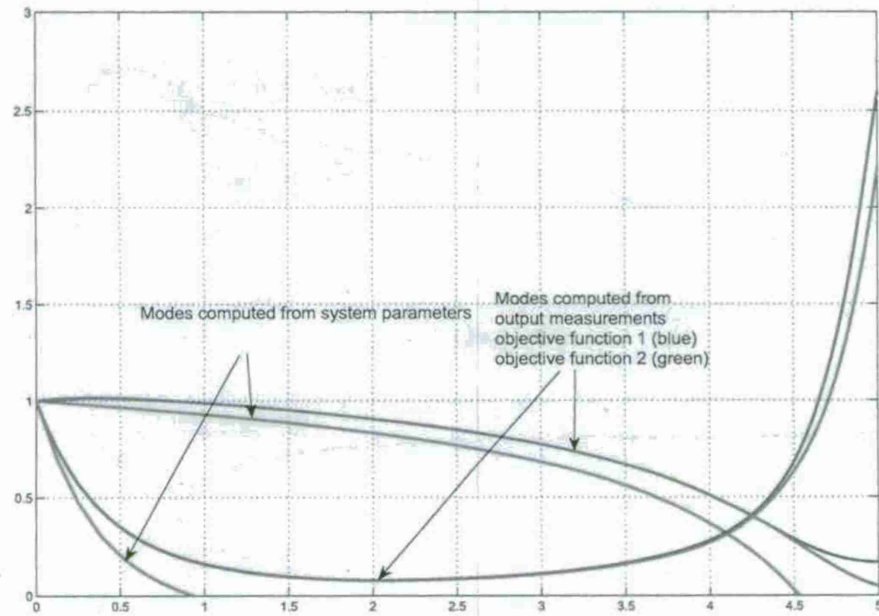


Figure 62. Comparison of LTV modes computed for  $a_1(t)=3-t; a_0(t)=0.2$  using system parameters (5) and sensor measurements (Eqns (18), (20))

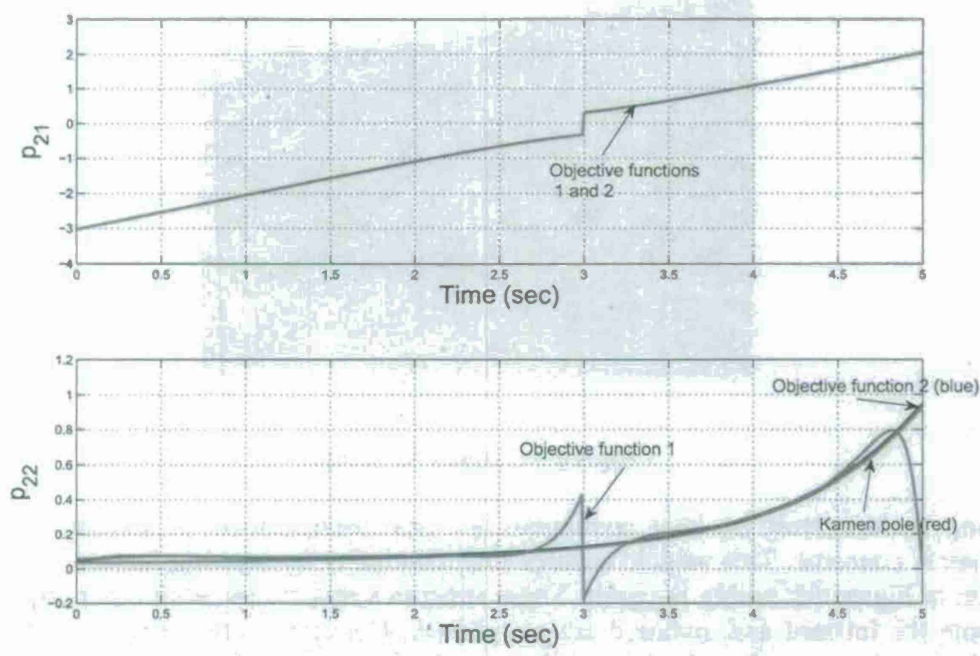


Fig 63. Comparison of LTV poles computed for  $a_1(t)=3-t$ ;  $a_0(t)=-0.1$  using system parameters (Eqn (5)) and sensor measurements (Eqns (18), (20))

## MORPHING WING MAV STUDY

### Vehicle

A vehicle which features the independent multi-joint capability was designed by retrofitting an existing aircraft. The basic construction uses skeletal members of a prepregnated, bi-directional carbon fiber weave along with rip-stop nylon. The fuselage and wings are entirely constructed of the weave while the tail features carbon spars covered with nylon. The resulting structure is durable but lightweight.

The wings are actually separate sections that are connected to the fuselage and each other through a system of spars and joints. These joints, as shown in Figure 64, are representative of a shoulder and elbow which serve to vary the sweep of inboard and outboard. The range of motion admitted by these joints is approximately  $\pm 30$  deg.

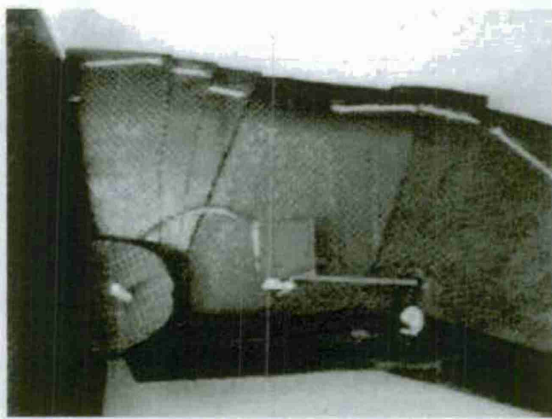


Figure 64. Joints on Wing

The wing surface must be kept continuous for any configuration of sweeping because of aerodynamic concerns. This vehicle ensures such continuity by layering feather-like structures, as shown in Figure 65, within the joint. These structures retract onto each other under the wing when both the inboard and outboard are swept back. Conversely, they create a fan-like cover across the ensuing gap when the inboard is swept back and the outboard is swept forward. The contraction and expansion of the surface area created by these structures is smoothly maintained by a tract system implemented on the outer regions of each member.

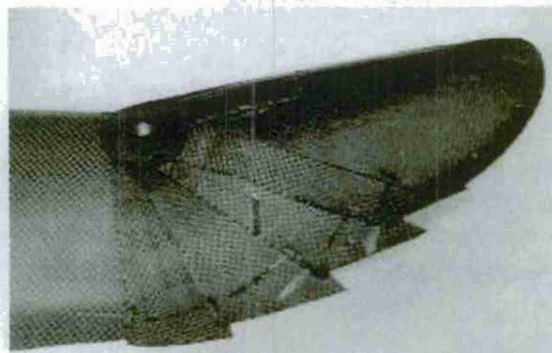


Figure 65. Feather-Like Elements

Spars, formed from hollow shafts of carbon fiber, are placed along the leading edge of each wing. These spars act as both a rigid source to maintain the leading-edge curvature and a connection of each independent wing joint. The inboard spar is translated horizontally by a servo-driven linear actuator located inside the fuselage. The inboard spar is then connected to the inboard wing section at the shoulder joint located on the outside of the fuselage. The inboard spar then connects at the elbow joint to outboard spar at roughly the quarter span point. The outboard wing region is activated independently of the inboard region by means of a servo

attached at the elbow.

Overall, this vehicle is able to achieve a wide range of sweep orientations. Some representative configurations are shown in Fig. 66 to demonstrate the range.

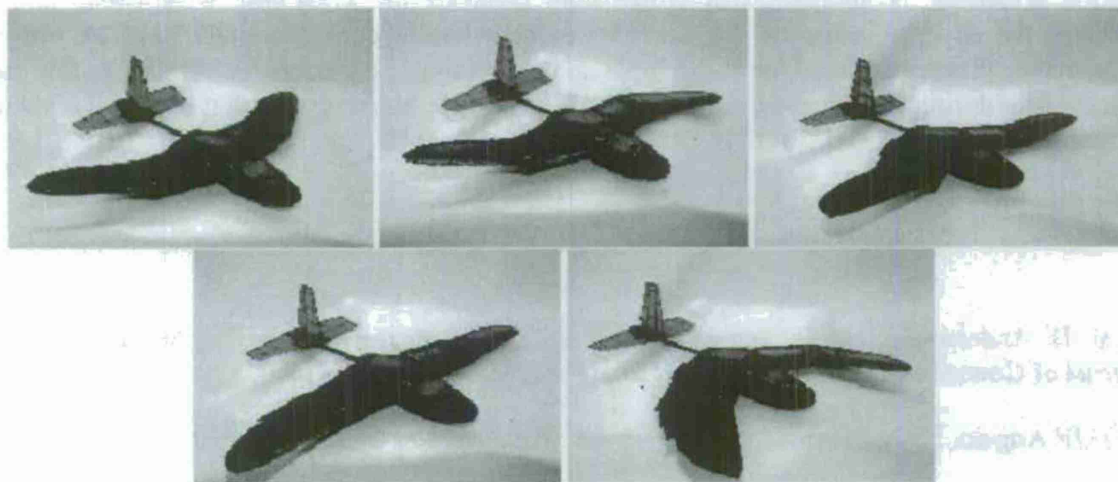


Figure 66. Sweep Configurations

### Modeling

A set of plant models were generated to represent the flight dynamics at each configuration. Essentially, the forces and moments affecting the vehicle are computed using an assumption of steady-state conditions. The resulting models do not properly relate the unsteady aerodynamics but will include the dominant steady-state aerodynamics. The time-varying inertias are then introduced to account for the morphing.

Also, the vehicle is constrained in this example to simplify the configuration space. The physical vehicle has 4 degrees-of-freedom in that each inboard and outboard and sweep independently on the left and right sides; however, this example constrains the left and right wings to symmetric sweep with the outboard having twice as much sweep as the inboard. This constraint limits the system to a single degree-of-freedom which is appropriate for the longitudinal nature of the altitude change associated with the mission.

The flight dynamics for each configuration are trimmed for straight and level flight. Actually, the thrust is held constant for each of these configurations to note the propulsion is not affected by the morphing. Such an approach is particularly useful for relating models that may be trimmed at various airspeeds. In this case, the thrust and drag were held constant so the trim routine found the correct airspeed.

## Simulations

Simulations were conducted for fast and slow varying wing sweeping conditions in various mission scenarios. A simulation of closed-loop behavior for a variable wing-sweep aircraft indicates the adverse influence that such transient behavior can potentially have on mission performance if not accounted for in the flight control design of the micro air vehicle. In this case, the coupling during the transient response resulted in a lateral translation that caused the vehicle to miss its target.

## REFERENCES:

- [5] B. D. Anderson, "Internal and External Stability of Linear Time-Varying Systems," SIAM Journal of Control and Optimization, Vol 20, No. 3, May 1982, pp. 408-413.
- [6] H.D' Angelo, Linear Time Varying Systems : Analysis and Synthesis, 1970.
- [7] R.T. O'Brien, Jr. and P.A. Iglesias, "On the Poles and Zeros of Linear, Time-Varying Systems," IEEE Transactions on Circuits and Systems-I:Fundamental Theory and Applications, Vol.48, No.5, May 2001, pp. 565-577.
- [8] E.W. Kamen, "The Poles and Zeros of a Linear Time Varying System," Linear Algebra and its Applications, 1988, pp.~263-289.
- [9] H. K. Khalil, "Nonlinear systems," 2002.
- [10] P. van der Kloet and F.L Neerhoff, "Some remarks on modal solutions for second and third order time-varying systems," Proc. ISSSE, Linz, Austria, August 10-13, 2004.
- [11] J.J. Zhu, "A Unified Spectral Theory for Linear Time-Varying Systems - Progress and Challenges," Proc. Of the 34th IEEE Conference on Decision and Control, 1995, pp. 2540-2546.
- [12] J.J. Zhu, "PD-Spectral Theory for Multivariable Linear Time-Varying Systems," Proc. IEEE Conference Decision and Control, 1997, pp. 3908-3913.

## Task 5: Computational Aerodynamics of Flexible and Flapping Wing for MAV

### MILESTONES/STATUS:

#### First 9 Months/Status)

- Assess computational and experimental data regarding flexible, morphing wing aerodynamics (lift, drag, detailed flow field). (Completed)
- Initiate flexible, Morphing wing simulations. (completed fro flexible and flapping wings)
- Document and evaluate higher order numerical and modeling treatments, including numerical dispersion/dissipation, grid movement, and transition-turbulence model coupling for morphing wings. (Completed for flapping wings)

Under the leadership of Dr. Wei Shyy from the University of Michigan (UM) and Dr. Jian Tang post doc from (UM) significant progress was made in computational fluid-structure interaction of a deformable flapping wing for micro air vehicle applications. Motivated by micro air vehicle applications, a fluid-structure coupling procedure was developed between a Navier-Stokes solver and a three-dimensional FEM beam solver ( see Figure 67). Research was conducted into fluid and flexible structural Wing interactions with selected results highlighting some of implications presented in this progress report. The fluid model includes laminar, the  $k-\varepsilon$  turbulence closure, and a filter-based  $k-\varepsilon$  closure. The structural model is based on an asymptotic approximation to the equations of elasticity. Using the slenderness as the small parameter, the equations are decomposed into two independent variational problems, corresponding to (i) cross-sectional, small-deformation and (ii) longitudinal, large deformation analyses. A model example problem corresponding to a NACA0012 wing of aspect ratio 3 in pure heave motion is presented and the results compared

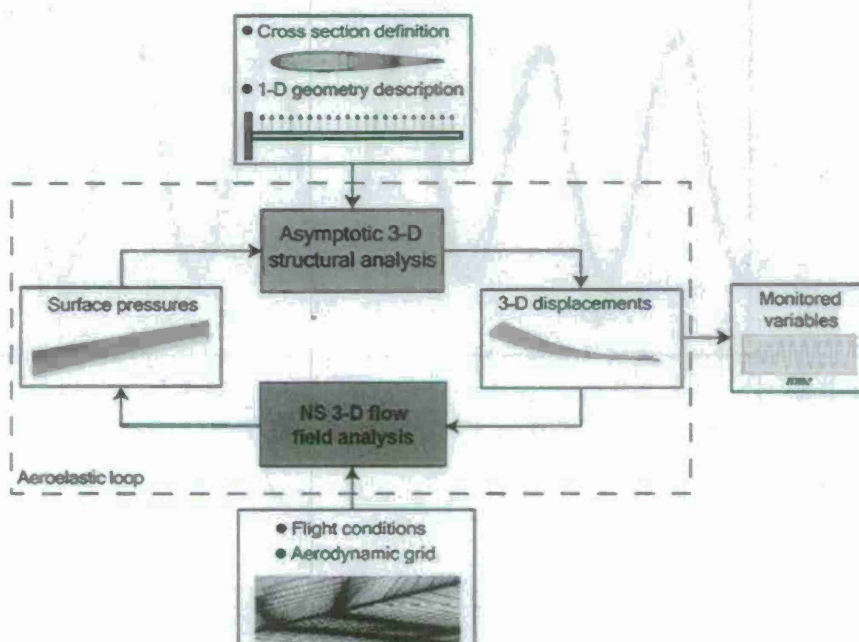
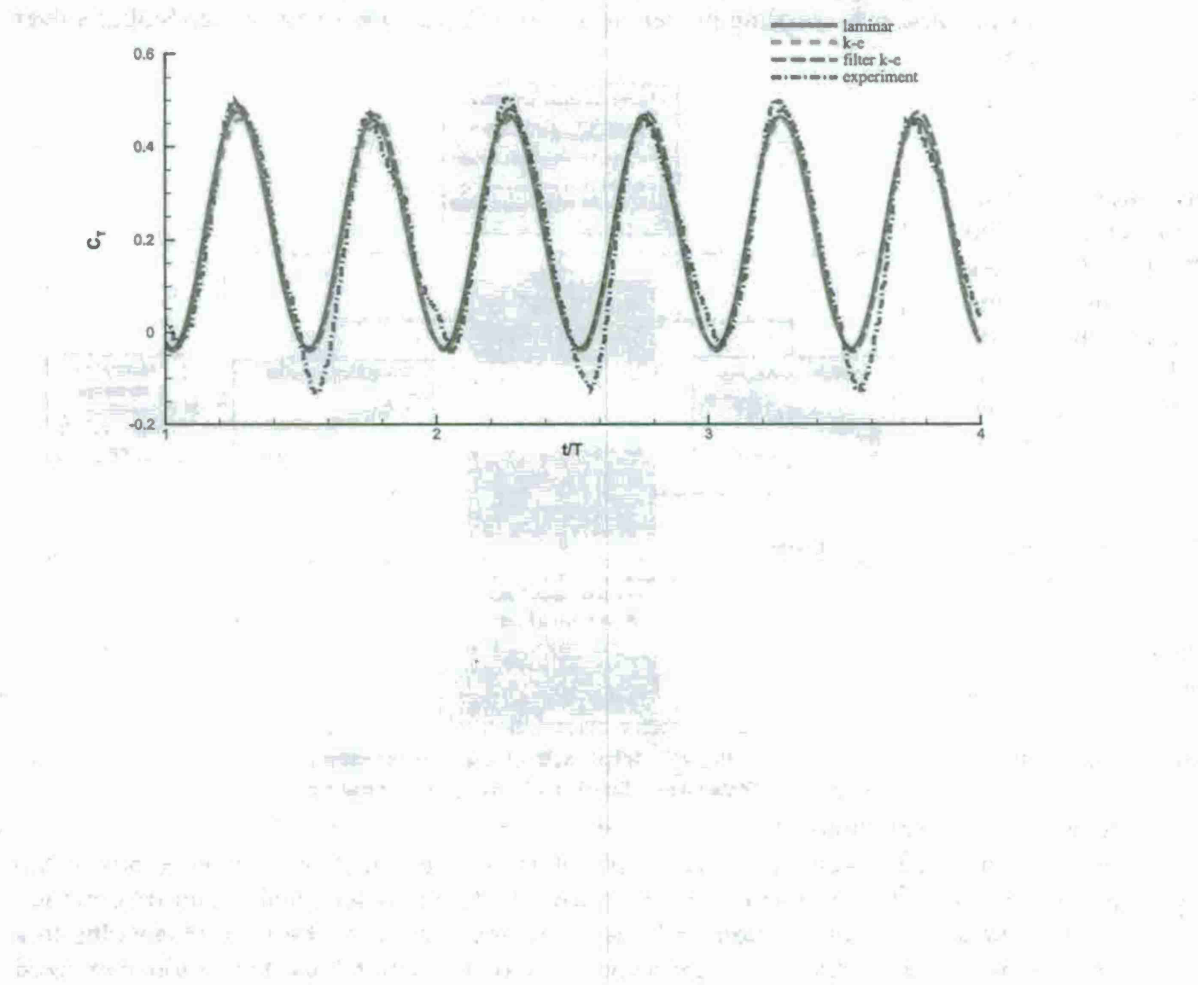


Fig 67: Schematic of the computational framework for flexible wing aerodynamics

against available experiment data (experimental results of Heathcote et al<sup>13</sup>). Quantitative comparisons with experiment are done for the rigid wing and the implications of wing flexibility on aerodynamics are presented in a qualitative sense. It was observed that phase lag of the wing tip displacement relative to the flapping motion becomes more pronounced as the fluid density increases.

## SELECTED RIGID WING RESULTS

Figure 68 includes the thrust coefficient results of three different computational cases compared with the experiment results. It may be observed that computational results have a decent agreement with those of experiment. It may also be observed that the inclusion of turbulent models did not have a significant effect on the response. The experimental data shows asymmetric thrust in the two strokes of each cycle, while the computational results show no distinguished difference between the two strokes. Compared to the experimental data, the computational results agree with the experimental data very well at the small force peaks, if the asymmetric difference is neglected.



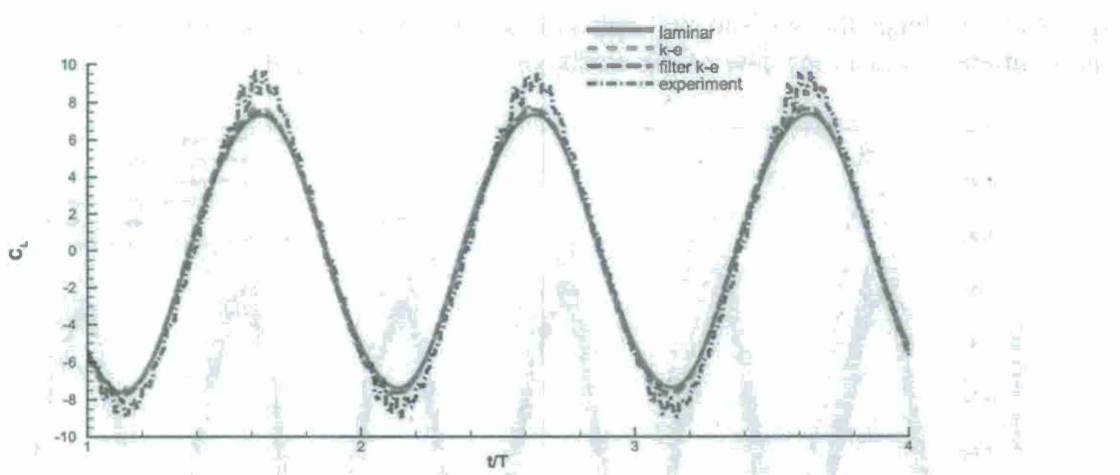


**Fig 68:** Thrust (upper) and Lift (lower) coefficients of experimental and computational results of rigid wing.  $k-\varepsilon$  model,  $k-\varepsilon$  with filter model and laminar flow are employed in the computation. ( $Re=30,000$ ,  $h_r=0.175$ ,  $k=1.82$ )

#### SELECTED FLEXIBLE WING RESULTS

Fig. 69 includes the thrust coefficient response of the flexible wing at 3 different flow densities (air density, 10xair density, and 416xair density) compared to the computational and experimentally determined responses of the rigid wing at the same Reynolds number. Once again, the effect of induced phase lag is seen here. Incremental changes to the thrust coefficient are clearly seen with increasing flow density. Also, it may be noted that spanwise flexibility has proven to be beneficial to the thrust coefficient just as seen in the experiment.

Fig. 69 also includes the experimental response of the flexible wing for the heavier fluid case. Similar inferences as in the case of the displacement response may be drawn even in this case.

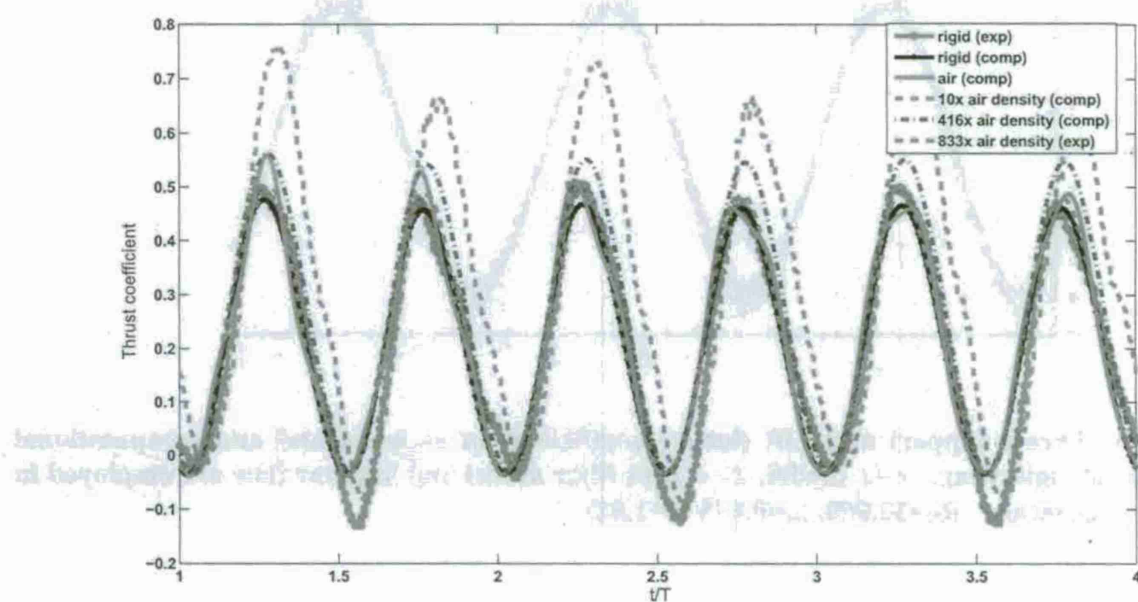


**Fig 69: Thrust coefficient response of the flexible wing at three different flow densities**

#### REFERENCES:

13. Heathcote, S., Z. Wang., and Gursul, I, "Effect of Spanwise Flexibility on Flapping Wing Propulsion", AIAA Paper 2006-2870, Jan. 2005..

#### PERSONNEL SUPPORTED DURING DURATION OF GRANT

Dr. Rogacki	Professor, UF-REEF
Dr. Ukeiley	Assistant Professor, UF-REEF
Dr. Albertani	Research Engineer, UF-REEF
Dr. Prazenica	Visiting Professor, UF-REEF
Dr. Chakravarthy	Research Engineer, UF-REEF
Dr. Carroll	Associate Professor, University of Florida
Dr. Ifju	Associate Professor, University of Florida
Dr. Lind	Assistant Professor, University of Florida

Dr. Dixon	Assistant Professor, University of Florida
Dr. Shyy	Professor, University of Michigan
Dr. Hubner	Assistant Professor, University of Alabama
Dr. Gans	Post Doc, UF-REEF
Dr. Tang	Post Doc, University of Michigan
3 Graduate students	University of Florida, UF-REEF, and University of Alabama

## PUBLICATIONS

### **Journal Articles/to appear**

1. Lian, Y. and Shyy, W., "Laminar-Turbulent Transition of a Low Reynolds Number Rigid or Flexible Airfoil," *AIAA Journal*, Vol. 45, (2007), pp. 1501-1513.
2. Albertani, R, B Stanford, JP Hubner, and PG Ifju (2007) "Aerodynamic Characterization and Deformation Measurement of a Flexible Wing Micro Air Vehicle," *Experimental Mechanics*, 47(4), DOI: 10.1007/s11340-006-9025-5.
3. B. Stanford, M. Abulrahim, R. Lind and P. Ifju, "Investigation of Membrane Actuation for Roll Control of a Micro Air Vehicle, " *Journal of Aircraft*, Vol. 44, No. 3, May-June 2007, pp. 741-749.
4. Albertani, R., Stanford, B., Hubner, J. P., and Ifju, P., "Aerodynamic Characterization and Deformation Measurements of a Flexible Wing Micro Air Vehicle," *SEM Journal*, DOI: 10.1007/s11340-006-9025-5, October 2007.
5. Stanford, B., Sytsma, M., Albertani, R., Viieru, D., Shyy, W., Ifju, P.G., "Static Aeroelastic Model Validation of Membrane Micro Air Vehicles Wing," *AIAA Journal*, Vol. 45, No. 12, December 2007.
6. Albertani, R., DeLoach, R., Stanford, B., Hubner, J. P, Ifju, P., "Wind Tunnel Testing and Nonlinear Modeling Applied to Powered Micro Air Vehicles with Flexible Wings," *AIAA Journal of Aircraft*, December 2007.
7. Albertani, R., "A Wind Tunnel Study of Gurney Flaps applied to a Micro Aerial Vehicle," *AIAA Journal*, Volume 46, Number 6, June 2008.
8. K. Dupree, N.R. Gans, W. MacKunis and W.E. Dixon, "Euclidean Calculation of Feature Points of a Rotating Satellite: A Daisy Chaining Approach," *AIAA Journal of Guidance, Controls, and Dynamics*, Volume 31, Number 4, pp. 954-961, 2008
9. N. Gans, G. Hu and W. E. Dixon, "Image-Based State Estimation" in Autonomous Robotics, Complexity and Nonlinearity, in *Encyclopedia of Complexity and Systems Science*, Springer, *to appear*
10. G. Hu, N. Gans and W. E. Dixon, "Adaptive Visual Servo Control" in Autonomous Robotics, Complexity and Nonlinearity, in *Encyclopedia of Complexity and Systems Science*, Springer, *to appear*
11. G. Hu, W. MacKunis, N. Gans, W. E. Dixon, J. Chen, A. Behal, D. Dawson, "Homography-Based Visual Servo Control Via an Uncalibrated Camera," *IEEE Transactions on Automatic Control*, *to appear*, 2008 .

12. G. Hu, N. Gans, N. Fitz-Coy, and W. E. Dixon, "Adaptive Homography-Based Visual Servo Tracking Control Via A Quaternion Formulation," *IEEE Transactions on Control Systems Technology*, to appear.
13. K. Dupree, N.R. Gans, W. MacKunis and W.E. Dixon, "Euclidean Calculation of Feature Points of a Rotating Satellite: A Daisy Chaining Approach," *AIAA Journal of Guidance, Controls, and Dynamics*, Volume 31, Number 4, pp. 954-961, 2008.
14. G. Hu, D. Aiken, S. Gupta, W.E. Dixon, "Lyapunov-Based Range Identification For A Paracatadioptric System," *IEEE Transactions on Automatic Control*, Vol. 53, No. 7, pp. 1775-1781 (2008).

### **Submitted Journal Articles**

1. D.T. Grant, M. Abdulrahim and R. Lind, "Flight Dynamics of a Morphing Aircraft utilizing Independent Multiple-Joint Wing Sweep," *Journal of Aircraft*, in review.
2. M. Abdulrahim and R. Lind, "Control of Morphing Configurations for a Multi-Role Micro Air Vehicle," *Journal of Guidance, Control and Dynamics*, in review.
3. M.K. Kaiser, N. Gans and W. Dixon, "Vision-Based Estimation and Control of an Aerial Vehicle through Chained Homography," *IEEE Transactions on Aerospace and Electronic Systems*, submitted, 2008.
4. L. Ma, C. Cao, N. Hovakimyan, C. Woolsey, and W. E. Dixon, "Fast Estimation for Range Identification in the Presence of Unknown Motion Parameters," *IMA Journal of Applied Mathematics*, submitted.
5. N. Gans, W. Dixon, R. Lind and A Kurdilla, "A Hardware in the Loop Simulation Platform for Vision-Based Control of Unmanned Air Vehicles," *IFAC Journal of Mechatronics*, submitted, 2008.
6. G. Hu, N. Gans, and W. E. Dixon, "Quaternion-Based Visual Servo Control in the Presence of Camera Calibration Error," *International Journal of Robust and Nonlinear Control*, submitted.

### **Conference Papers**

1. Tang, J., Viieru, D. and Shyy, W., "A Study of Aerodynamics of Low Reynolds Number Flexible Airfoils," AIAA Paper No. 2007-4212, 37th AIAA Fluid Dynamics Conference and Exhibit, 2007.
2. G. Hu, N.R. Gans, S. Mehta, W.E. Dixon, "Daisy Chaining Based Visual Servo Control Part I: Adaptive Quaternion-Based Tracking Control," *Proc. IEEE Multi-conference on Systems and Control*, 2007 pp. 1474-1479.
3. G. Hu, S. Mehta, N.R. Gans, W.E. Dixon, "Chaining Based Visual Servo Control Part II: Extensions, Applications and Open Problems," *Proc. IEEE Multi-conference on Systems and Control*, 2007, pp. 729-734.
4. W. Mackunis, N.R. Gans, M. Kaiser, W. E. Dixon, "Unified Tracking and Regulation Visual Servo Control for Wheeled Mobile Robots," *Proc. IEEE Multi-conference on Systems and Control*, 2007, pp. 88-93.
5. K. Kaiser, N.R. Gans, W.E. Dixon, "Localization and Control of an Aerial Vehicle through Chained, Vision-Based Pose Reconstruction," *Proc. American Controls Conference*, 2007, pp. 3874-3879.

6. G. Hu, N.R. Gans, W.E. Dixon, "Quaternion-Based Visual Servo Control in the Presence of Camera Calibration Error," *IEEE Multi-conference on Systems and Control*, 2007, pp. 1492-1497.
7. K. Wright and R. Lind, "Investigating Sensor Emplacement on Vertical Surfaces for a Biologically-Inspired Morphing Design from Bats," AIAA Atmospheric Flight Mechanics Conference}, Hilton Head, SC, AIAA-2007-6488.
8. D.T. Grant and R. Lind, "Effects of Time-Varying Inertias on Flight Dynamics of an Asymmetric Variable-Sweep Morphing Aircraft," AIAA Atmospheric Flight Mechanics Conference}, Hilton Head, SC, AIAA-2007-6487.
9. D.T. Grant, M. Abdulrahim and R. Lind, "An Investigation of Biologically-Inspired Joints to Enable Sensor Pointing of Morphing Micro Air Vehicles," International Forum on Aeroelasticity and Structural Dynamics, Stockholm, Sweden, June 2007, IF-069.
10. D.T. Grant, M. Abdulrahim and R. Lind, "The Role of Morphing to Enhance Mission Capability of Micro Air Vehicles," World Forum on Smart Materials and Smart Structures Technology, invited paper, Chongqing and Nanjing, China, May 2007.
11. D.T. Grant, M. Abdulrahim and R. Lind, "Enhancing Mission Capability for Micro Air Vehicles using Biomimetic Joints and Structures," Australian International Aerospace Congress, Melbourne, Australia, March 2007.
12. Albertani, R., Stanford, B., Sytsma, M. and Ifju, P., "Unsteady Mechanical Aspects of Flexible Wings: an Experimental Investigation Applied on Biologically Inspired MAVs," *MAV07 3<sup>rd</sup> US-European Competition and Workshop on MAV Systems*, SUPAERO, Toulouse, France, September 18-21, 2007.
13. Stewart, K., Albertani, R., "Experimental Elastic Deformation Characterization of a Flapping-Wing MAV using Visual Image Correlation," *MAV07 3<sup>rd</sup> US-European Competition and Workshop on MAV Systems*, SUPAERO, Toulouse, France, September 18-21, 2007.
14. Khambatta, P., Tinney, C., Ukeiley, L., Stanford, B., and Ifju, P., "Flow Characteristics of a Three Dimensional Micro Air Vehicle Wing," AIAA Fluid Dynamics Conference, July 2008.
15. Albertani, R., Stewart, K., "Analysis of Wind Tunnel Unsteady Aerodynamic Data of Flexible Micro Air Vehicle Wings," abstract submitted to the 26th *AIAA Applied Aerodynamic Conference*, January 2008.
16. Albertani, R., Babcock, J., "Analysis of Wind Tunnel Unsteady Aerodynamic Data of Flexible Micro Air Vehicle Wings," 26th *AIAA Applied Aerodynamic Conference*, Honolulu, HI, August 18-21, 2008.
17. Albertani, R., "Experimental Characterization of Microflaps," *2<sup>nd</sup> NWF MAV08 Workshop*, University of Florida REEF, Shalimar, May 27-29, 2008.
18. Hu, H., Abate, G., Albertani, R. "An Experimental Investigation on Flapping Flexible Membrane Wings," abstract submitted for the *47h AIAA Aerospace Sciences Meeting*, Orlando, FL, January 5-8, 2009.
19. Albertani, R., Khambatta, P., Ukeiley, L., Cattafesta, L., Oyarzun, M., Abate, G., "Validation of an Aerodynamic Characterization Facility," abstract submitted for the *47h AIAA Aerospace Sciences Meeting*, Orlando, FL; January 5-8 y, 2009.
20. A. Chakravarthy., D.T. Grant, R. Lind, "Computation of Poles for LTV Systems", submitted to the American Control Conference 2009, (under review).

21. N. R. Gans, G. Hu and W. E. Dixon, "Keeping Multiple Objects in the Field of View of a Single PTZ Camera," Proc. American Controls Conference, 2009, submitted
22. A. P. Dani, N. R. Gans and W. E. Dixon, "Position-Based Visual Servo Control of Leader-Follower Formation Using Image-Based Relative Pose and Relative Velocity Estimation," Proc. American Controls Conference, 2009, submitted
23. N. R. Gans, J. Shea, P. Barooah and W. E. Dixon, "Ensuring Network Connectivity of UAV's Performing Video Reconnaissance," Proc. MILCOM, 2008, accepted, to appear
24. A. P. Dani, S. Velat, C. Crane, N. R. Gans and W. E. Dixon, "Experimental Results for an Image-Based Pose and Velocity Estimation Method," Proc. IEEE Conference on Control Applications, 1159-1164, 2008
25. N. R. Gans, G. Hu, W. E. Dixon, "Simultaneous Stability of Image and Pose Error in Visual Servo Control," Proc. IEEE International Symposium on Intelligent Control, pp. 438-443, 2008
26. N. R. Gans, G. Hu, W. E. Dixon, "Keeping Objects in the Field of View: An Underdetermined Task Function Approach to Visual Servoing," Proc. IEEE International Symposium on Intelligent Control, pp. 432-437, 2008
27. S. S. Mehta, G. Hu, A. P. Dani, **W. E. Dixon**, "Multi-Reference Visual Servo Control of an Unmanned Ground Vehicle," *Proceedings of AIAA Guidance, Navigation, and Controls Conference*, Hawaii, 2008.
28. N. R. Gans, A. Dani, W. E. Dixon, "Visual Servoing to an Arbitrary Pose with Respect to an Object Given a Single Known Length," Proceedings of the American Control Conference, pp. 1261-1267, 2008
29. G. Hu, W. Mackunis, N. Gans, and W. E. Dixon, "Homography-Based Visual Servo Control via An Uncalibrated Camera," Proc. American Controls Conference, 2008, pp. 4791-4796.
30. K. Dupree, S. Mehta, C. Crane and W. E. Dixon, "Euclidean Calculation of the Pose of an Unmanned Ground Vehicle: A Daisy Chaining Approach," *International Joint Topical Meeting on Emergency Preparedness & Response and Robotics & Remote Systems*, Albuquerque, New Mexico, 2008, pp. 557-562.

## HONORS & AWARDS RECEIVED

Best Paper in Session, 2007 *American Controls Conference*: K. Kaiser, N.R. Gans, W.E. Dixon, "Localization and Control of an Aerial Vehicle through Chained, Vision-Based Pose Reconstruction"

## AFRL POINTS OF CONTACT

Dr. David Jeffcoat (DSN 875-2693), Dr. Gregg Abate (833-9355 ex 303), and Dr. Johnny Evers (850-883-2693) are AFRL/RW points of contact on a daily basis. Dr. Abate is a team leader whose team is co-located at the UF-REEF to insure collaborative research occurs between AFRL/MN and the UF-REEF research team.

## TRANSITIONS

The micro air vehicle technologies in agile, flexible airframes, vision based guidance, and vision based control has transitioned into assets provided to our Air Force Special Operations Forces. Specific technologies being transition are not for public release and would have to be addressed through Dr. Abate.

#### NEW DISCOVERIES

1. W. Dixon, N. Gans, M. Kaiser, *Image-Based System and Methods for Vehicle Guidance and Navigation*, Patent Cooperative Treaty No. PCT/US2007/76419, filed August 21, 2007, Pending.
2. W. Dixon, N. Gans, S. Gupta, *Passive Single Camera Imaging System for Determining Motor Vehicle Speed*, Patent Cooperative Treaty No. PCT/US2007/83895, filed November 7, 2007, Pending.

the  $\text{H}_2$  atom and the  $\text{H}_2$  molecule. The  $\text{H}_2$  atom has a radius of  $1.2 \times 10^{-10} \text{ cm}$  and the  $\text{H}_2$  molecule has a radius of  $1.2 \times 10^{-10} \text{ cm}$ .

The  $\text{H}_2$  atom has a radius of  $1.2 \times 10^{-10} \text{ cm}$  and the  $\text{H}_2$  molecule has a radius of  $1.2 \times 10^{-10} \text{ cm}$ .